

NASA CR-72562
PWA-3546



DESIGN REPORT
SINGLE-STAGE EVALUATION OF HIGHLY-LOADED
HIGH-MACH-NUMBER COMPRESSOR STAGES

by
N. T. Monsarrat, M. J. Keenan and P. C. Tramm

Pratt & Whitney Aircraft Division
United Aircraft Corporation

N69-30869

FACILITY FORM 802	_____ (ACCESSION NUMBER)	_____ (TRU)
	_____ (PAGES)	_____ (CODE)
	_____ (NASA CR OR TMX OR AD NUMBER)	_____ (CATEGORY)

prepared for
NATIONAL AERONAUTICS AND SPACE ADMINISTRATION

NASA Lewis Research Center
Contract NAS3-10482
L. Reid, Project Manager

NOTICE

This report was prepared as an account of Government sponsored work. Neither the United States, nor the National Aeronautics and Space Administration (NASA), nor any person acting on behalf of NASA:

- A.) Makes any warranty or representation, expressed or implied, with respect to the accuracy, completeness, or usefulness of the information contained in this report, or that the use of any information, apparatus, method, or process disclosed in this report may not infringe privately owned rights; or
- B.) Assumes any liabilities with respect to the use of or for damages resulting from the use of any information, apparatus, method or process disclosed in this report.

As used above, "person acting on behalf of NASA" includes any employee or contractor of NASA, or employee of such contractor, to the extent that such employee or contractor of NASA, or employee of such contractor prepares, disseminates, or provides access to, any information pursuant to his employment or contract with NASA, or his employment with such contractor.

Requests for copies of this report should be referred to:

National Aeronautics and Space Administration
Scientific and Technical Information Facility
P. O. Box 33, College Park, Maryland 20740

NASA CR-72562
PWA-3546

DESIGN REPORT
SINGLE-STAGE EVALUATION OF HIGHLY-LOADED
HIGH-MACH-NUMBER COMPRESSOR STAGES

by
N. T. Monsarrat, M. J. Keenan and P. C. Tramm

Pratt & Whitney Aircraft Division
United Aircraft Corporation
East Hartford, Connecticut 06108

Prepared for
NATIONAL AERONAUTICS AND SPACE ADMINISTRATION

July 16, 1969

Contract NAS3-10482

NASA Lewis Research Center
Cleveland, Ohio
L. Reid, Project Manager
Fluid System Components Division

FOREWORD

This report was prepared by the Pratt & Whitney Aircraft Division of United Aircraft Corporation, East Hartford, Connecticut, to describe the aerodynamic and mechanical design work conducted under Contract NAS3-10482, Single-Stage Evaluation of Highly-Loaded High-Mach-Number Compressor Stages. Mr. L. Reid, NASA-Lewis Research Center, Fluid System Components Division, was Project Manager.

TABLE OF CONTENTS

	<u>Page</u>
FOREWORD	ii
TABLE OF CONTENTS	iii
LIST OF FIGURES	iv
LIST OF TABLES	vii
I. SUMMARY	1
II. INTRODUCTION	3
III. AERODYNAMIC DESIGN	4
IV. AIRFOIL DESIGN	15
A. Rotor	15
B. Stator	28
C. Stator Slit Design	35
V. STRUCTURAL AND VIBRATION ANALYSIS	37
A. Blade and Disc Vibration	37
B. Blade Stress	37
C. Torsional Blade Flutter	41
D. Disc and Attachment Stresses	43
E. Critical Speeds	44
APPENDIX 1 - Aerodynamic Calculation Procedure	45
APPENDIX 2 - Loss System	47
APPENDIX 3 - Incidence Selection	53
APPENDIX 4 - Stream-Tube Analysis in Channels Between Blades	60
APPENDIX 5 - Deviation System	64
APPENDIX 6 - Aerodynamic Summary	68
APPENDIX 7 - Airfoil Sections on Conical Surfaces (Multiple-Circular-Arc Definitions)	73 73
APPENDIX 8 - Rotor Slot Design	76
APPENDIX 9 - Tandem Rotor Design	90
APPENDIX 10 - Airfoil Coordinates for Manufacturing Sections	97
APPENDIX 11 - Nomenclature	105
REFERENCES	110

LIST OF FIGURES

<u>Number</u>	<u>Title</u>	<u>Page</u>
1	Flowpath	6
2	Rotor and Stator Portion of Flowpath	7
3	Rotor and Stator Inlet and Exit Meridional Velocity Profiles	8
4	Rotor and Stator Inlet Mach Numbers	9
5	Rotor and Stator Diffusion Factor Profile	11
6	Rotor Adiabatic Efficiency	12
7	Stator Spanwise Loss Profile	13
8	Rotor Inlet and Exit Relative and Stator Inlet Absolute Meridional Air Angle Profiles	14
9	Multiple-Circular-Arc Airfoil Definitions	16
10	Four Views of Rotor	17
11	Axial Projection of Rotor	18
12	Rotor Incidence	19
13	Slotted Rotor Blade Section	20
14	Tandem Rotor Blade Section	21
15	Rotor Entrance Region Relative Air Angle Showing Effects of Annulus Convergence and Front Camber	23
16	Rotor Entrance Region Relative Mach Number Showing Effects of Annulus Convergence and Front Camber	24
17	Rotor Spanwise Variation of a/a^*	25
18	Rotor Deviation	26
19	Rotor Inlet and Exit Mean Camber Line Metal Angles on Conical Surface	27

LIST OF FIGURES (Cont'd)

<u>Number</u>	<u>Title</u>	<u>Page</u>
20	Four Views of Stator	29
21	Axial Projection of Stator	30
22	Stator Leading-Edge Suction Surface and Mean Camber Line Incidence	31
23	Stator Spanwise Variation of α/a^*	32
24	Stator Deviation	33
25	Stator Inlet and Exit Mean Camber Line Metal Angles on Conical Surface	34
26	Slit Flow to Prevent Corner Separation at Intersection of Stator Suction Surface and Hub Wall	36
27	Blade and Disc Resonance Diagram	38
28	Maximum Stress Locations	39
29	Effect of Tangential Tilt on Rotor Gas Bending Stress	40
30	Rotor Goodman Diagram	42
31	Compressor Rig Spring Location and Spring Rates	44
32	Location of Assumed Normal Shock for Loss Model	49
33	Rotor Profile Loss Parameter vs D Factor	51
34	Stator Profile Loss Parameter vs D Factor	52
35	Multiple-Circular-Arc Stator B Loss Data for 50 Percent Span from Contract NAS3-7614	55
36	Multiple-Circular-Arc Stator B Loss Data for 5 Percent Span from Root, Contract NAS3-7614	56
37	Multiple-Circular-Arc Stator B Loss Data for 95 Percent Span from Root, Contract NAS3-7614	57

LIST OF FIGURES (Cont'd)

<u>Number</u>	<u>Title</u>	<u>Page</u>
38	Wave Pattern for Super-Critical Operation of Curved-Blade Entrance Regions	58
39	Channel Area	62
40	Loss Distribution through Channel	63
41	Modification to Carter's Rule for Rotor	66
42	Modification to Carter's Rule for Stator	67
43	Recovery Increase vs Slot Angle	78-80
44	Axial Projection of Slotted Rotor	81
45	Rotor Efficiency vs Rotor Exit Diameter	88
46	Rotor Blade Resonance Diagram	89
47	Axial Projection of Tandem Rotor	92
48	Airfoil Coordinates for Manufacturing Sections	98

LIST OF TABLES

<u>Number</u>	<u>Title</u>	<u>Page</u>
1	Aerodynamic Design Point	4
2	Design Parameters	4
3	Rotor and Stator Stresses	41
4	Disc and Attachment Stresses	43
5	Compressors Analyzed for Profile Loss Correlation	50
6	Aerodynamic Summary - Rotor Inlet	69
7	Aerodynamic Summary - Rotor Exit	70
8	Aerodynamic Summary - Stator Inlet	71
9	Aerodynamic Summary - Stator Exit	72
10	Airfoil Sections on Cylindrical Surfaces - Rotor	74
11	Airfoil Sections on Conical Surfaces - Stator	75
12	Rotor Coordinates - Sections A, B, C and D	99
13	Rotor Coordinates - Sections E, F, G and H	100
14	Rotor Coordinates - Sections J, K, L and M	101
15	Stator Coordinates - Sections A, B, C and D	102
16	Stator Coordinates - Sections E, F, G and H	103
17	Stator Coordinates - Sections J, K and L	104

ABSTRACT

DESIGN REPORT SINGLE-STAGE EVALUATION OF HIGHLY-LOADED HIGH-MACH-NUMBER COMPRESSOR STAGES

A compressor stage of 1600 ft/sec (487.7 m/sec) tip speed, a D factor at 10 percent span from the tip of 0.5, and a hub/tip ratio of 0.5 was designed to deliver a pressure ratio of 1.936 with an efficiency of 0.842. The design flow rate is 187.1 lb/sec (84.869 kg/sec). Three rotors were designed, the first with multiple-circular-arc airfoils, the second with slotted airfoils, and the third with tandem airfoil sections. The same stator will be used with all three rotors.

I. SUMMARY

A high-tip-speed single-stage compressor has been designed under Contract NAS3-10482. This report presents the detailed aerodynamic and mechanical design. The design is intended to document the performance of a stage with a high rotor tip speed and with high aerodynamic loadings on both the rotor and stator. The feasibility of using high rotor-inlet relative Mach numbers and high blade loadings to obtain a high pressure ratio at an acceptable level of efficiency will be evaluated. The important features of this design are that there is no inlet guide vane, the rotor tip speed is 1600 ft/sec (487.7 m/sec), overall stage pressure ratio is 1.936, rotor leading-edge tip diameter is 33 inches (0.8382m), rotor inlet hub/tip ratio 0.5, rotor-tip solidity 1.3, and stator-hub solidity 2.0.

The aerodynamic design was based on the approximate design parameters specified in the contract, typical performance requirements for advanced fans, and the use of existing test facilities. The design flow per unit of annulus area at the rotor leading edge is 42 lb/sec/ft² (205.07 kg/sec/m²). The rotor was designed for a constant spanwise pressure ratio of 2.0. Blade losses for both rotor and stator were estimated using a loss model in which shock loss and profile loss are considered separately with their sum equal to the total blade loss. Performance calibrations using this model predicted an adiabatic rotor efficiency of 88.7 percent, and an overall stage average adiabatic efficiency of 84.2 percent.

Three rotor configurations were designed, one with multiple-circular-arc airfoil sections, the second with slots, and the third with tandem airfoils. The multiple-circular-arc airfoil is the basic blade design, the slotted and tandem designs being modifications which use essentially the same solidity, and the same chordwise distributions of camber and thickness.

The multiple-circular-arc rotor airfoil sections were designed to obtain low loss by appropriate camber distribution. Slots were designed for these multiple-circular-arc sections to deflect supersonic flow with slot exit flow, causing an oblique shock to form upstream of the normal shock. Combined shock losses of the precompression and normal shocks were calculated to be less than normal shock losses without precompression.

Tandem rotor airfoils were designed by dividing the multiple-circular-arc sections just to the rear of the assumed shock impingement point on the suction surface. Shock boundary-layer interaction effects are isolated from subsonic diffusion by a stream of high-energy air flowing between front and rear tandem sections. Since the initial condition of the boundary layer on the rear airfoil should not be affected by the shock, efficient subsonic diffusion should be obtained.

The rotor-inlet hub-tip ratio is 0.50 and was set primarily by mechanical considerations. The rotor and stator aspect ratios are 1.663 and 1.721 respectively, using root

chord and average length. The rotor chord is constant spanwise at 4.4 inches (0.11176m) which, with 30 blades, yields a rotor tip solidity of 1.297. The low aspect ratio is not typical of engine designs, but was considered preferable to use of a part-span shroud which would have given unreliable blade-element data in the region of the part-span shroud. The stator chord is also constant spanwise at 3.0 inches (0.07620 m) and, with 44 blades, yields a root solidity of 2.047.

Mechanical design included a structural and vibration analysis. Centrifugal stress, gas bending stress, and stress produced by untwist are all well within the capabilities of the AMS 4928 titanium alloy to be used for the blades. Because all critical speeds are outside the operating range, vibratory stress levels should be low.

II. INTRODUCTION

Future aircraft powerplants will require lightweight highly-loaded compressors which are very efficient over a wide operating range. Pressure ratio per stage can be increased considerably above current levels by increasing rotor wheel speed and blade loadings. In general, such attempts have been discouraging and resulted in severe aerodynamic penalties. High blade-element losses result from normal shocks at high Mach numbers, shock boundary-layer interactions on blade surfaces, and boundary-layer growth due to high blade loadings. Recently-developed design techniques and new concepts of blade design may be employed to gain this work increase without attendant efficiency loss.

In general, loss in high Mach-number rotor blading is strongly related to chordwise camber distribution. The optimum blade shape provides the best balance between shock loss and subsonic diffusion loss. The supersonic curvature should account for axial velocity changes due to annulus convergence, and provide a cancelling system of expansion and compression waves across each rotor gap. Channel area between blades must be adequate to pass the flow, but should be small enough to limit the growth of a separated boundary layer.

A new airfoil termed multiple-circular arc has been designed by NASA. The multiple-circular-arc airfoil is formed by portions of two circular-arc sections, with blade surfaces and the mean camber line each mutually tangent at the points where they join. Blades of this type provide a means of varying blade shape to control camber distribution and minimize overall blade losses. Two recent experimental evaluations of this airfoil, References* 1 to 4 for rotors, and Reference 5 for stators, have provided data indicating probable success for a stage of this type. In view of this, a high-tip-speed highly-loaded single stage was designed and will be fabricated and tested under Contract NAS3-10482.

In addition to the basic rotor design configuration, two other rotors were designed to evaluate other advanced concepts. A slotted rotor was designed in which slot discharge flow is used to cause an oblique shock to reduce the Mach number upstream of the normal shock and reduce overall shock loss. A tandem rotor was designed with a supersonic forward blade and a subsonic rear blade. The shock impinges on the forward blade, whose boundary layer is isolated from the subsonic suction surface by a stream of high-energy air.

This report presents the aerodynamic and mechanical design of the compressor stage, including all three rotor configurations.

*See Page 110 for numbered list of references

III. AERODYNAMIC DESIGN

Velocity vector diagrams within the flowpath were used to design rotor and stator blade elements. Rotor and stator blade elements were designed based on their leading and trailing-edge vector diagrams. Design of the stage flowpath was guided by the aerodynamic objectives specified in the contract. Multiple-circular-arc airfoil sections were designed for both blade rows. A slotted rotor and a tandem rotor were also designed for the same velocity vectors, although the slotted and tandem rotors are expected to operate with lower losses. The design point for the stage is summarized in Table 1.

TABLE 1
Aerodynamic Design Point

corrected speed, rpm	11,110
corrected flow, lb/sec (kg/sec)	187.1 (84.869)
rotor pressure ratio	2.0
stage pressure ratio	1.936
rotor adiabatic efficiency, %	88.7
stage adiabatic efficiency, %	84.2

The stage design parameters are compared with the approximate values specified by the contract work statement in Table 2.

TABLE 2
Design Parameters

	<u>Final Design</u>	<u>Work Statement</u>
rotor inlet tip diameter, inches (meter)	33.0(0.8382)	30.0 (0.7620) min.
rotor tip speed, ft/sec (m/sec)	1600(487.68)	1600(487.68)
rotor inlet tip relative Mach number	1.609	1.6
rotor tip diffusion factor	0.5 at 10% span from tip	0.55
rotor inlet hub-tip ratio	0.5	0.5 max.
rotor tip solidity	1.297	1.3
rotor tip inlet-to-exit axial velocity ratio	1.682(1.25 at 10% span from tip)	1.0

rotor aspect ratio, average length/root chord	1.663	2.0
stator hub solidity	2.047	2.0
stator root inlet-to-exit velocity ratio	1.007	1.0
stator aspect ratio, average length/root chord	1.721	2.0

The stage is designed without an inlet guide vane and the stator exit flow angle is zero at all radii. Rotor exit pressure is uniform spanwise as specified by the contract. Rotor design pressure ratio is 2.0 and was established as a consequence of the intended rotor-tip loading. With the design stator losses the stage average pressure ratio becomes 1.936.

The rotor inlet flow per unit annulus area was set at 42 lb/sec/ft² (205.07 kg/sec/m²). An analysis was made to determine the effect of inlet flow per unit annulus area on stage efficiency. This study showed that reducing the flow to 40 lb/sec/ft² (195.2 kg/sec/m²) did not improve the stage efficiency appreciably. The higher value of inlet flow per unit annulus area was selected as the more desirable stage because of weight and frontal area considerations.

The rotor inlet hub/tip ratio of 0.5 and aspect ratio of 1.663 are not typical of advanced stages and were set by mechanical design considerations, as discussed in Section V. No part-span shroud was used in order to have a maximum of useful blade-element data. The low aspect ratio was necessary from flutter and resonance considerations, and the moderately high hub/tip ratio was required to maintain acceptable steady-state stresses.

The flowpath, including stage inlet and exit ducting, is shown by Figure 1. Figure 2 shows the rotor and stator portion of the flowpath in more detail. Flowpath convergence was used to control levels and radial distributions of meridional velocity throughout the compressor. Because of the high stage pressure ratio, considerable convergence was required to obtain equal meridional velocity levels at the stage inlet and exit. This consideration is desirable from the standpoint of possible applications for a stage of this type. Studies of possible flowpath contours showed that a meridional angle of 14 degrees over the rotor tip gave the desired rotor-tip D-factor. Overall convergence was obtained with a rotor-hub meridional angle of 20 degrees, with both walls faired to the axial direction midway through the stator. The spacing between the rotor and stator was set at 1.20 inch (0.0305 meter) at the hub, to provide sufficient room for interstage instrumentation. Figure 3 shows inlet and exit meridional velocity distributions for the rotor and stator. Rotor exit meridional velocity is less than at the rotor inlet, particularly at the tip.

Inlet Mach numbers for the rotor and stator are shown by Figure 4. It should be noted that the rotor-inlet relative Mach number is supersonic over nearly the entire span. The stator Mach number is subsonic spanwise with a maximum value of 0.89 occurring at the hub.

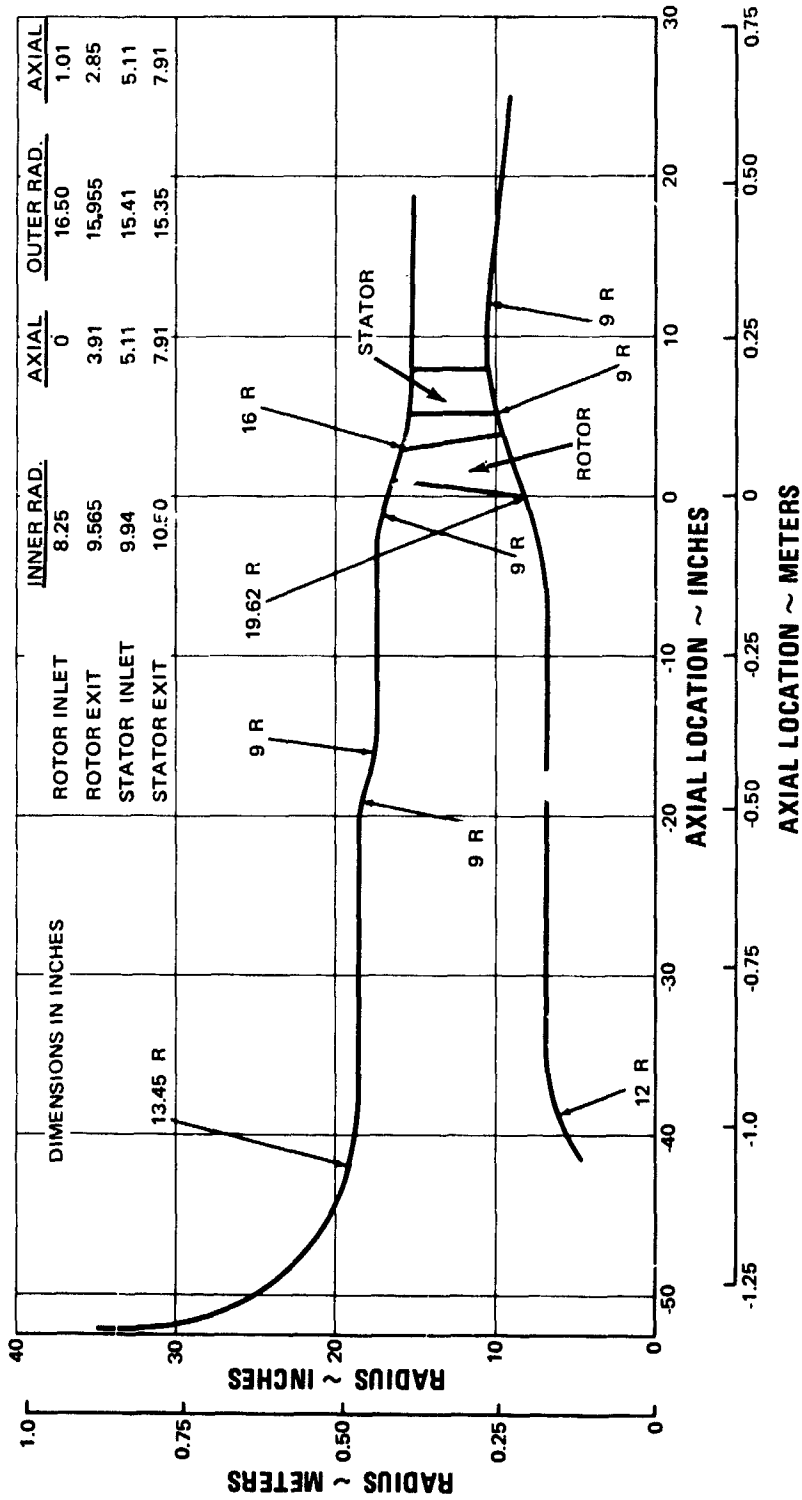


Figure 1 Flowpath

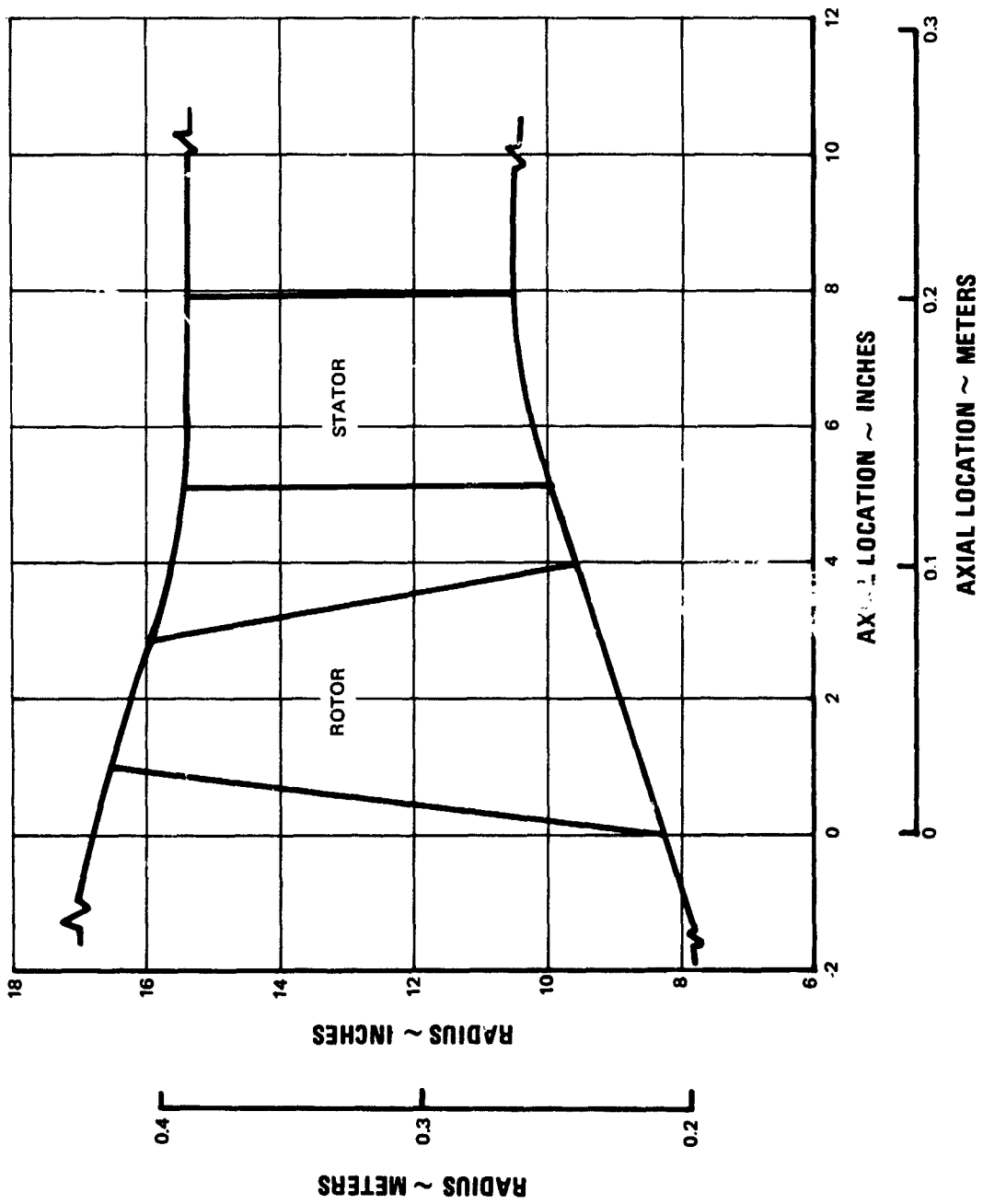


Figure 2 Rotor and Stator Portion of Flowpath

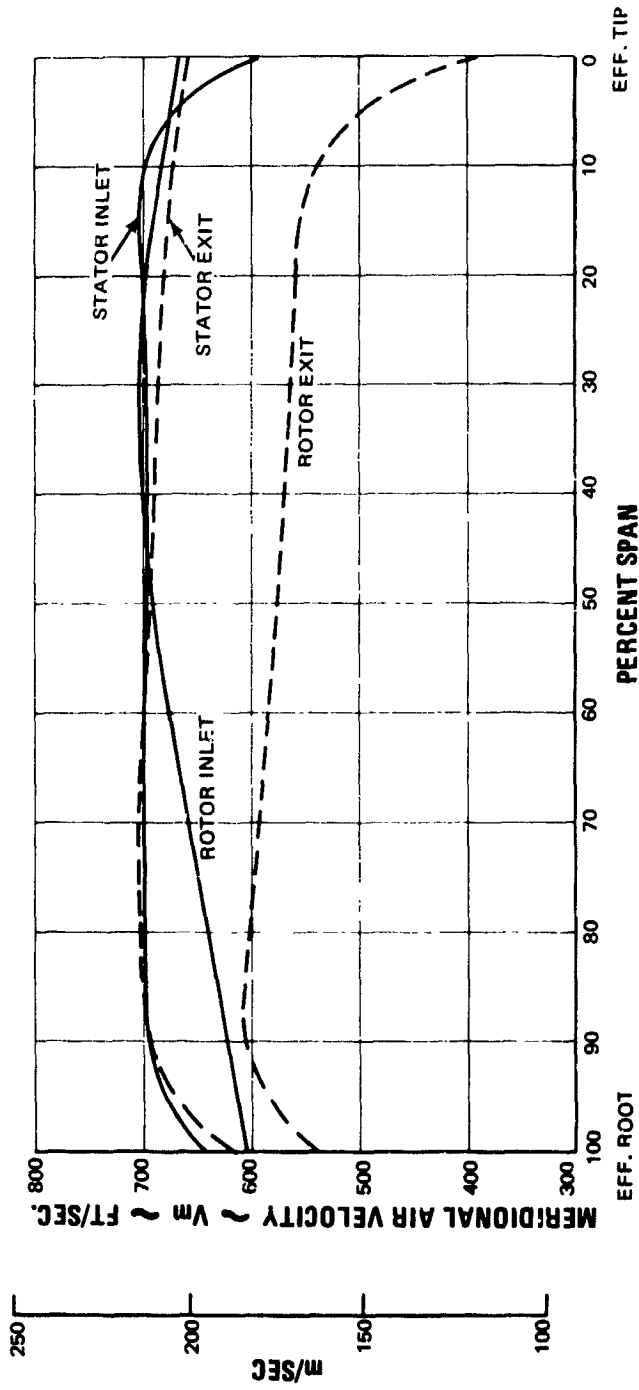


Figure 3 Rotor and Stator Inlet and Exit Meridional Velocity Profiles

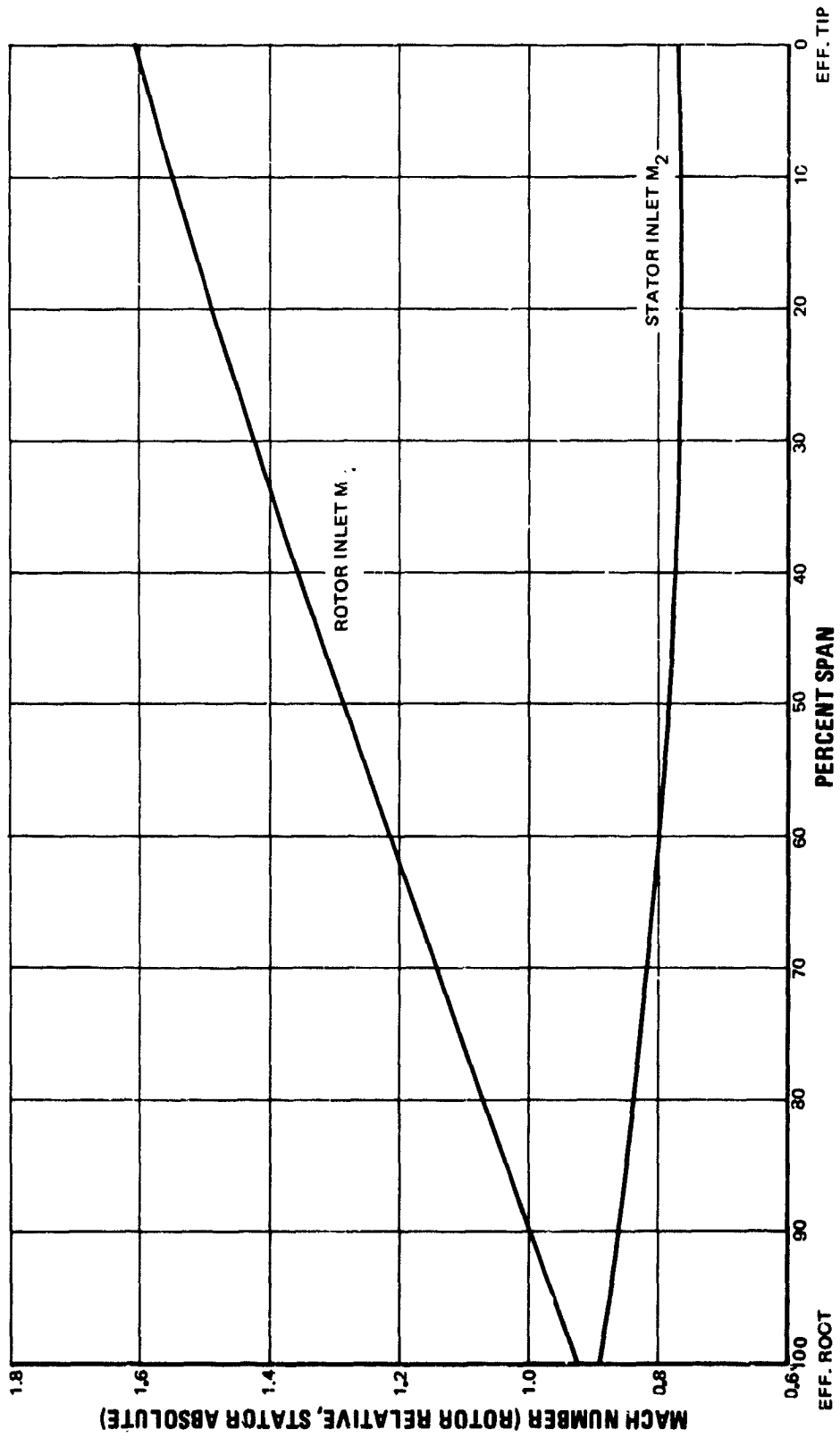


Figure 4 Rotor and Stator Inlet Mach Numbers

The chords of both the rotor and stator were held constant from root to tip. Blade-element loading as represented by diffusion factor is shown in Figure 5. It is noted that both the rotor and stator exhibit a trend towards increased loading at the end walls, which is a result of designing for anticipated higher losses in these portions of the blading. The blade elements between 10 and 90 percent of span are relatively free of these end effects and the diffusion factors of both the rotor and stator are well below 0.6. The rotor diffusion factor increases rapidly from 0.5 at ten percent of span from the tip, to a value of 0.62 at the tip. The level of loading in the neighborhood of the rotor tip is considered consistent with the intent of the contractual requirement for a 0.55 rotor-tip diffusion factor.

The procedure used to calculate the velocity triangles was an iteration involving the flow-field calculation given in Appendix 1 and the loss system given in Appendix 2. The flow-field calculation procedure solves the continuity, energy, and radial equilibrium equations including effects of streamline curvature, slope, and entropy gradient. Stagnation pressures and temperatures are entered spanwise behind the rotor and stator. The iteration is required because the velocity triangles are dependent upon losses which, in turn, are dependent upon the blade-inlet Mach number and loading. In general, it takes three passes before the blade and aerodynamic calculations are consistent. Figures 6 and 7 show the spanwise variation of rotor adiabatic efficiency and stator loss respectively. Boundary-layer growth on the flowpath walls was estimated using test data from several single-stage rigs of similar size. Effective end walls within the actual flowpath were used to account for the displacement thickness of the wall boundary layers. The ratio of actual-to-effective area is 1.005 ahead of the rotor, 1.01 between the rotor and stator, and 1.015 behind the stator. Area reductions were obtained by locating effective walls at equal percentages of span inside of the actual walls.

Figure 8 shows the rotor inlet and exit relative air angles and the stator inlet absolute air angle. The stator turns the flow to axial at the rig discharge and flow enters the rotor without swirl. The design vector diagrams are presented in Appendix 7 at the rotor and stator leading and trailing edges along streamlines for every ten percent of flow radially.

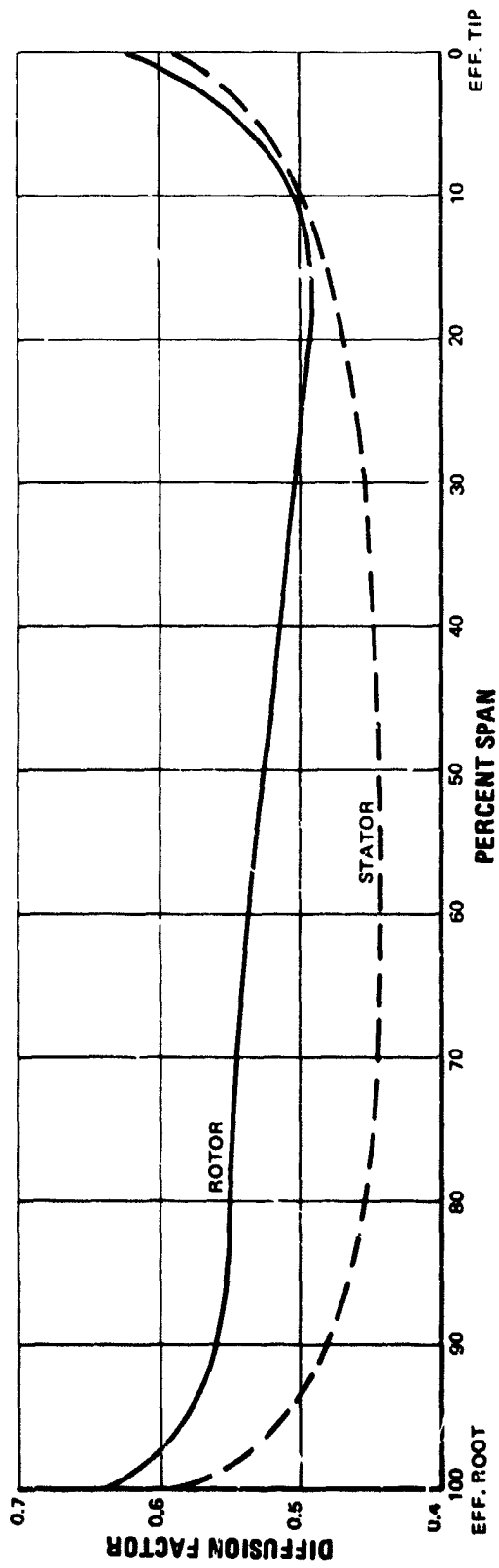


Figure 5 Rotor and Stator Diffusion Factor Profile

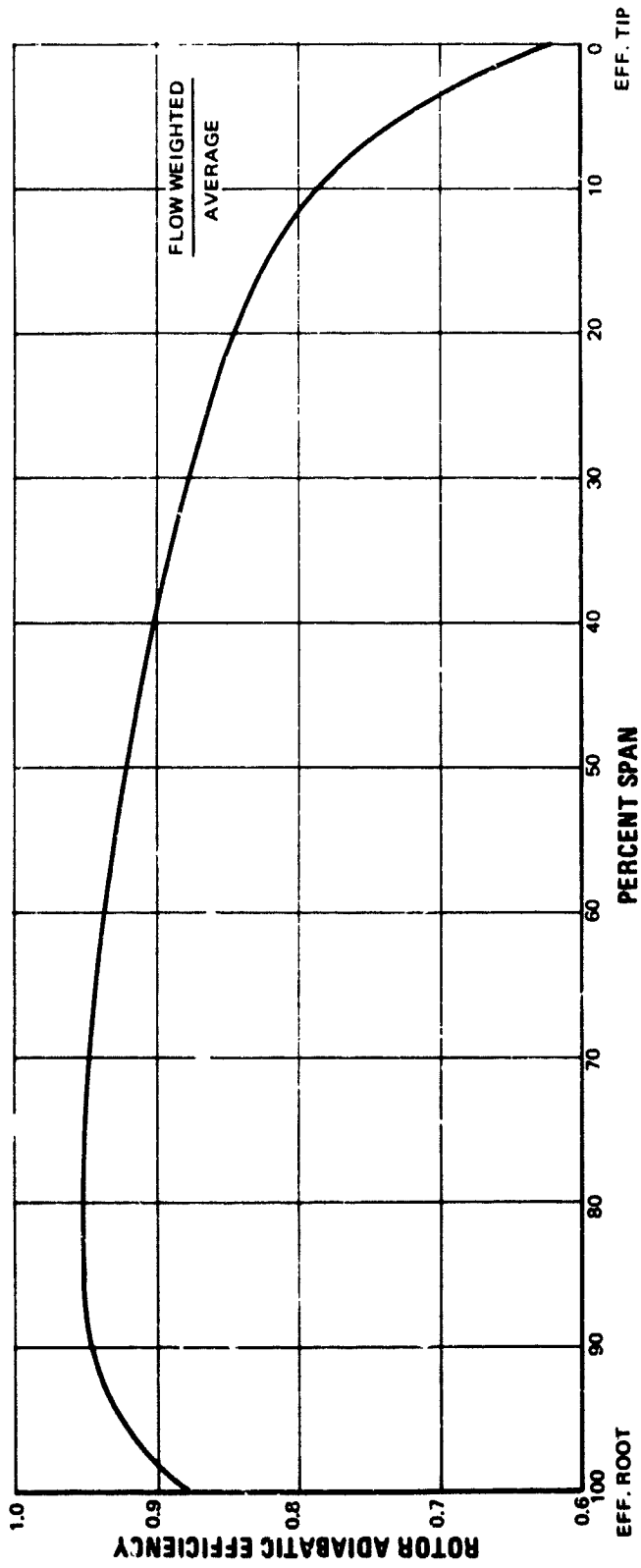


Figure 6 Rotor Adiabatic Efficiency

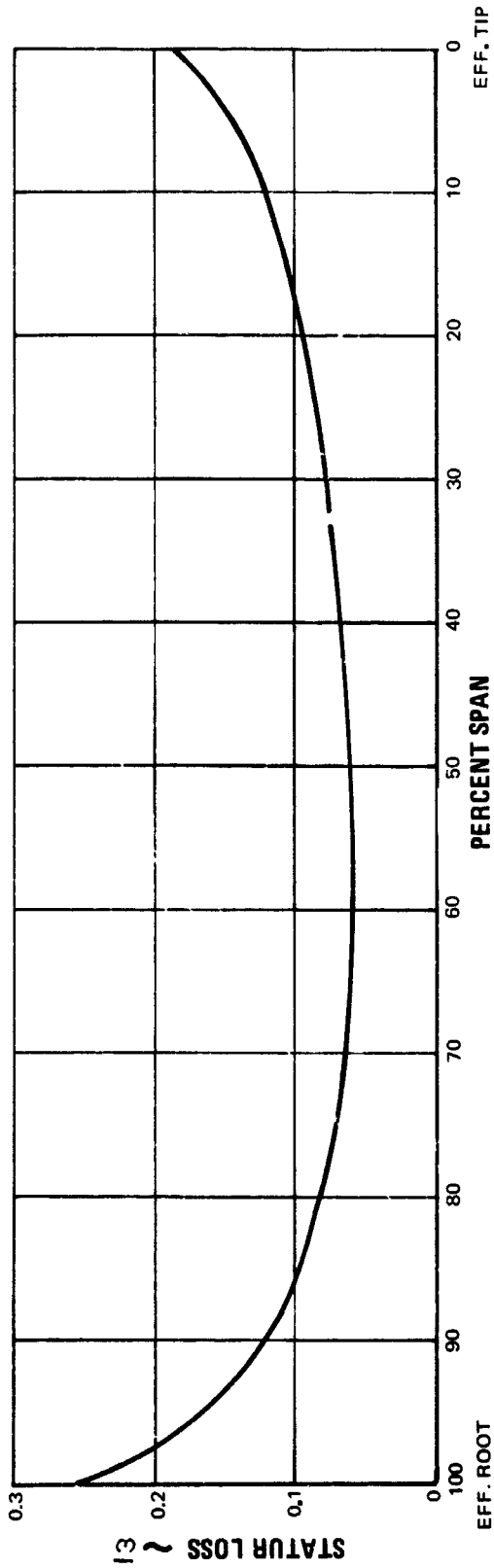


Figure 7 Stator Spanwise Loss Profile

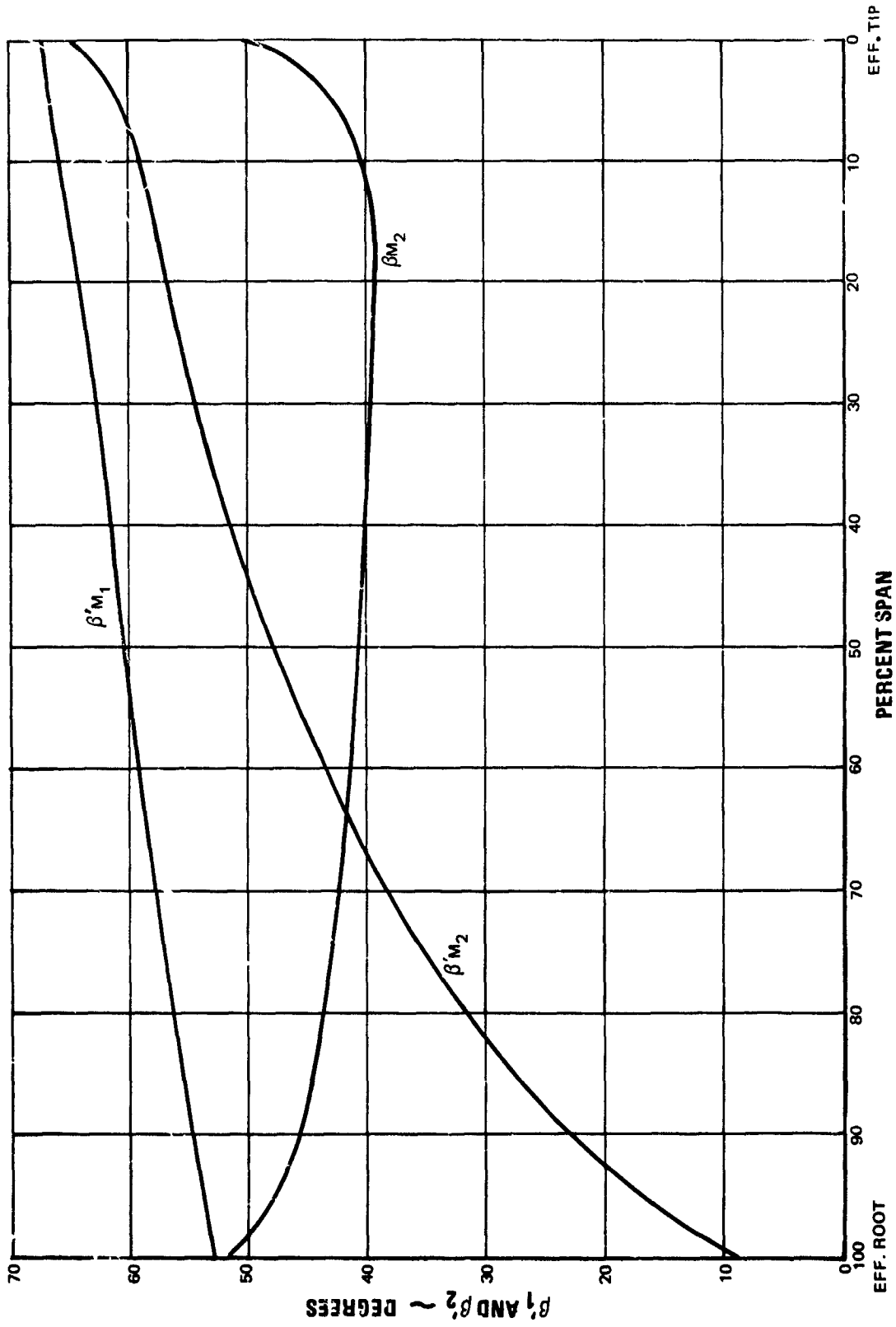


Figure 8 Rotor Inlet and Exit Relative and Stator Inlet Absolute Meridional Air Angle Profiles

IV. AIRFOIL DESIGN

A. Rotor

The rotor chord is constant spanwise at 4.4 inches (0.11176 m) which, with 30 blades, yields a rotor-tip solidity of 1.297. The low rotor aspect ratio (1.66) is not typical of front stages for engine design, but was considered preferable to use of a part-span shroud.

The rotor uses multiple-circular-arc airfoil sections designed on conical surfaces which approximate streamlines of revolution. Airfoil sections are defined by specifying total and front chord, total and front camber, maximum thickness and its location, and leading and trailing edge radii, as shown by Figure 9. Figure 10 shows several views of the rotor.

The total chord and thickness ratio were so selected as to provide mechanical integrity. The ratio of front chord to total chord was set to provide a transition point just aft of the assumed shock location, discussed in Appendix 2 and shown by Figure 32. Figure 11 is an axial projection of the blade and shows the chordwise location of the transition point versus radius. The maximum thickness was so located that for a given total camber, front camber, total chord and front chord, the leading edge wedge angle is the minimum possible without a cusp shape in the front portion of the blade.

The thickness ratio was set at 0.10 at the root to provide mechanical integrity. This is somewhat thicker than optimum from loss considerations, but was necessary from a structural point of view. The thickness ratio varies linearly from the root to a value of 0.025 at the tip.

Multiple-circular-arc rotor airfoil forward sections were tailored to satisfy entrance-region requirements and to provide the desired throat width in the channel between blades. The approach and design procedure for the forward section is discussed fully in Appendix 3. Rearward sections were designed to give the necessary air turning for design work input. Deviation angles were calculated using Carter's rule plus an experience factor, as discussed in Appendix 5.

Incidence was set at approximately 1.5 degrees to the suction surface at a point midway between the leading edge and the first captured Mach-wave emanation point, Point B' in Figure 38. Incidence at this point, together with entrance-region and channel-area considerations, determined leading-edge incidence. Incidence at Point B' and at the leading edge is shown in Figure 12. Flow channels between front and rear blade sections in both slotted and tandem designs are downstream of the first captured Mach wave, where they cannot affect entrance-region flow (Figures 13 and 14).

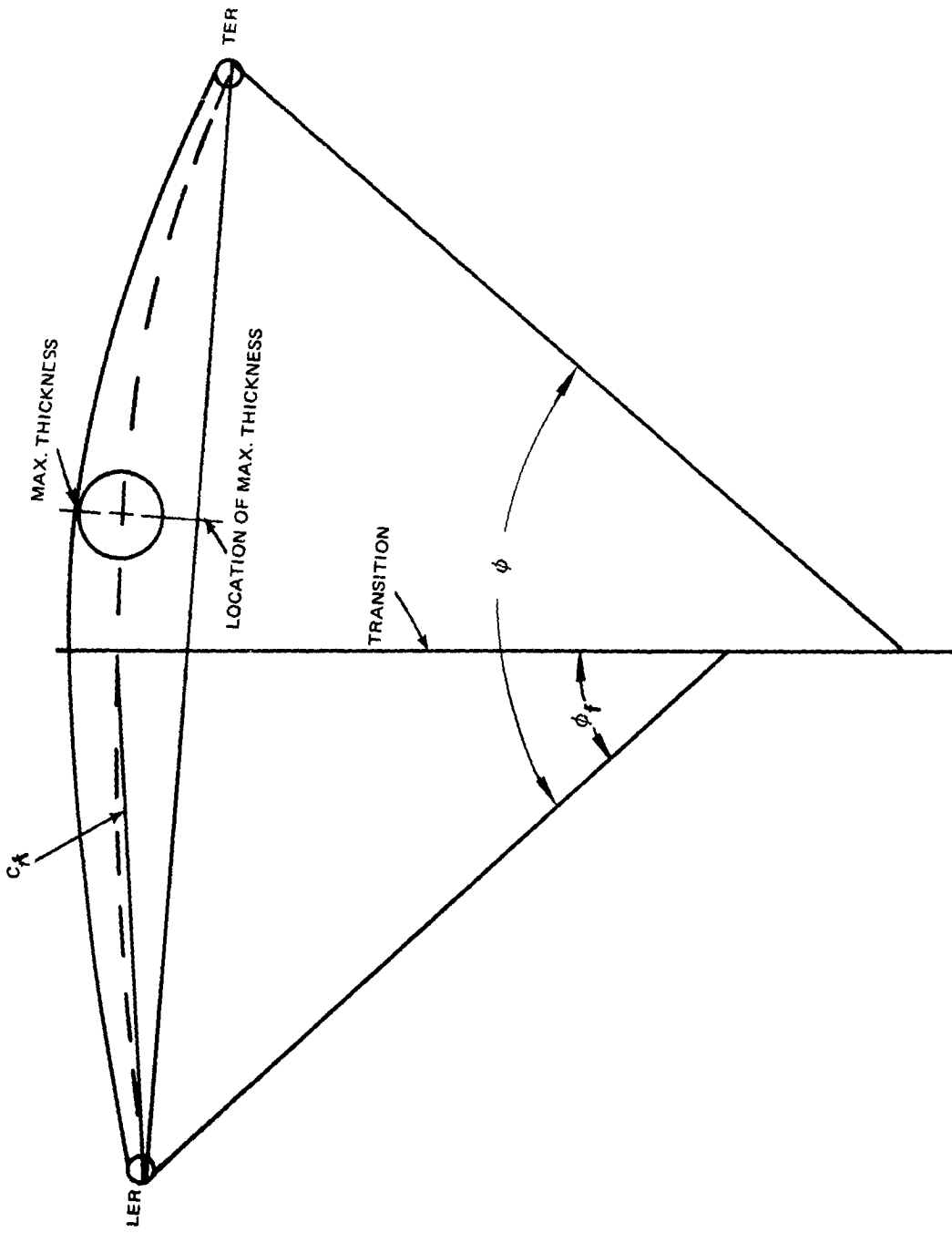
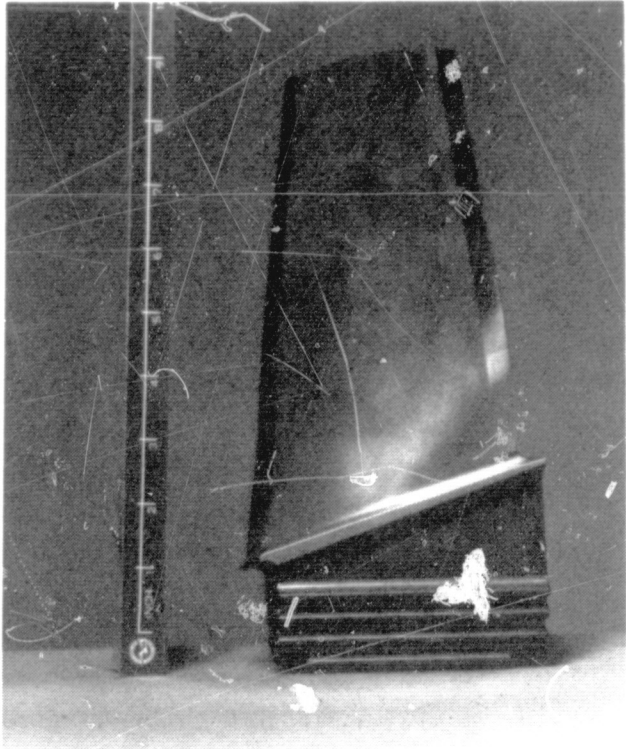
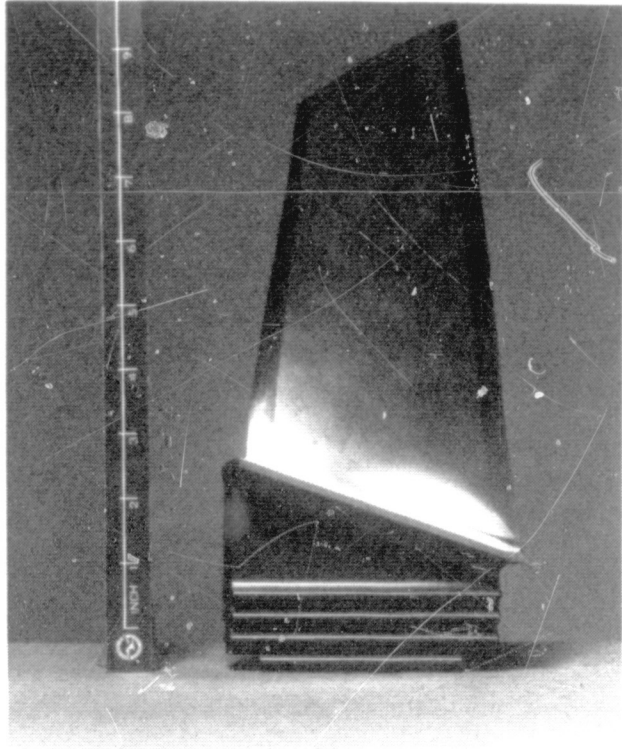


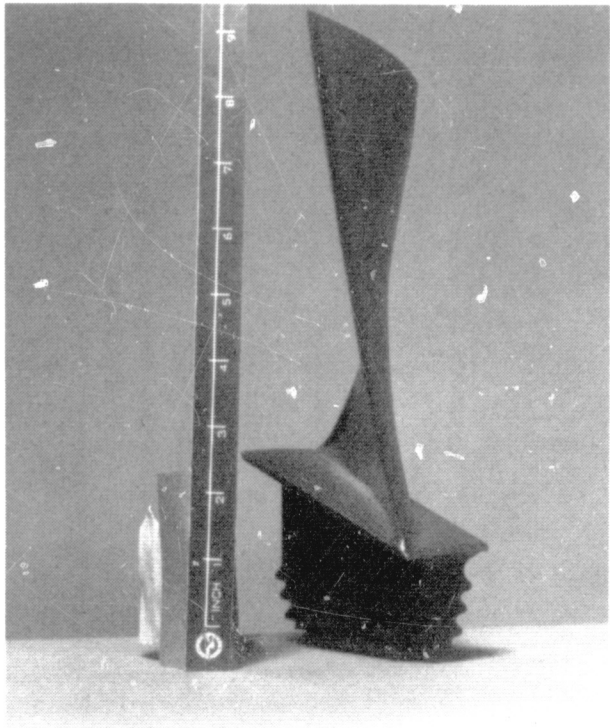
Figure 9 Multiple-Circular-Arc Airfoil Definitions



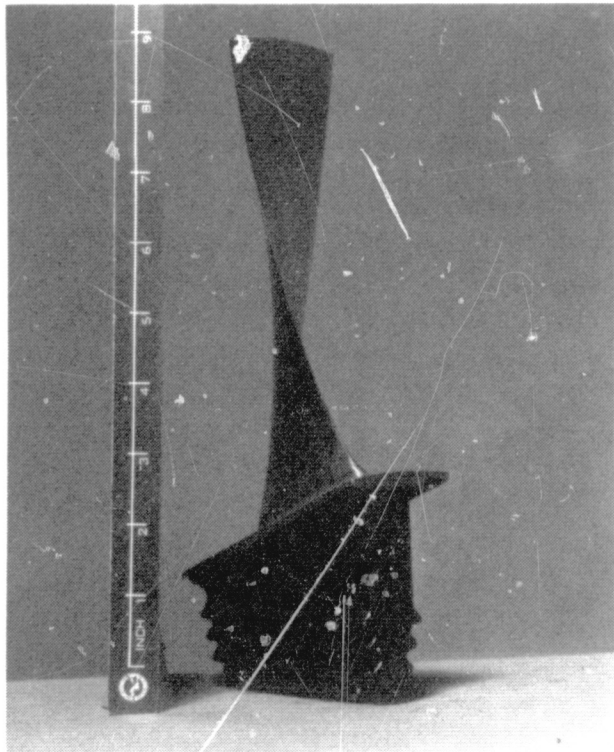
Convex Surface



Concave Surface



Leading Edge



Trailing Edge

Figure 10 Four Views of Rotor

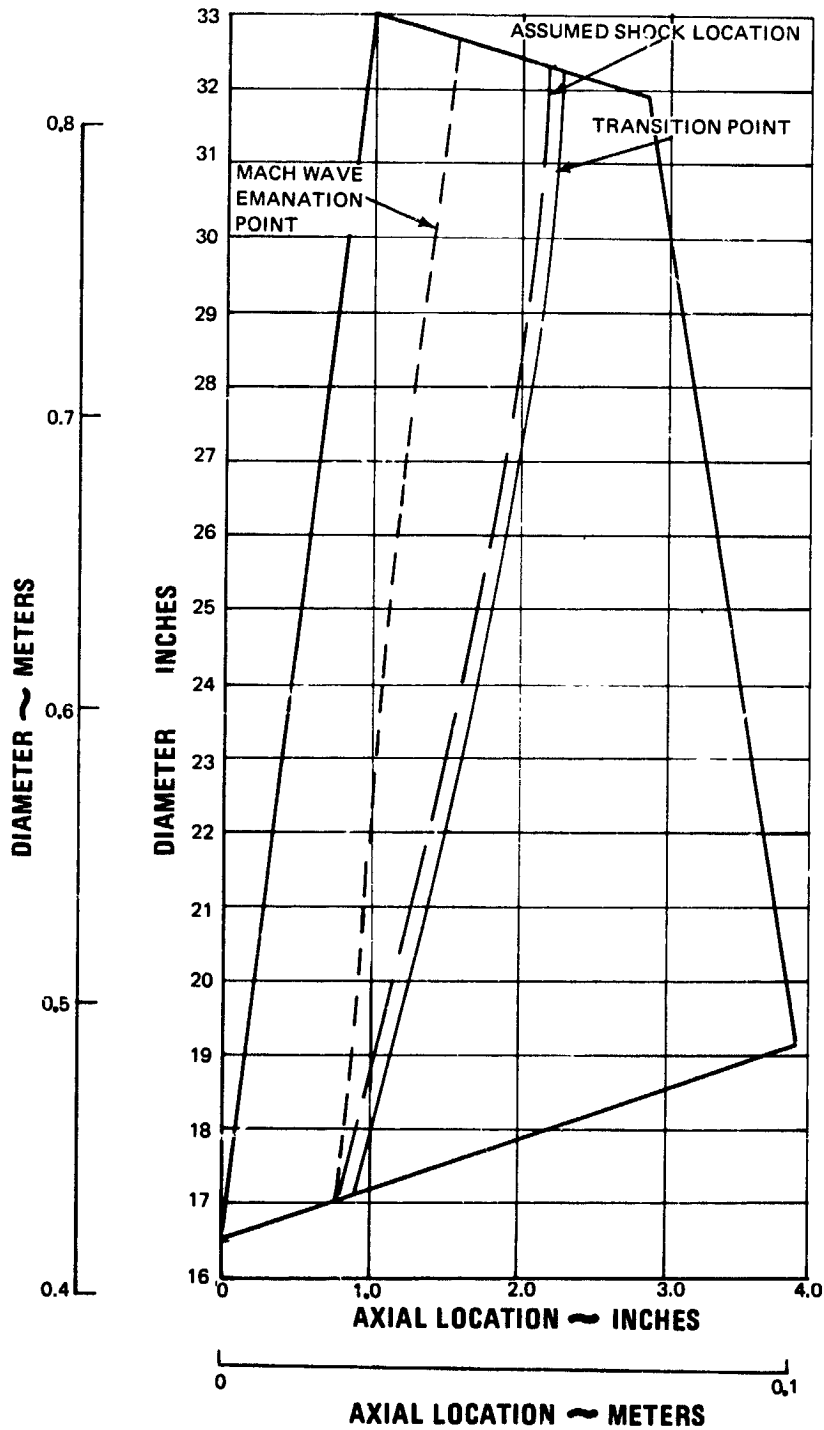


Figure 11 Axial Projection of Rotor

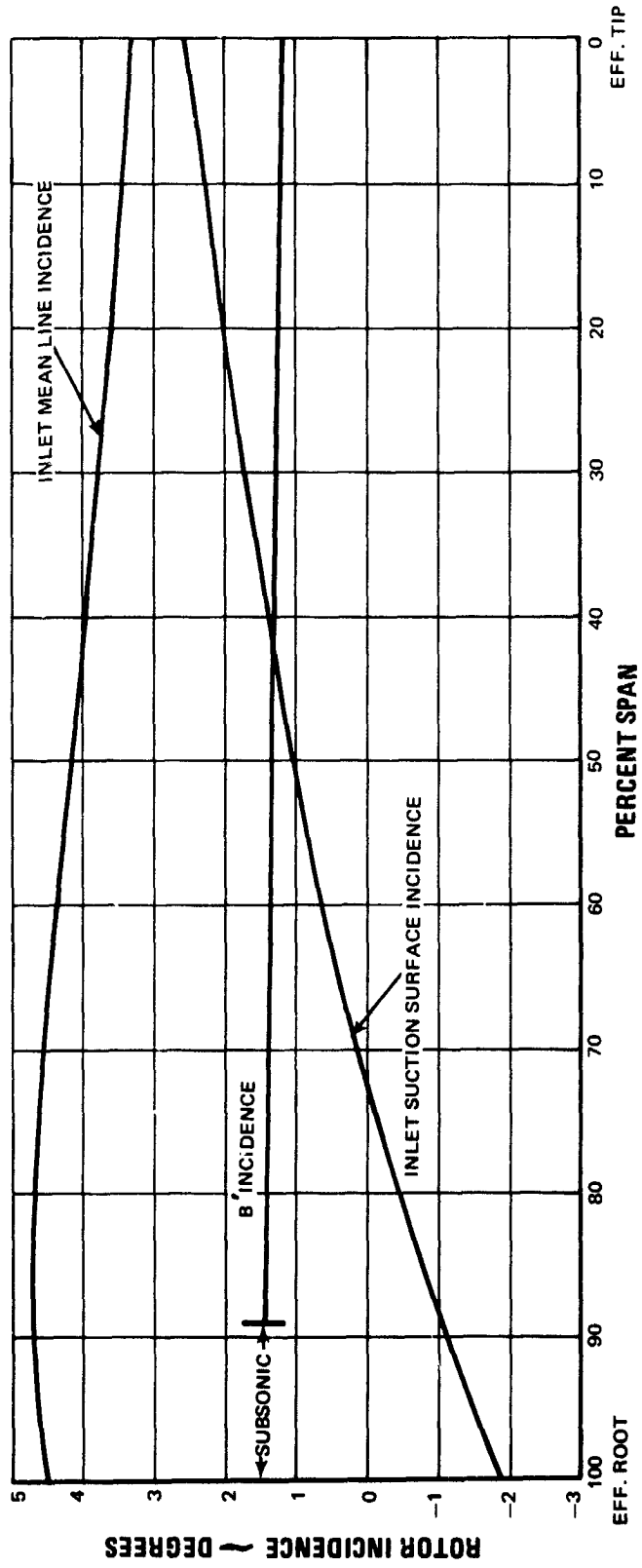


Figure 12 Rotor Incidence

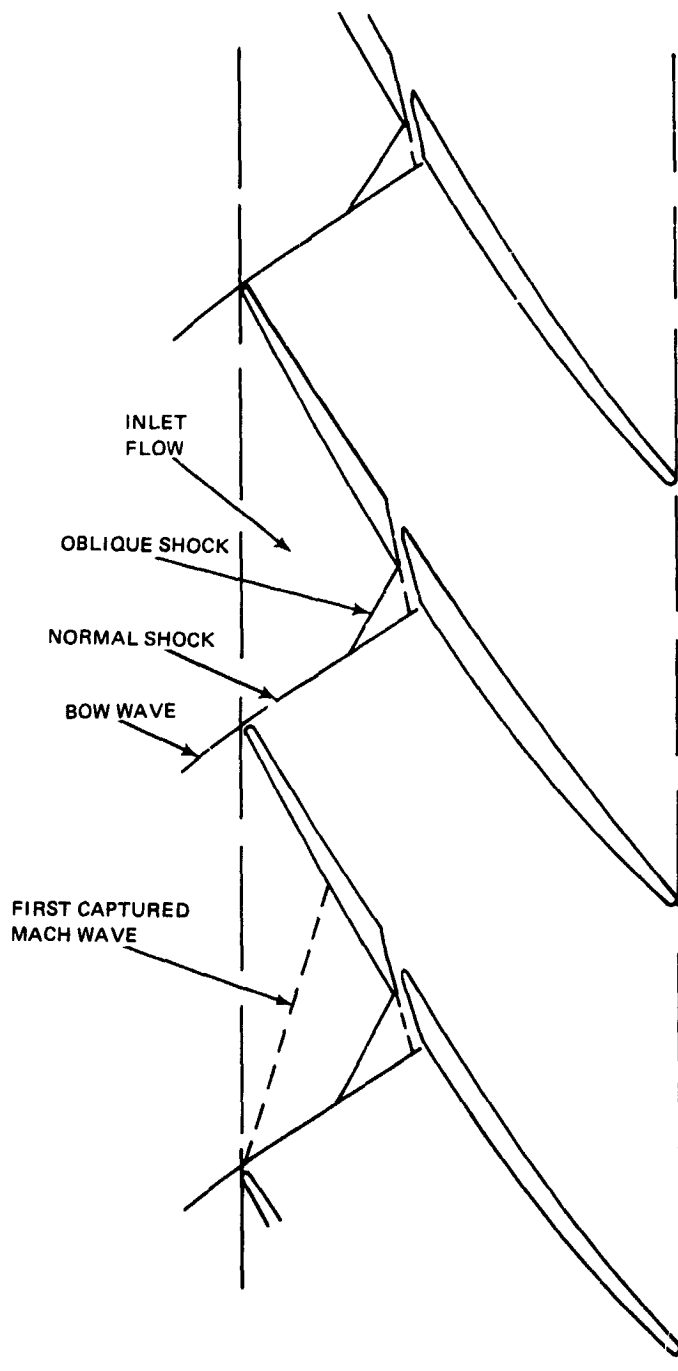


Figure 13 Slotted Rotor Blade Section

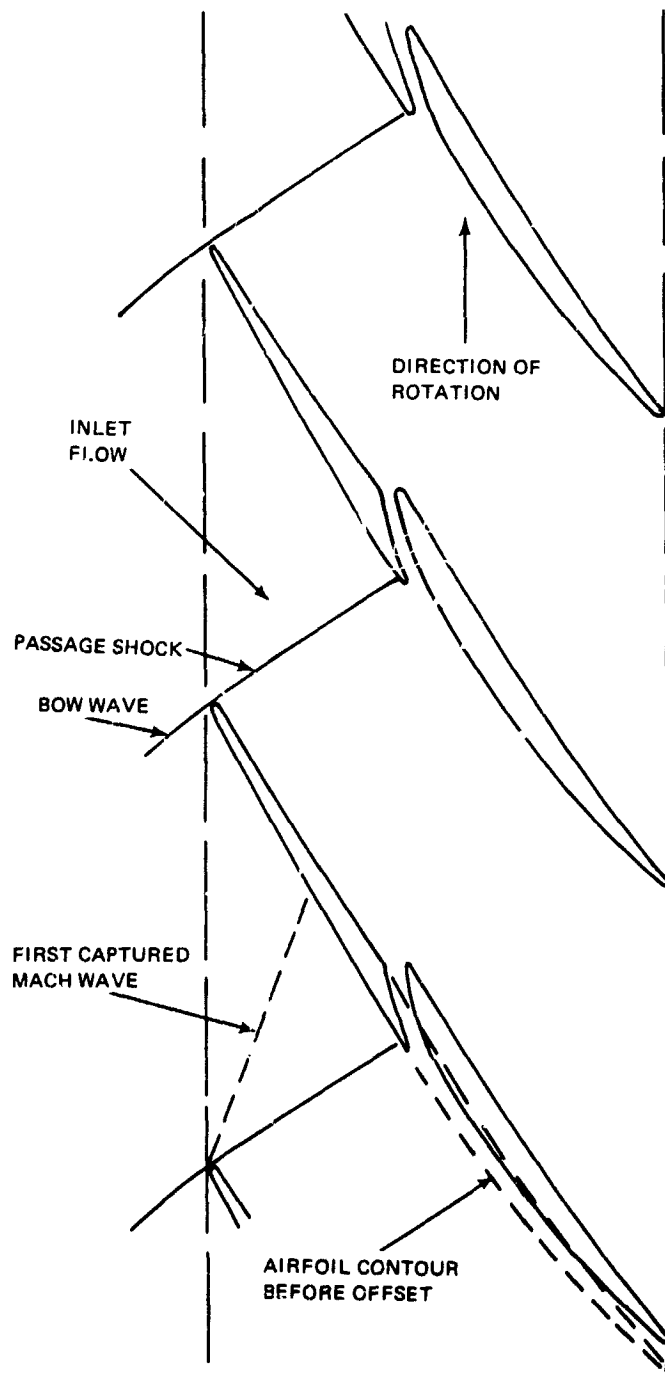


Figure 14 Tandem Rotor Blade Section

The radial distribution of minimum local a/a^* between multiple-circular-arc blades was set between 1.03 and 1.05. The desired throat was obtained by adjusting front camber as discussed in Appendix 4. Because of this a/a^* criterion and the high relative tip Mach number, there is a strong suction-surface compression at the tip. Figure 15 shows the difference between the free-stream air angles if there were no blading, and the suction-surface metal angle at the shock impingement location. Assuming that the flow is attached to the suction surface, Figure 16 shows the change in Mach number at the assumed shock location due to the front camber. There is a maximum increase in Mach number of approximately 0.2 at 90 percent from the tip, and a reduction in tip Mach number of 0.16. The resultant local channel a/a^* through the rotor passage for ten annular stream tubes is shown by Figure 17.

Rear-section camber of the multiple-circular-arc rotor was set to obtain air turning corresponding to the desired work input. Calculations of blade-element deviation required knowledge of solidity, inlet and exit air angles, incidence, and chordwise location of maximum camber. The tip solidity was specified to be 1.3, and solidity between hub and tip was determined by stress and vibration criteria. Inlet and exit air angles were determined by a streamline calculation. Maximum camber point is dependent on deviation, and was determined by an iteration. The ratio of forward chord to total chord was held constant, and the ratio of front camber to total camber was varied to obtain a combination of camber and maximum camber point which produced the desired exit-air angle. Deviation was set by Carter's rule plus an experience factor as discussed in Appendix 5. Deviation versus span is shown by Figure 18. Rearward blade sections of the slotted blade are exactly the same as for the multiple-circular-arc blade. Rearward tandem sections have small differences in suction-surface contour extending from the leading edge of the rear blade to approximately 25 percent chord. Deviation angles are assumed to be the same as for the multiple-circular-arc rotor.

An additional correction was required to compensate for blade untwist due to centrifugal loading. Static blade angles were set so that the untwist at design speed produces the desired operating blade angles. Untwist angles calculated for the slotted blade were the same as for the unslotted blade. Untwist at the tandem blade tip is approximately 0.1 degree less than that for the multiple-circular-arc blade tip. Rotating, as well as static blade angles, are shown by Figure 19. Multiple-circular-arc rotor geometry on the conical surfaces used for design is summarized in Appendix 7.

The slotted and tandem rotor designs were essentially modifications of the multiple-circular-arc design. The slotted rotor aerodynamic design is described in Appendix 8, and the tandem rotor design is described in Appendix 9.

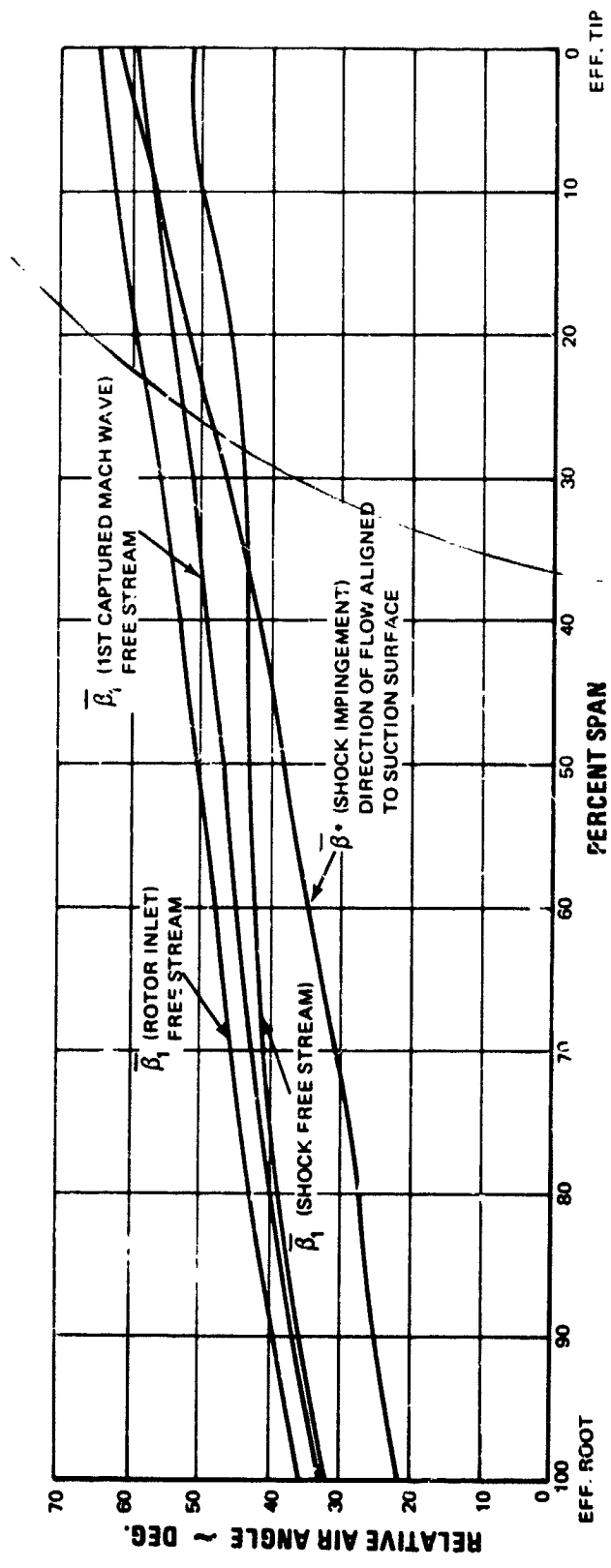


Figure 15 Rotor Entrance Region Relative Air Angle Showing Effects of Annulus Convergence and Front Camber

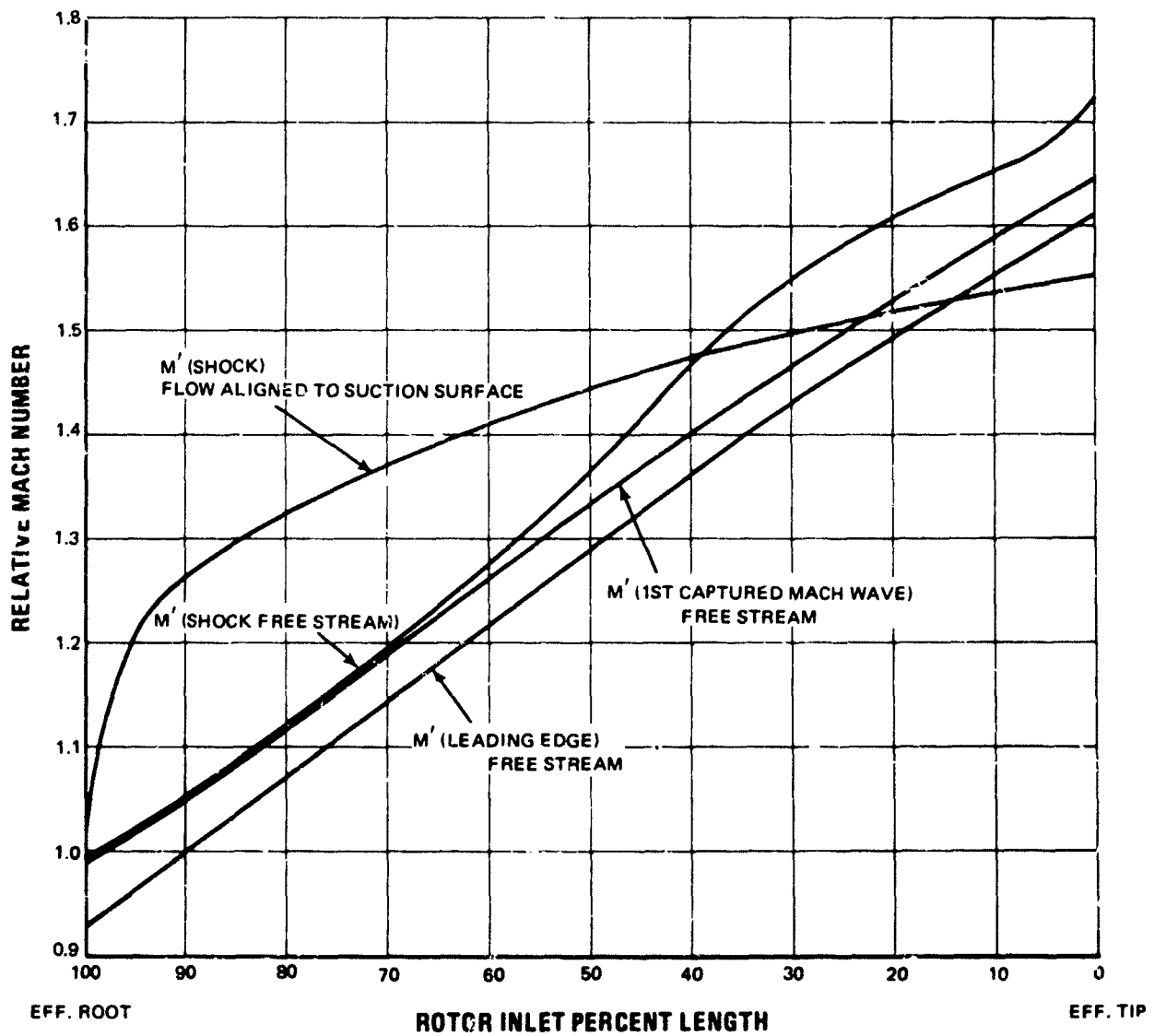


Figure 16 Rotor Entrance Region Relative Mach Number Showing Effects of Annulus Convergence and Front Camber

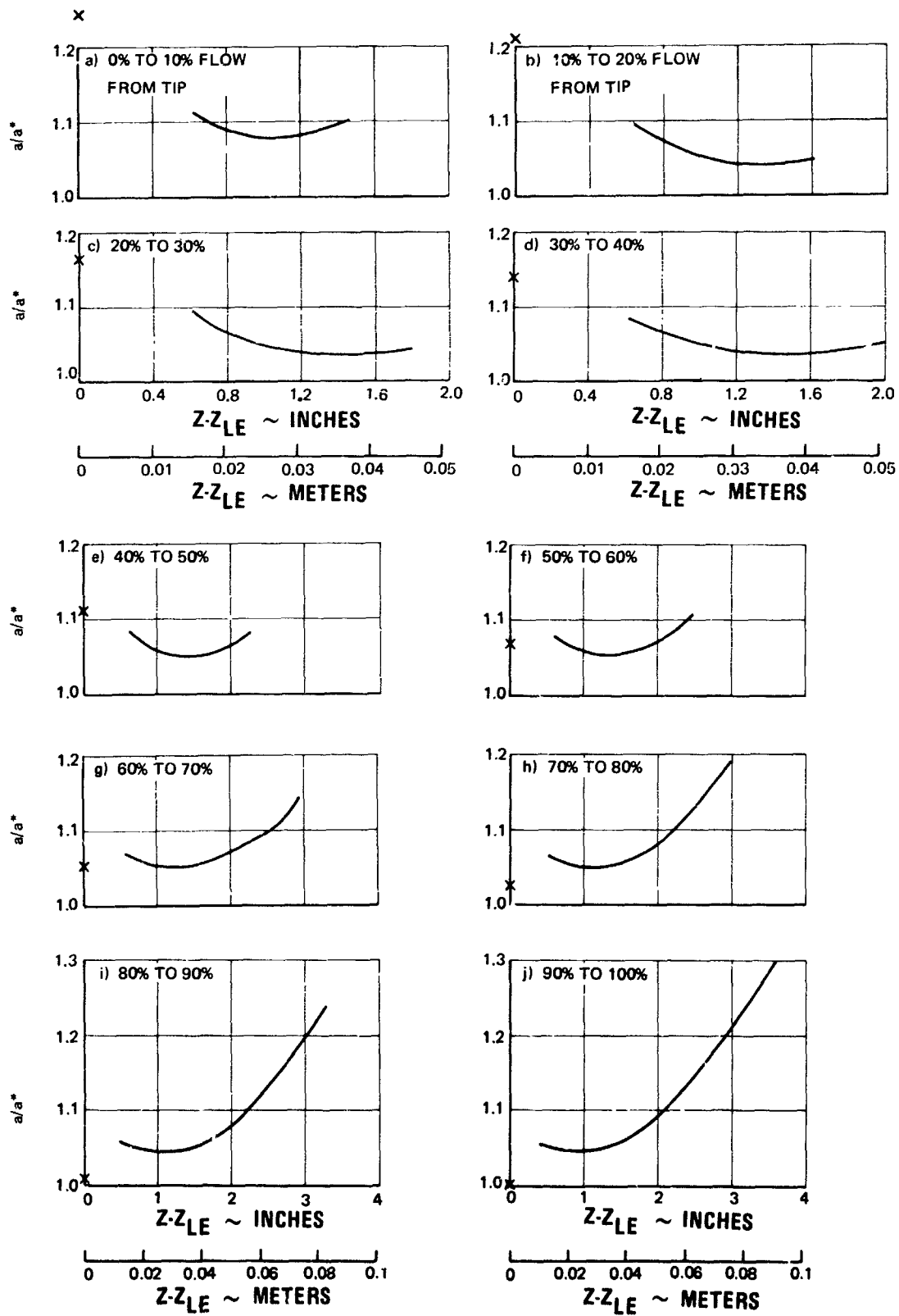


Figure 17 Rotor Spanwise Variation of a/a^*

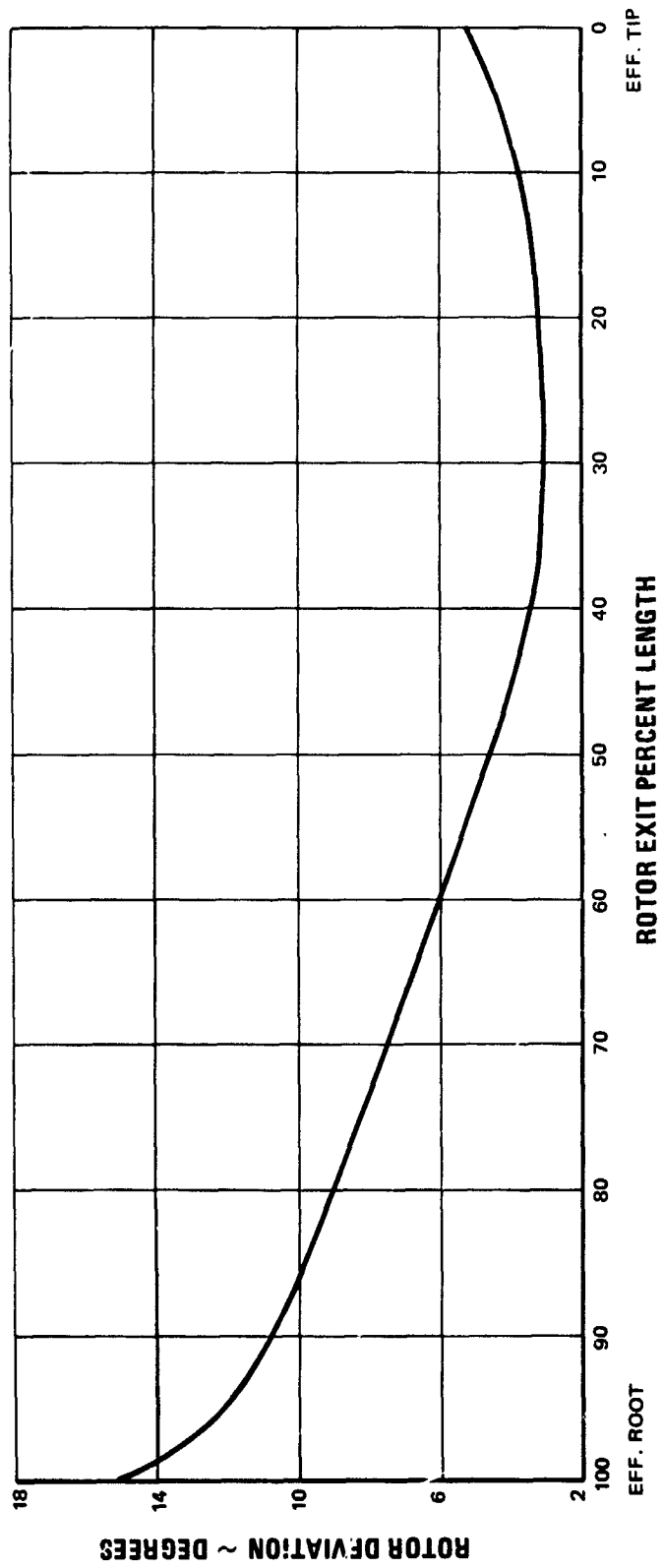


Figure 18 Rotor Deviation

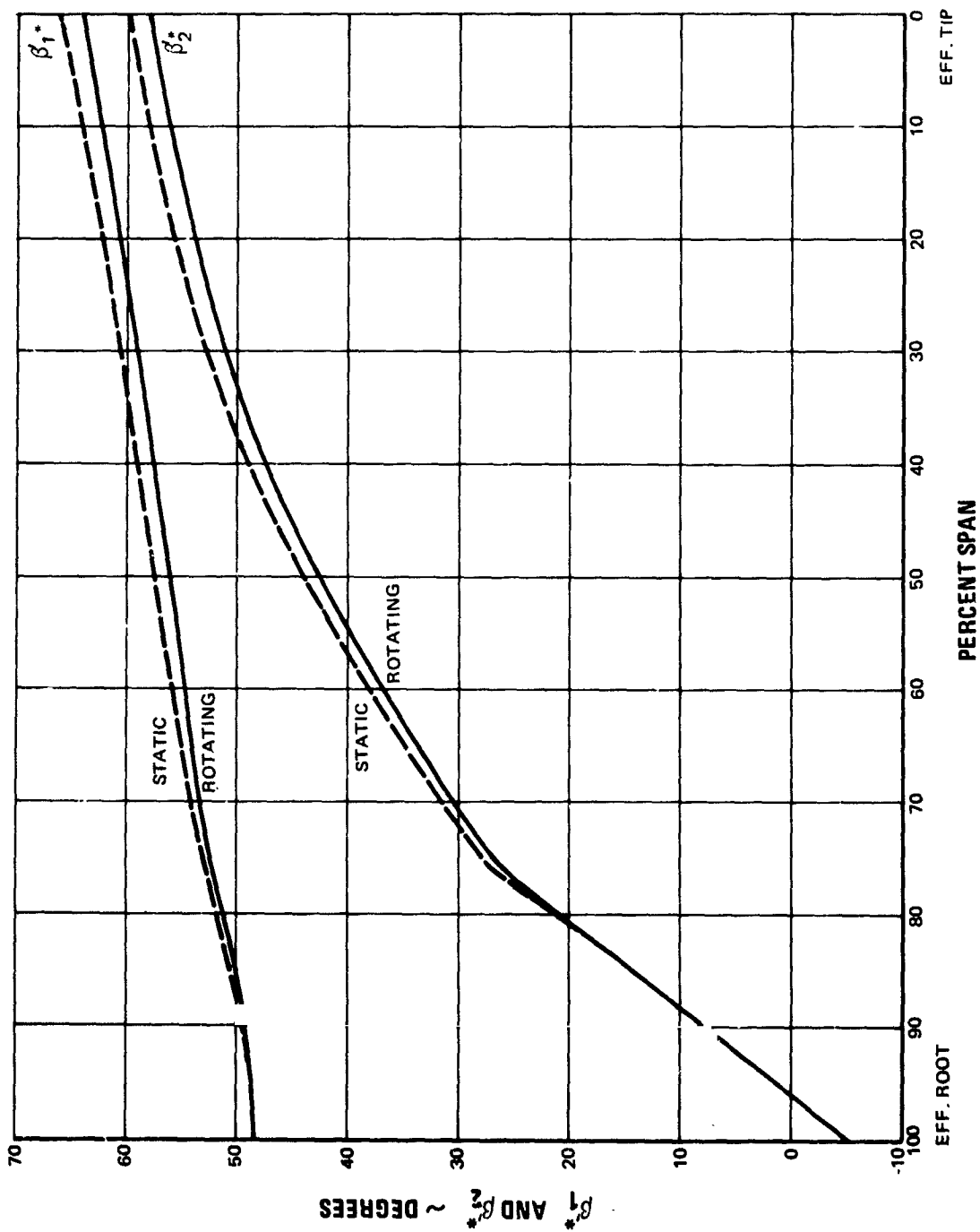


Figure 19 Rotor Inlet and Exit Mean Camber Line Metal Angles on Conical Surface

For manufacturing purposes the airfoil sections were redefined on planes normal to a line termed the stacking line, which is defined as a radial line passing through the center of gravity of the root conical section. A computer program provided a smooth fit of the airfoil properties and produced a set of coordinates for manufacturing purposes. These coordinates are tabulated in Appendix 11.

B. Stator

The stator chord is constant spanwise at 3.0 inches (0.0762 m) and with 44 blades, yields a root solidity of 2.047 and an aspect ratio of 1.72.

The stator is a multiple-circular-arc airfoil, as shown by Figure 9, and is designed on conical surfaces approximating streamlines of revolution. Figure 20 shows several views of the stator.

The stator design criteria were very similar to those of the rotor. The front chord was selected to provide a transition point just aft of the first covered section, as shown by Figure 21, similar to what was done for the rotor.

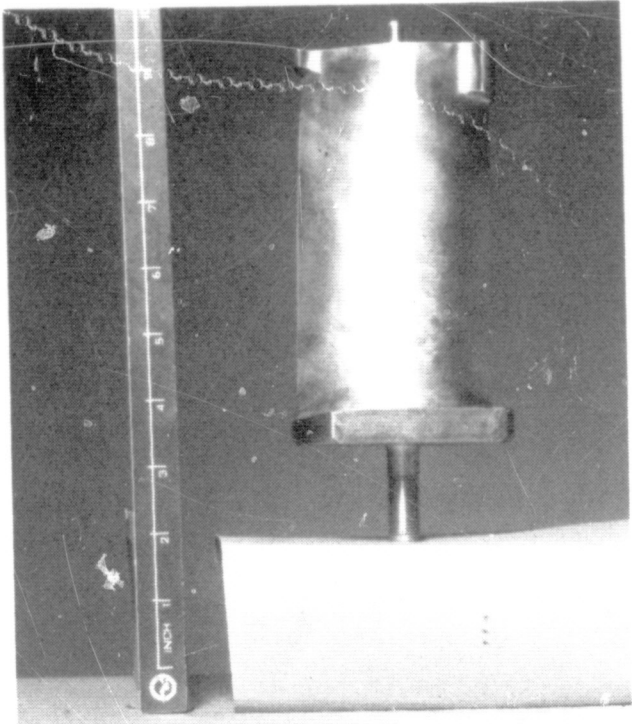
The stator thickness ratio was set to vary linearly from 0.05 at the root to 0.07 at the tip, which should result in low losses and yet be large enough to provide mechanical integrity, as discussed in Section V, below. Maximum thickness was located in the same manner as for the rotor, to provide a minimum wedge angle without a cusp front section.

Incidence was set at roughly zero degrees to the suction surface at the leading edge, as discussed in Appendix 3. Figure 22 shows the stator suction surface and mean camber line incidence.

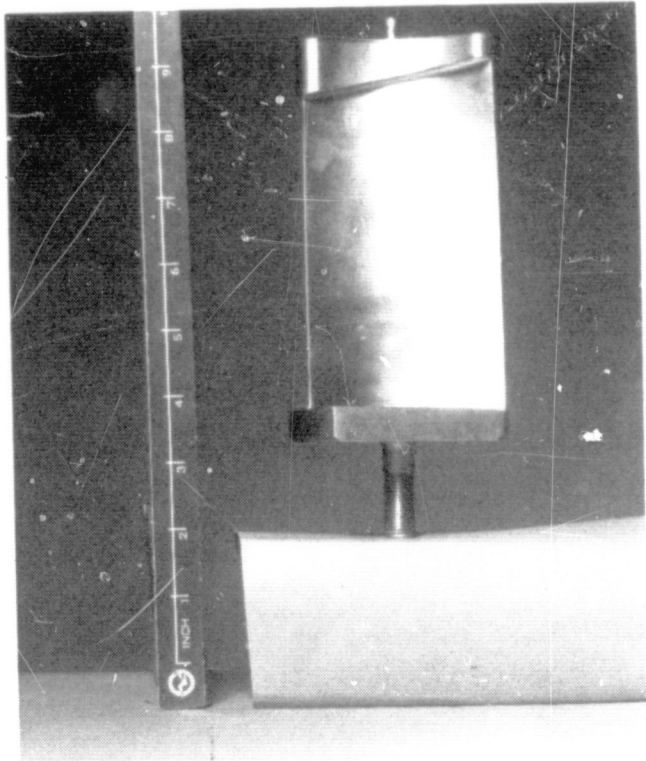
The stator throat a/a^* was set at 1.05 times the a/a^* implied by the inlet Mach number, and is discussed in Appendix 4. Figure 23 shows the local channel a/a^* through the stator passage for ten stream tubes spanwise.

Stator deviations, shown by Figure 24, were calculated using Carter's rule with a correction factor implied by the test results of Reference 5. Appendix 5 discusses the deviation and shows this correction factor to Carter's rule. Figure 25 presents the stator inlet and exit mean camber metal angles spanwise on the conical surfaces used for design.

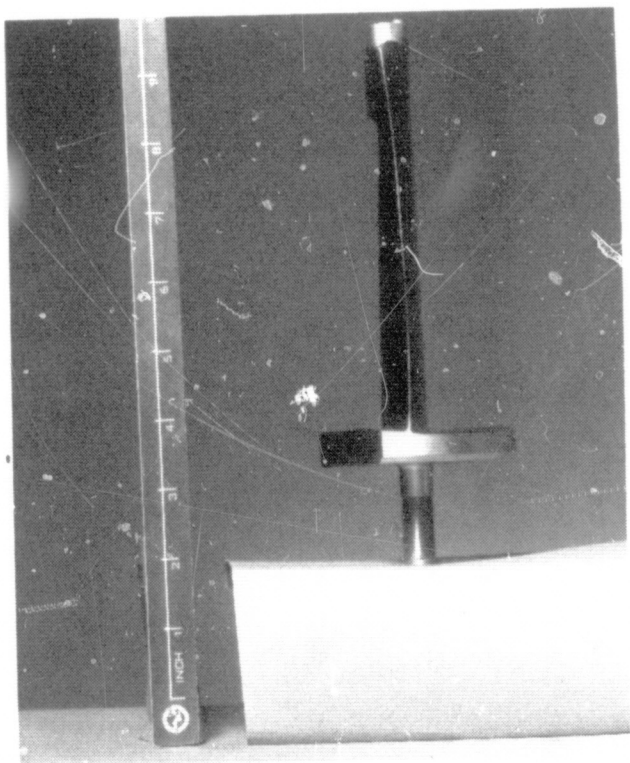
The stator geometry is summarized in Appendix 7 on the conical surfaces used for design. For manufacturing purposes, the airfoil sections were redefined on planes normal to a line termed the stacking line defined as a radial line passing through the center of gravity of the root section on the plane normal to the stacking line. A computer program provided a smooth fit of the airfoil properties and produced a set of coordinates for manufacturing purposes. These coordinates are tabulated in Appendix 10.



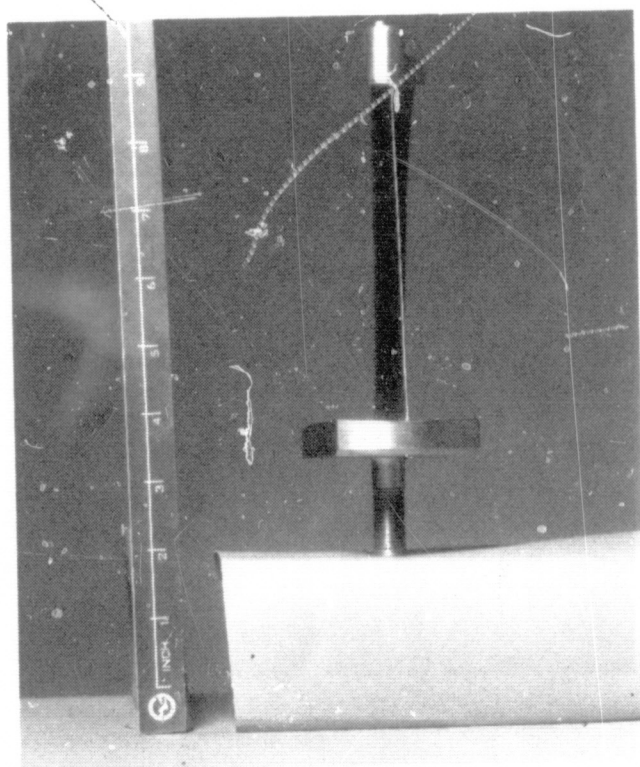
Convex Surface



Concave Surface



Leading Edge



Trailing Edge

Figure 20 Four Views of Stator

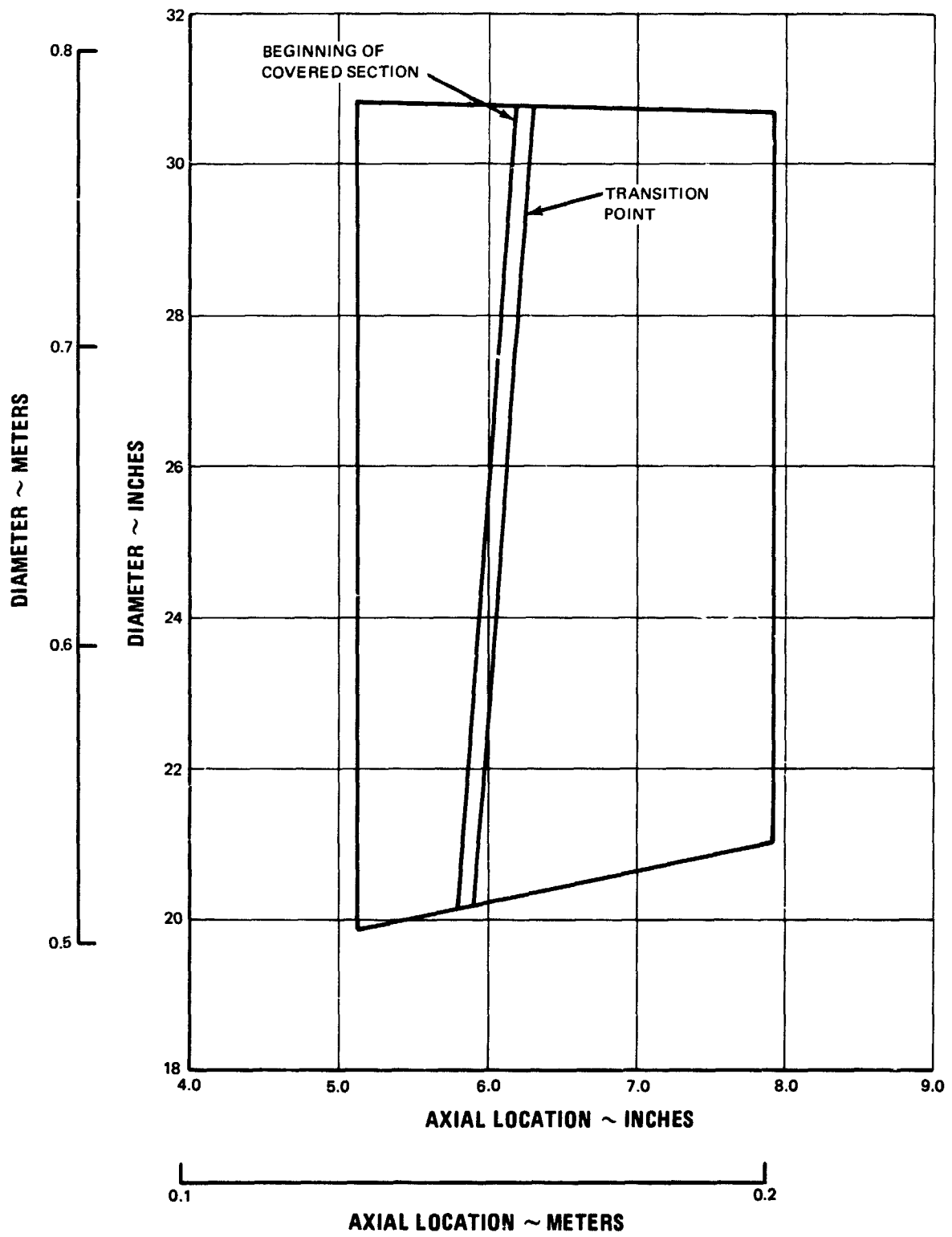


Figure 21 Axial Projection of Stator

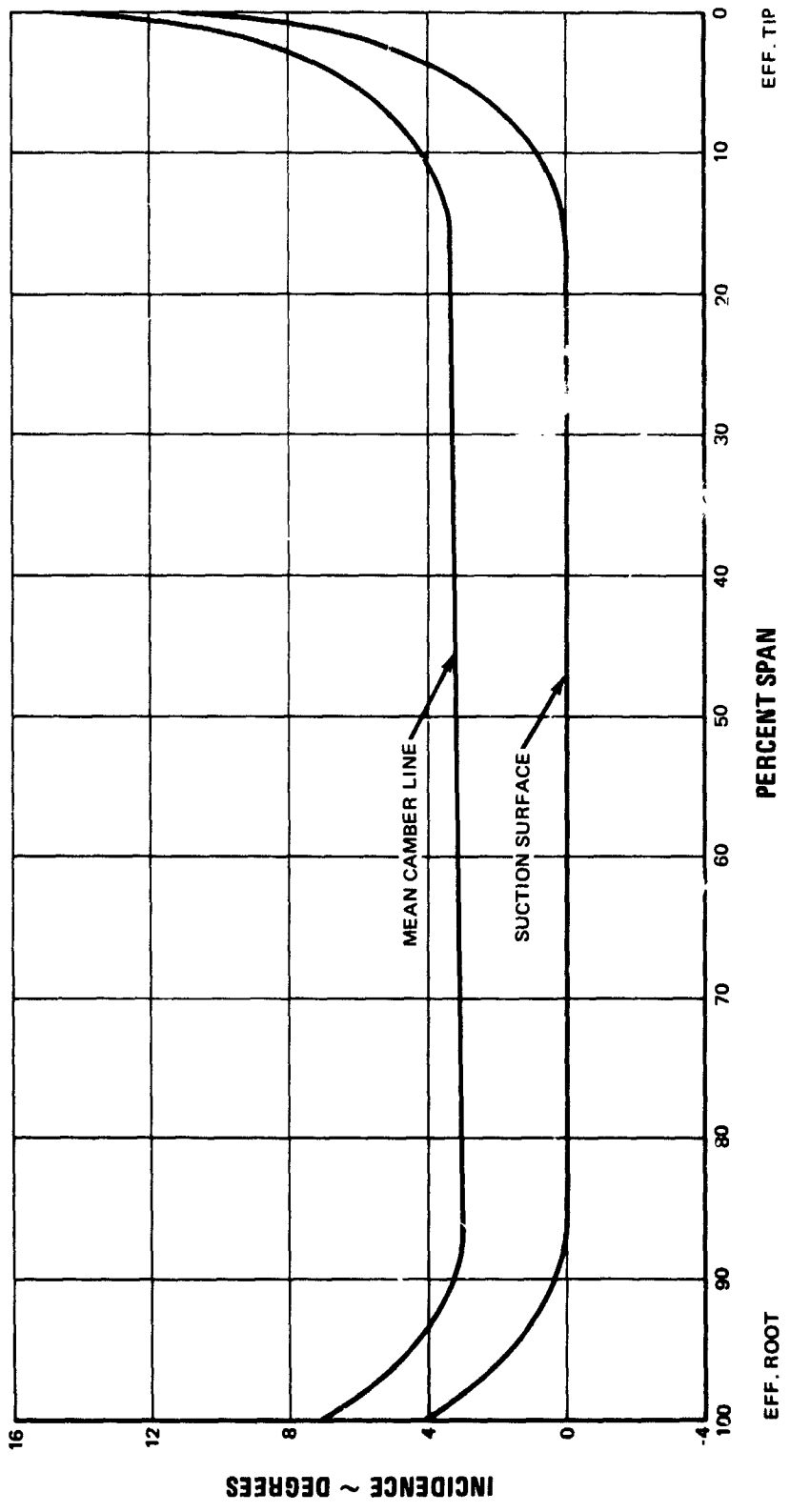
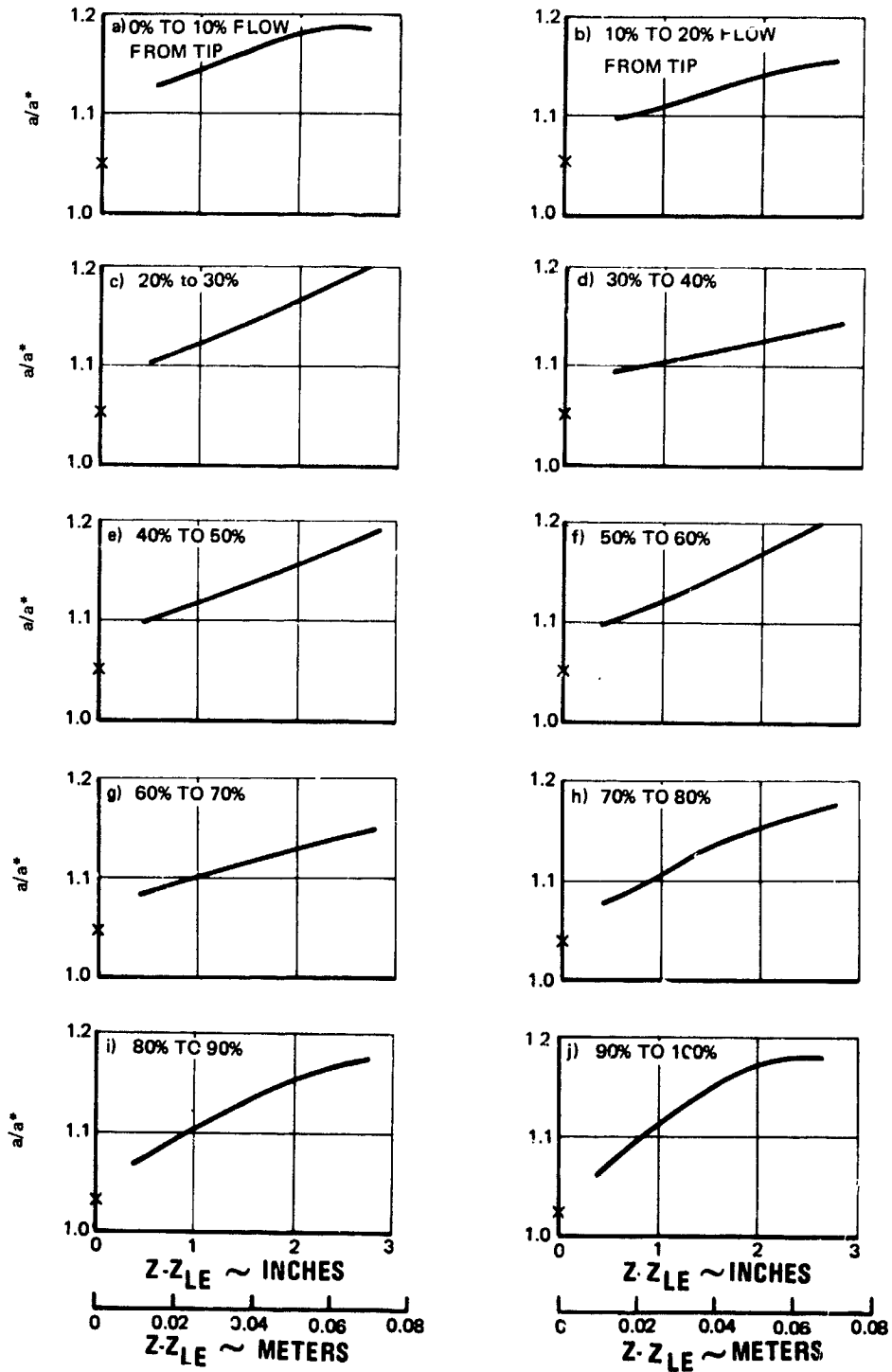


Figure 22 Stator Leading-Edge Suction Surface and Mean Camber Line Incidence



Note: $\times = a/a^*$ at stator inlet Mach number

Figure 23 Stator Spanwise Variation of a/a^*

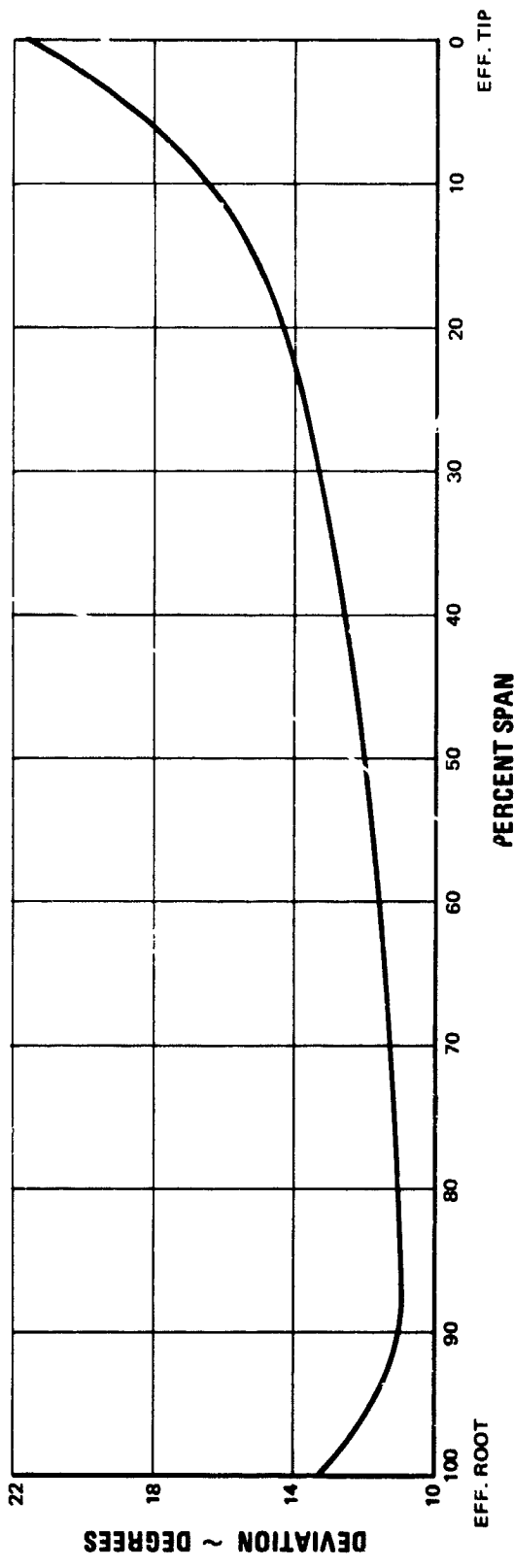


Figure 24 Stator Deviation

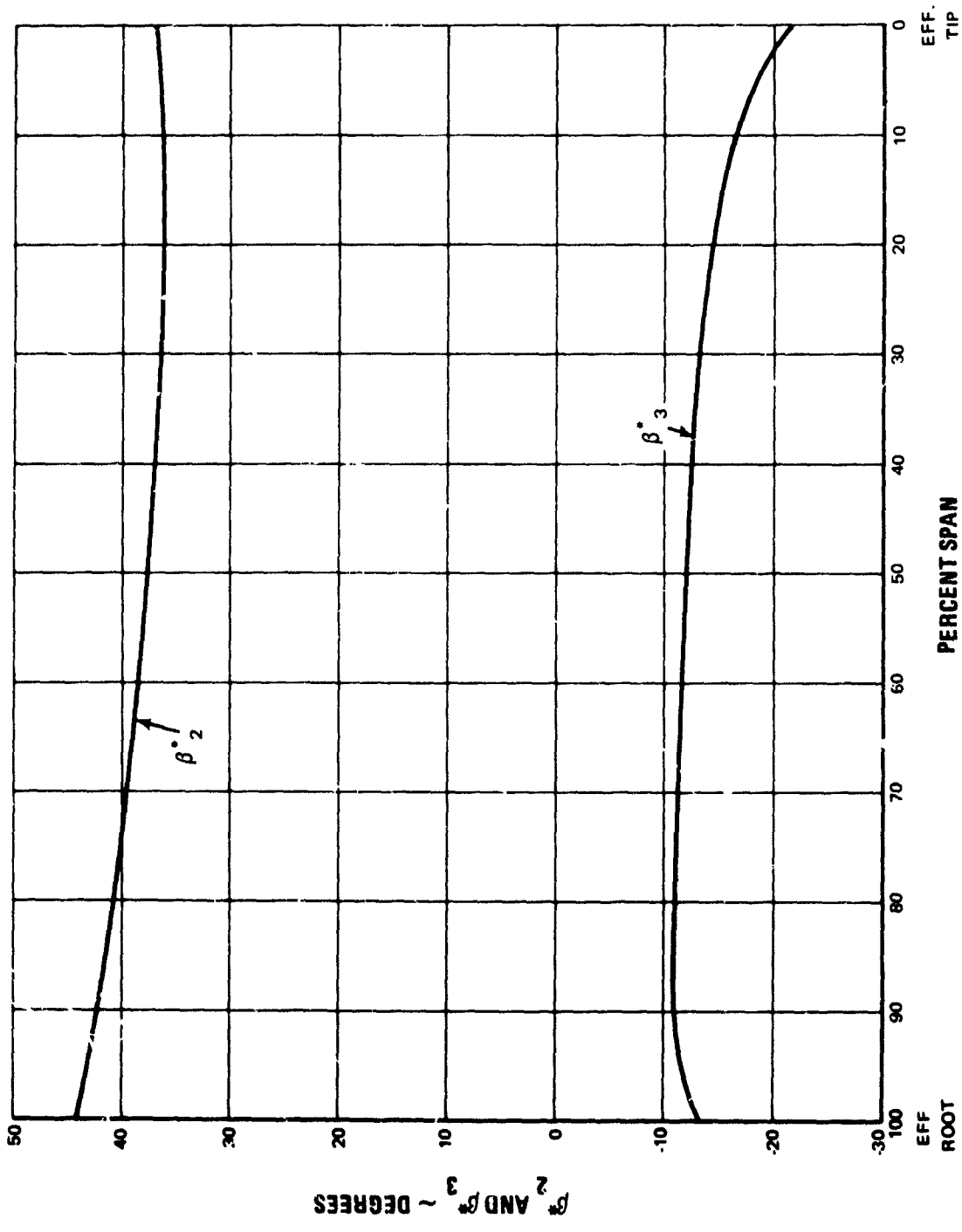


Figure 25 Stator Inlet and Exit Mean Camber Line Metal Angles on Conical Surface

C. Stator Slit Design

In order to reduce total pressure losses and attain higher lift coefficients in axial flow turbomachinery, it is necessary to prevent end-wall boundary-layer separation. Data from Reference 5 show that losses in the end-wall region limit stator loadings. Other experimental data⁶ show that substantial improvements in performance (2 points in efficiency) can be gained by applying boundary-layer control in the corner of a blade or vane surface and the annular wall or casing. Peacock⁶ reduced compressor cascade losses significantly by extracting a small amount of flow through a slit at the intersection of the wall and blade suction surface. His data were analyzed and slit design criteria were developed. It was found that most of the attainable benefit was obtained by bleeding off the flow common to displacement thickness growths on the vane surface and the wall. This is the flow in which the direct and turbulent dissipation of kinetic energy is greatest⁷. As shown in Figure 26, a slit width greater than the width of this critical region requires an increased flow rate to eliminate separation.

With flow rate determined by slit width, many combinations of slit length and flow velocity are possible. In this design, the slit extends from 15 percent to 85 percent of chord. This is further forward than the optimum configuration reported in Reference 6, but it provides suction closer to the minimum pressure point, and covers the area of possible shock impingement during transonic operation. Sonic bleed velocity was selected to prevent recirculation. A slit width of 0.025 inch (0.000635 m) was selected to provide an adequate margin between slit flow capacity and the calculated flow rate to prevent separation.

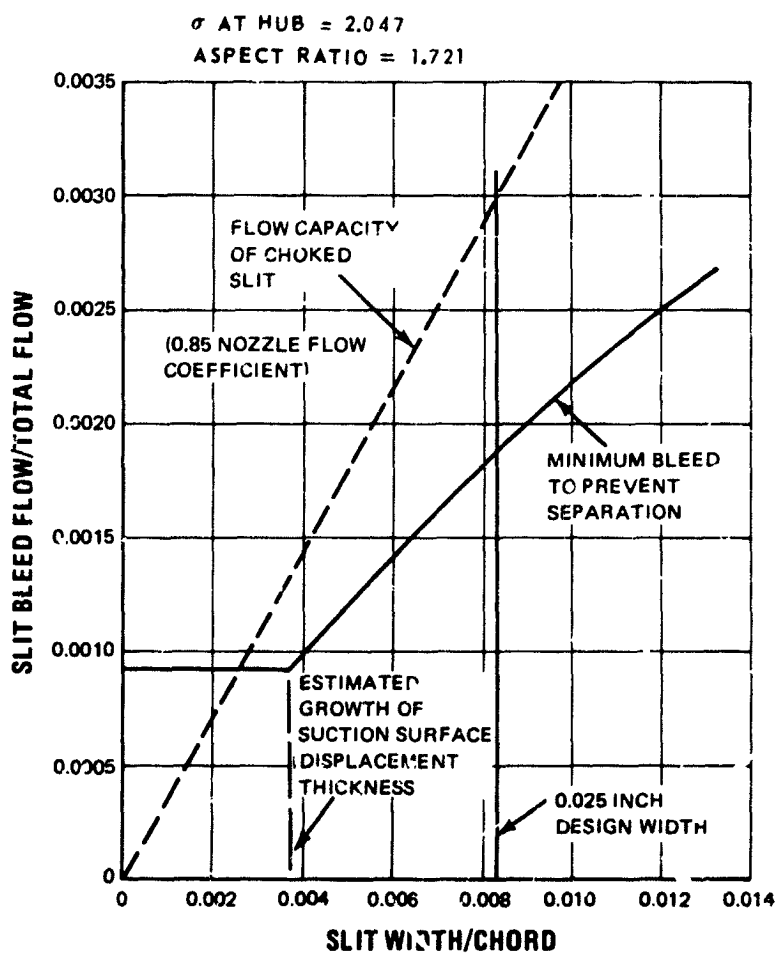


Figure 26 Slit Flow to Prevent Corner Separation at Intersection of Stator Suction Surface and Hub Wall

V. STRUCTURAL AND VIBRATION ANALYSIS

Two major problem areas that the rotor blade mechanical design was tailored to avoid were first-mode bending resonance with two excitations per revolution and static stress due to blade untwist at high speeds.

A. Blade and Disc Vibration

Because circumferential distortion testing requires operation in an environment of two excitations per revolution, it was mandatory that there be no 2E resonances in the operating range. Airfoil spanwise length was set at the minimum allowed by the contract with an inlet hub/tip ratio of 0.50. A parametric study of vibration frequency as a function of blade aspect ratio was made, with root maximum thickness-to-chord ratio set at 0.10. An aspect ratio of 1.663 gave its lowest natural frequency (first bending mode) higher than the frequency of two excitations per revolution at 110 percent of design speed. To avoid a large drop in frequency from dovetail root and disc flexibility, a firtree attachment was used in conjunction with a large steel disc. The resultant overall first bending mode resonance frequency margin at 110 percent of design speed is 7 percent, which is considered adequate. The frequency-speed diagram is shown in Figure 27.

B. Blade Stress

Combined centrifugal pull and untwisting stresses were calculated at 110 percent of design speed. A comparison was made to allowable stresses based on AMS 4928 titanium alloy at 150°F (338.7°K).

There are two spanwise maximum stress locations, the root section which has local high stresses at the leading and trailing edges, which from past experience is not a problem, and the 90 percent span combined stresses. The combined stresses at 90 percent span and 110 percent of design speed for the final design with 0.5 hub/tip ratio and 0.10 t/c ratio were calculated to be 74,000 psi (52,029,000 kg/m²), which is well below the 0.2 percent yield strength of 116,000 psi (81,560,000 kg/m²).

Gas bending stresses with centrifugal restoration were calculated at design speed for various tangential tilts (Figure 29). Airfoil stresses were minimized for the combination of load and no-load conditions. The selected tangential tilt is 0.034 inch (0.000864 m), which results in a maximum bending stress of 3800 psi (2,672,000 kg/m²).

The first bending mode maximum-vibratory-stress location is at the root trailing-edge position. The 90 percent span location is predicted to have only 32 percent of vibratory stress in first mode compared to the root trailing edge, as shown by Figure 28.

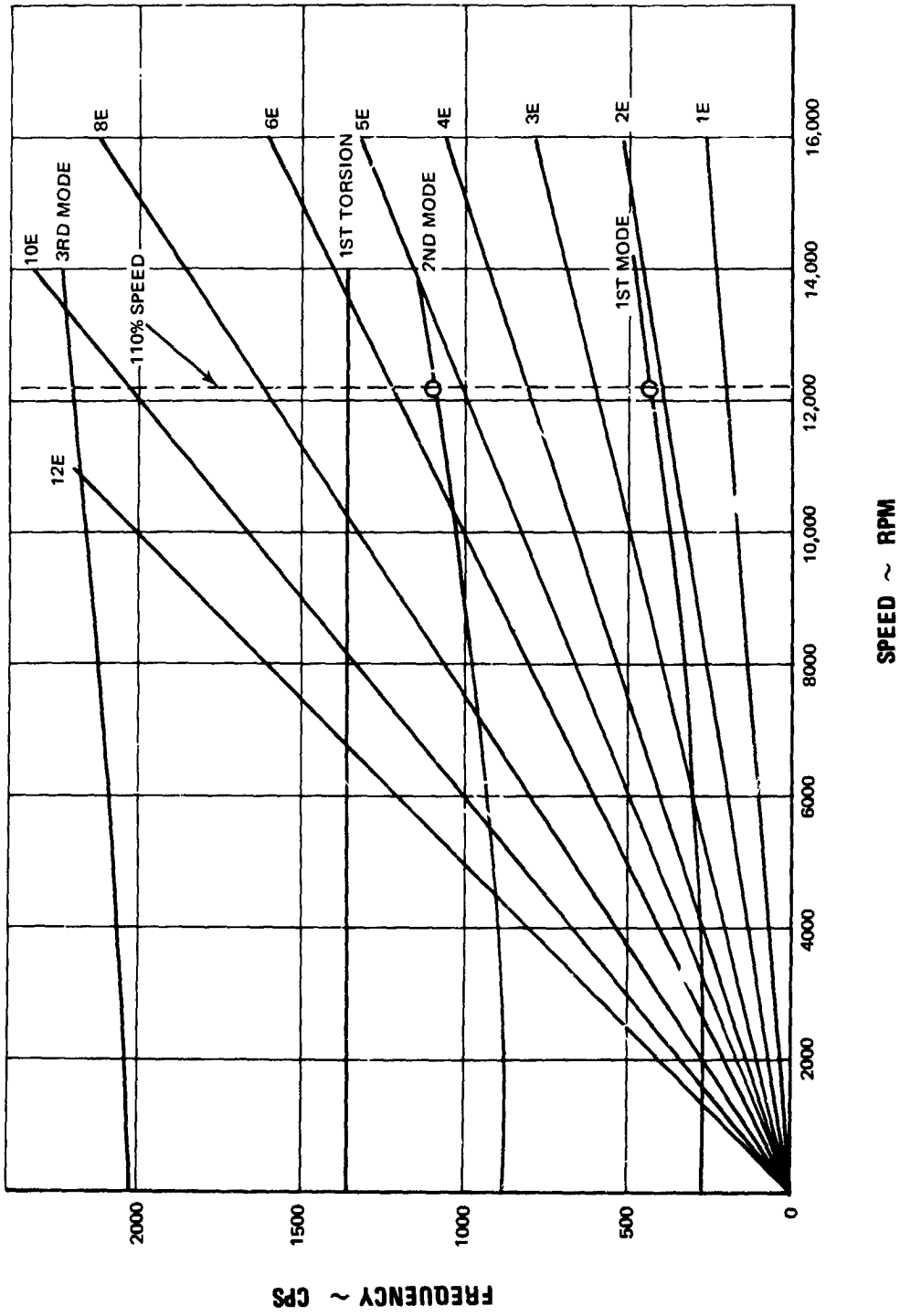


Figure 27 Blade and Disc Resonance Diagram

ROTOR SPEED = 12,221 RPM (110% DESIGN)

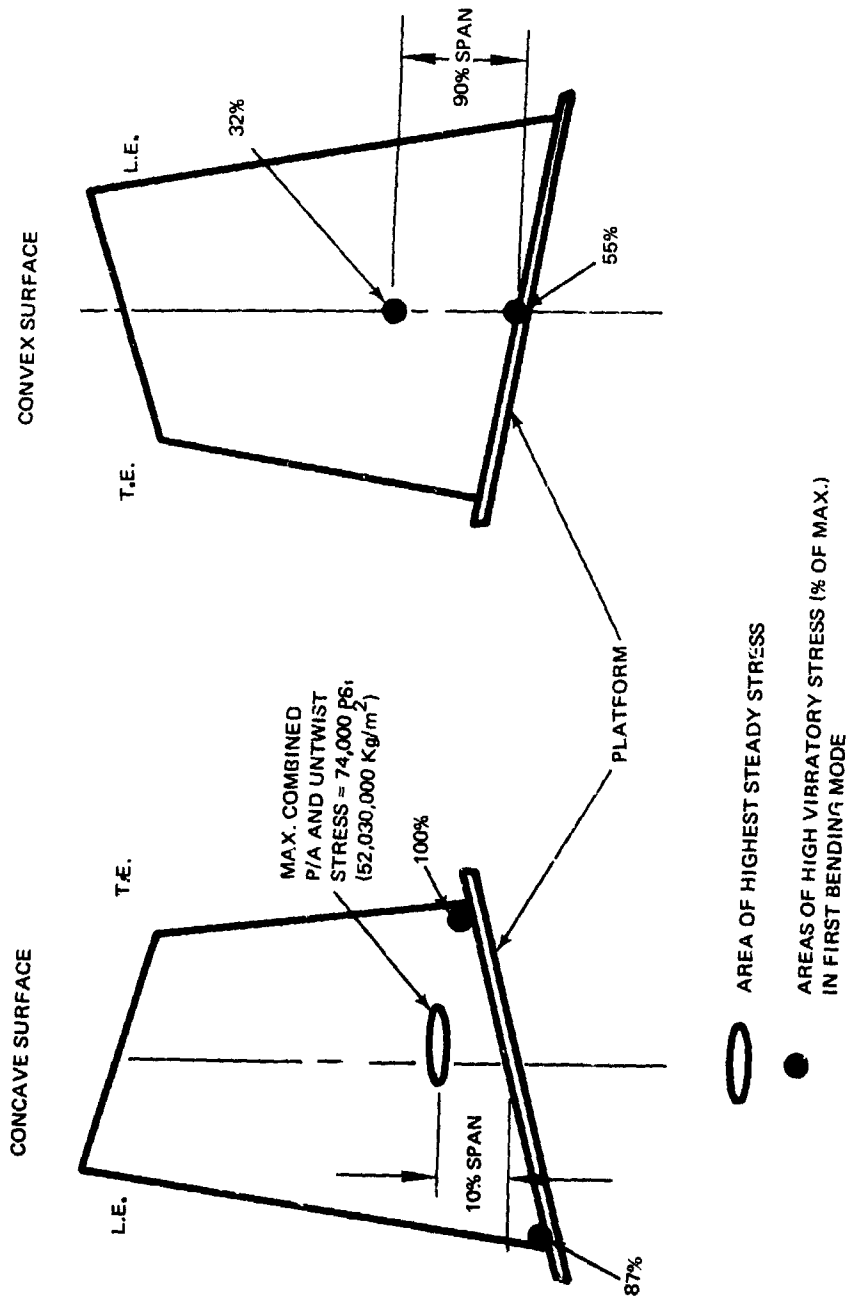


Figure 28 Maximum Stress Locations

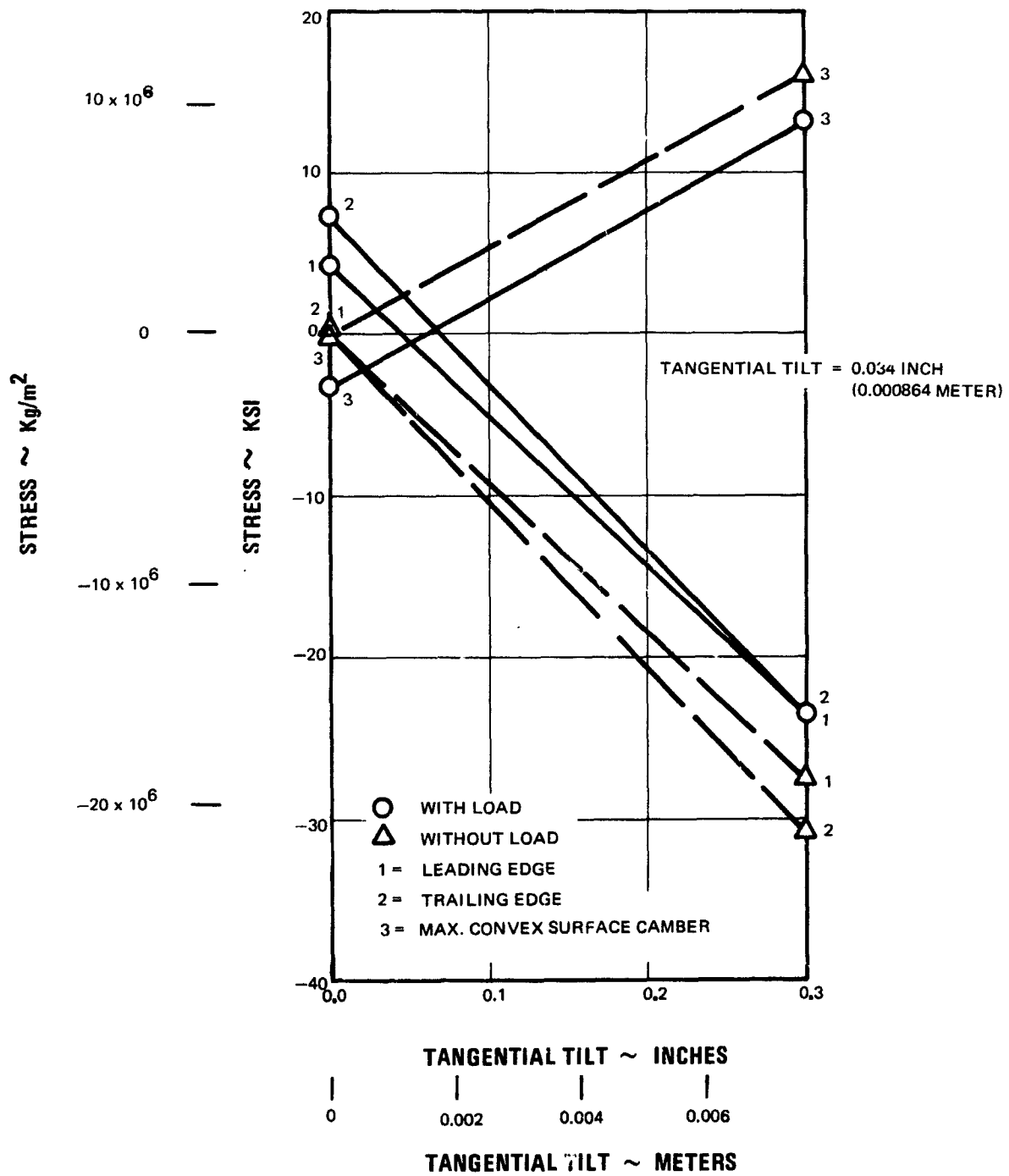


Figure 29 Effect of Tangential Tilt on Rotor Gas Bending Stress

A Goodman diagram was developed for the blade material at 150°F (338.7°K) and is presented in Figure 30. The maximum allowable continuous vibratory stress is 10,000 psi (7,031,000 kg/m²). Since critical resonances were removed from the operating range, vibratory stress levels should be less than 10,000 psi (7,031,000 kg/m²) and the rotor should have satisfactory fatigue characteristics. The rotor and stator stresses are summarized in Table 3.

TABLE 3

Rotor and Stator Stresses		
	<u>Rotor</u>	<u>Stator</u>
material	AMS 4928	AMS 5613
number of airfoils	30	44
rotor speed (110 percent), rpm	12,221	-
root centrifugal force, lb	45,600 (20,684 kg)	-
root centrifugal (P/A) tensile stress, psi,	36,000 (25,311,000 kg/m ²)	-
maximum gas bending stress at 100 percent speed, psi	3,800 (2,672,000 kg/m ²)	3,815 (2,682,000 kg/m ²)
tangential tilt, inches		
tip	0.034 (0.00964 m)	-
root	0 (0m)	-
10 percent span above platform, airfoil P/A + untwist tensile stress, psi	74,000 (52,029,000 kg/m ²)	-
0.2 percent yield strength, psi	116,000 (81,560,000 kg/m ²)	110,000 (77,341,000 kg/m ²)

C. Torsional Blade Flutter

The torsional flutter parameter $V/b\omega_t$, (where b is the blade semi-chord at 75 percent span and ω_t is the torsional frequency) was calculated for the rotor blade. For these blades, the torsional flutter parameter is 0.932, which is well below typical values where flutter problems occur.

Torsional flutter stability was brought about through minimizing the flutter parameter by increasing airfoil root thickness. The thickness-to-chord ratio at the airfoil root and tip are 0.100 and 0.025 respectively. The thin tip section was set primarily by aerodynamic considerations, but sufficient thickness was used to avoid panel flutter.

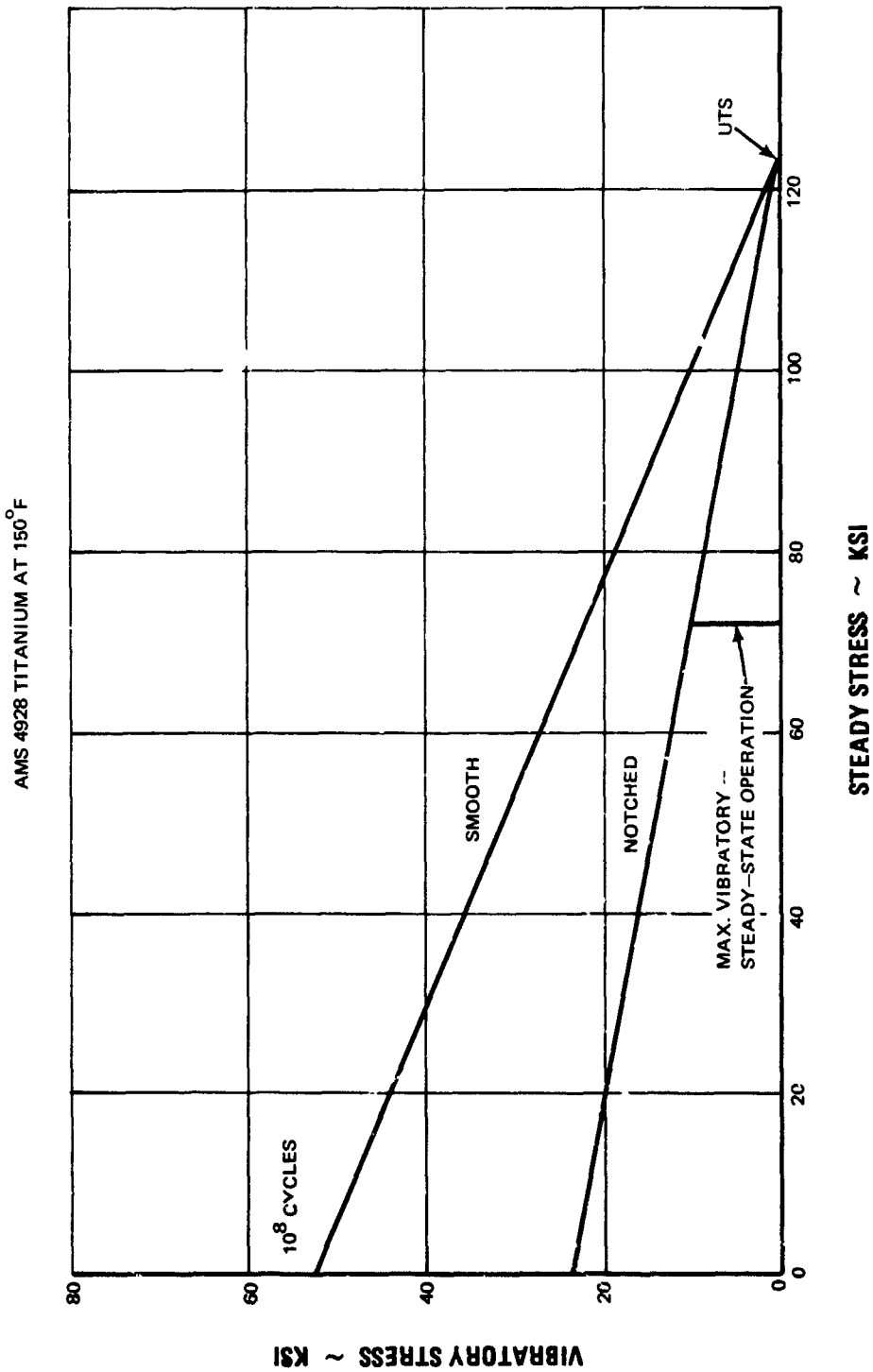


Figure 30 Rotor Goodman Diagram

D. Disc and Attachment Stresses

A firtree root attachment was used as discussed previously to provide a rigid root attachment and obtain adequate 2E margin. A conventional dovetail type of root attachment would have caused a fifty percent reduction in 2E margin. Table 4 summarizes the disc and attachment stresses.

TABLE 4
Disc and Attachment Stresses

Assumed Operating Conditions:

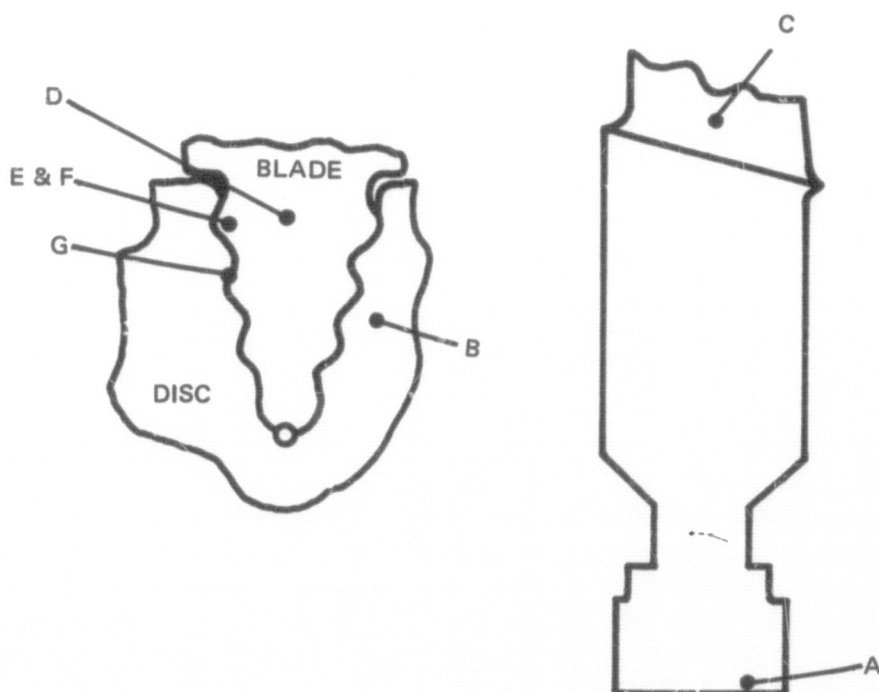
N = 12,220 rpm (110 percent of design speed)
 T = 200°F (366.5°K) (no radial temperature gradient)
 pressure difference across disc = 1.5 psi (1054.7 kg/m²)
 total disc rim load = 3,845,800 lb (1,744,470.0 kg)

Materials:

disc AMS 6415
 blade AMS 4928

<u>Location</u>	<u>Stress Type</u>	<u>Stress, psi</u>	<u>Stress, kg/m²</u>	<u>Percent Allowable Stress</u>
A-disc bore	tangential	137,644	96,777,000	98.4
B-disc lug	tensile	40,600	28,546,000	31.2
C-blade root	tensile	36,000	25,312,000	32.8
D-firtree attachment	tensile	19,850	13,957,000	18.0
E-tooth bending	tensile	17,350	12,198,000	18.8
F-tooth	shear	19,800	13,921,000	30.6
G-tooth	bearing	57,600	40,499,000	28.6

Total radial centrifugal growth at blade tip = 0.0268 inch (0.000681 m)



E. Critical Speeds

A critical speed analysis was performed for the two-bearing system shown by Figure 3i. The critical speed for a 6000 lb (2722 kg) thrust is 14,738 rpm, or 32.5 percent critical speed margin at design speed.

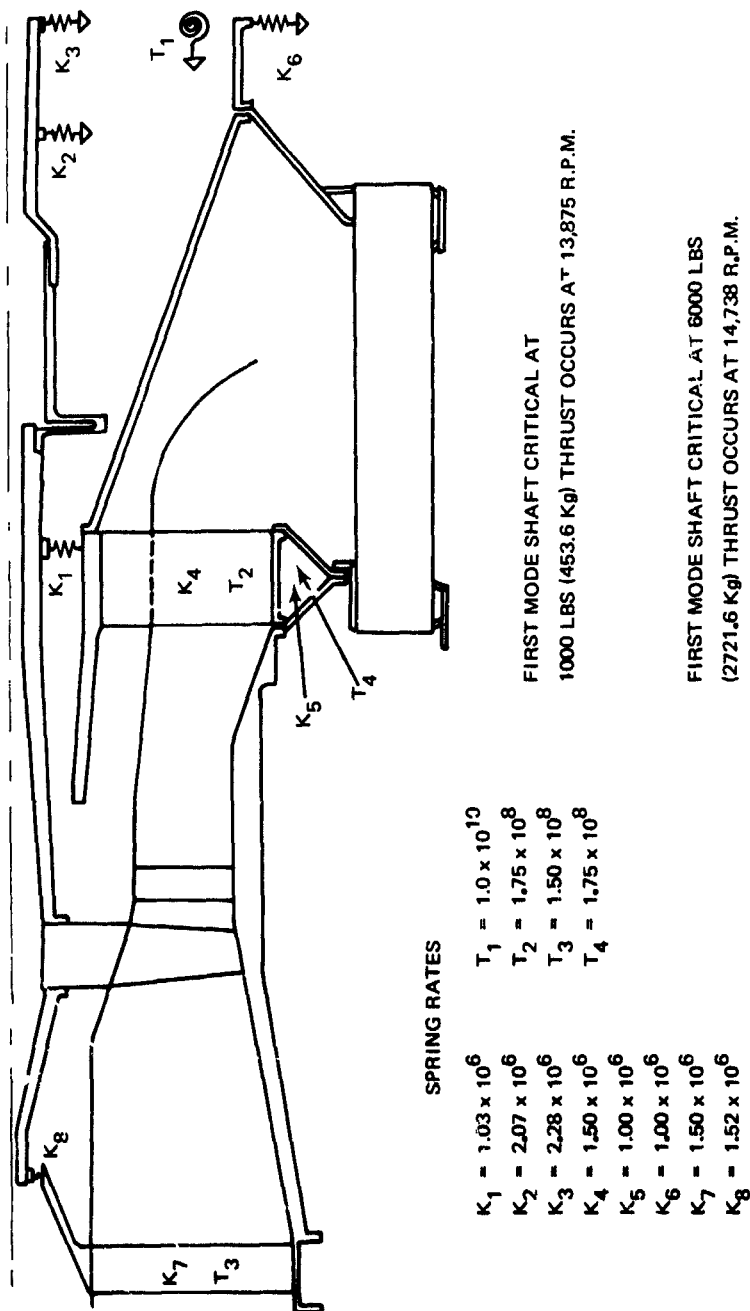


Figure 31 Compressor Rig Spring Location and Spring Rates

APPENDIX 1

Flow Field Calculation Procedure

APPENDIX 1

Flow Field Calculation Procedures

The aerodynamic flow field calculation used in this design assumes axisymmetric flow and uses solutions of continuity, energy, and radial equilibrium equations. These equations account for streamline curvature and radial gradients of enthalpy and entropy, but viscous terms are neglected. Calculations were performed on stations oriented at an angle λ with respect to the axial direction.

The equation of motion is in the form of:

$$\frac{1}{2} \frac{\partial V^2}{\partial m} \cos(\lambda - \epsilon) + \frac{V^2}{R_c} \sin(\lambda - \epsilon) - \frac{V_\theta^2}{r} + \frac{1}{\rho} \frac{\partial p}{\partial r} = 0$$

$$R_c = \frac{\partial \epsilon}{\partial m} = \text{streamline radius of curvature}$$

Enthalpy rise across a rotor for a streamline ψ is given by the Euler relationship

$$\Delta H_{\text{Rotor}} = (U_2 V_{\theta 2})_\psi - (U_1 V_{\theta 1})_\psi$$

Weight flow is calculated by the continuity equation

$$W = 2\pi \int_{y \text{ root}}^{y \text{ tip}} K \rho V_m \frac{\sin(\lambda - \epsilon)}{\sin \lambda} y \, dy$$

where K is the local blockage factor and y is the length along the calculation station from the centerline to the point of interest.

APPENDIX 2

Loss System

APPENDIX 2

Loss System

The loss model that was developed is an extension of the NASA model which combines a shock loss with a profile loss to obtain total loss⁸. To obtain shock loss a normal shock is assumed to originate at the leading edge and to be normal to a mean camber line at mid-gap as shown by Figure 32. To obtain the Mach number of the assumed normal shock, a Prandtl-Meyer expansion from the free-stream relative Mach number is calculated from the turning of the flow from the inlet to the suction-surface shock intersection point. The camber of the suction surface between the leading edge and the shock intersection point is termed the supersonic suction-surface camber ($\phi_{ss_{SS}}$). Thus, the flow turns from the free-stream condition through an incidence angle i_{SS} to the suction-surface leading edge and is further turned through the angle $\phi_{ss_{SS}}$ to the shock interaction point. Three-dimensional effects were considered small and were ignored.

For a Prandtl-Meyer expansion, Mach number and turning are related by:

$$\mu = f(M) = \sqrt{\frac{k+1}{k-1}} \tan^{-1} \sqrt{\frac{k-1}{k+1} (M^2 - 1)} - \tan^{-1} \sqrt{M^2 - 1}$$

Then

$$\mu_1 = f(M'_1)$$

$$\mu_s = \mu_1 + \phi_{ss_{SS}} + i_{SS}$$

$$M'_s = f^{-1}(\mu_s)$$

$$M'_{s \text{ avg.}} = \frac{M'_s + M'_1}{2}$$

Using the general loss model where total loss is equal to the sum of shock loss and profile loss, several compressors were analyzed. Aerodynamic conditions were calculated along the leading and trailing edges of both rotors and stators with a data reduction program that uses test data in the form of pressures and temperatures as input. This program provides a three-dimensional axisymmetric compressible flow solution of the continuity, energy, and radial equilibrium equations. It is discussed in Appendix 1. Spanwise values for profile loss (ω_p) were obtained by subtracting shock loss from the total loss. A profile loss parameter ($\bar{\omega}_p \cos \beta'_2 / 2\sigma$) was calculated and correlated against diffusion factor. Table 5 lists the compressors that were analyzed to obtain this correlation of profile loss.

Compressors 1 through 5 were used for the rotor profile loss correlation shown in Figure 33. Compressor 4 was used for the stator profile loss. This compressor was a NASA-sponsored high-Mach-number stator research rig in which three different stators were evaluated. The stator profile loss correlation is shown in Figure 34.

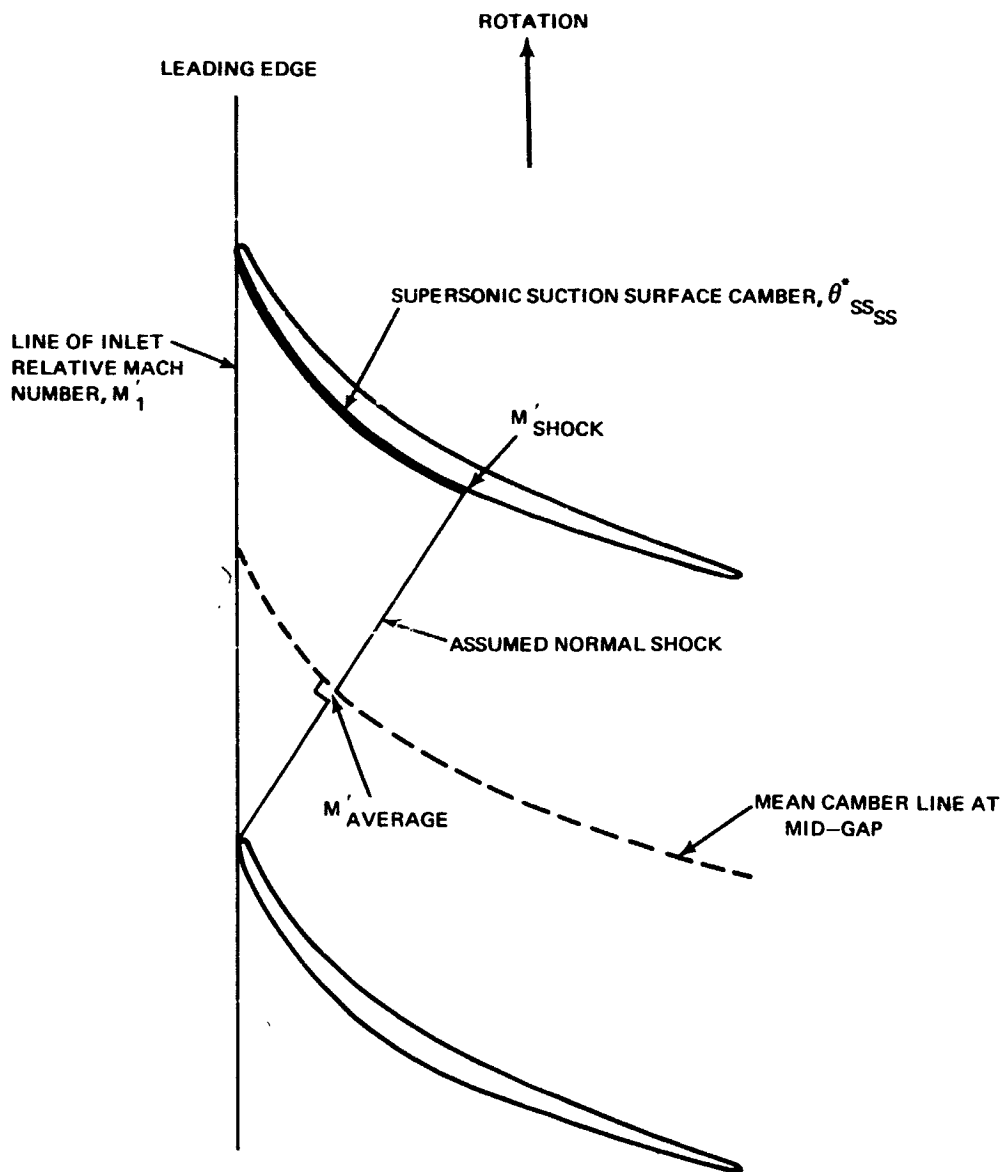


Figure 32 Location of Assumed Normal Shock for Loss Model

TABLE 5

Compressors Analyzed for Profile Loss Correlation

<u>No.</u>	<u>Compressor</u>	<u>Design</u>	<u>Rotor Series</u>	<u>Stator Series</u>	<u>Match Pres. Ratio</u>	<u>Tip Speeds Analyzed</u>	
						<u>ft/sec</u>	<u>(m/sec)</u>
1	JTF14F	single-stage fan	straight entry	not analyzed	-	1790	1630
						(545.6)	(496.3)
2	JTF17	two-stage fan	straight entry	not analyzed	-	1465	1300
						(446.5)	(396.2)
3	JTF9D	single-stage fan	straight entry	not analyzed	-	1550	1395
						(472.2)	(425.1)
4	Contract NAS3-7614	single-stage fan	C.A.	C.A. & M.C.A.	1.5	1570	1430
						(478.5)	(435.9)
5	Contract NAS3-7617	single-stage fan	C.A. & M.C.A.	not analyzed	1.6	1287	
						(392.3)	
4	Contract NAS3-7614	single-stage fan	C.A.	C.A. & M.C.A.	1.5	1315	1197
						(410.8)	(364.8)
5	Contract NAS3-7617	single-stage fan	C.A. & M.C.A.	not analyzed	1.6	1075	955
						(327.7)	(291.1)
5	Contract NAS3-7617	single-stage fan	C.A. & M.C.A.	not analyzed	1.6	1400	1260
						(426.7)	(384.0)

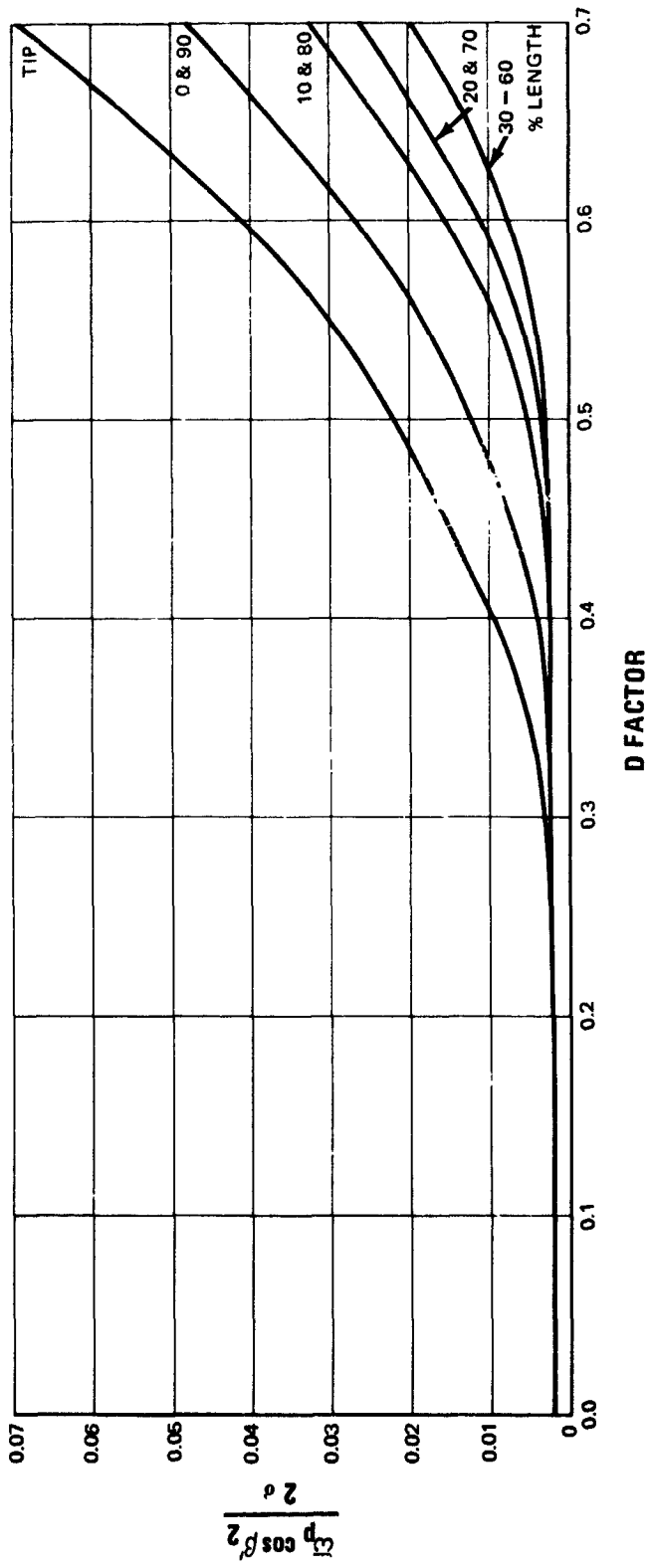


Figure 33 Rotor Profile Loss Parameter vs D Factor

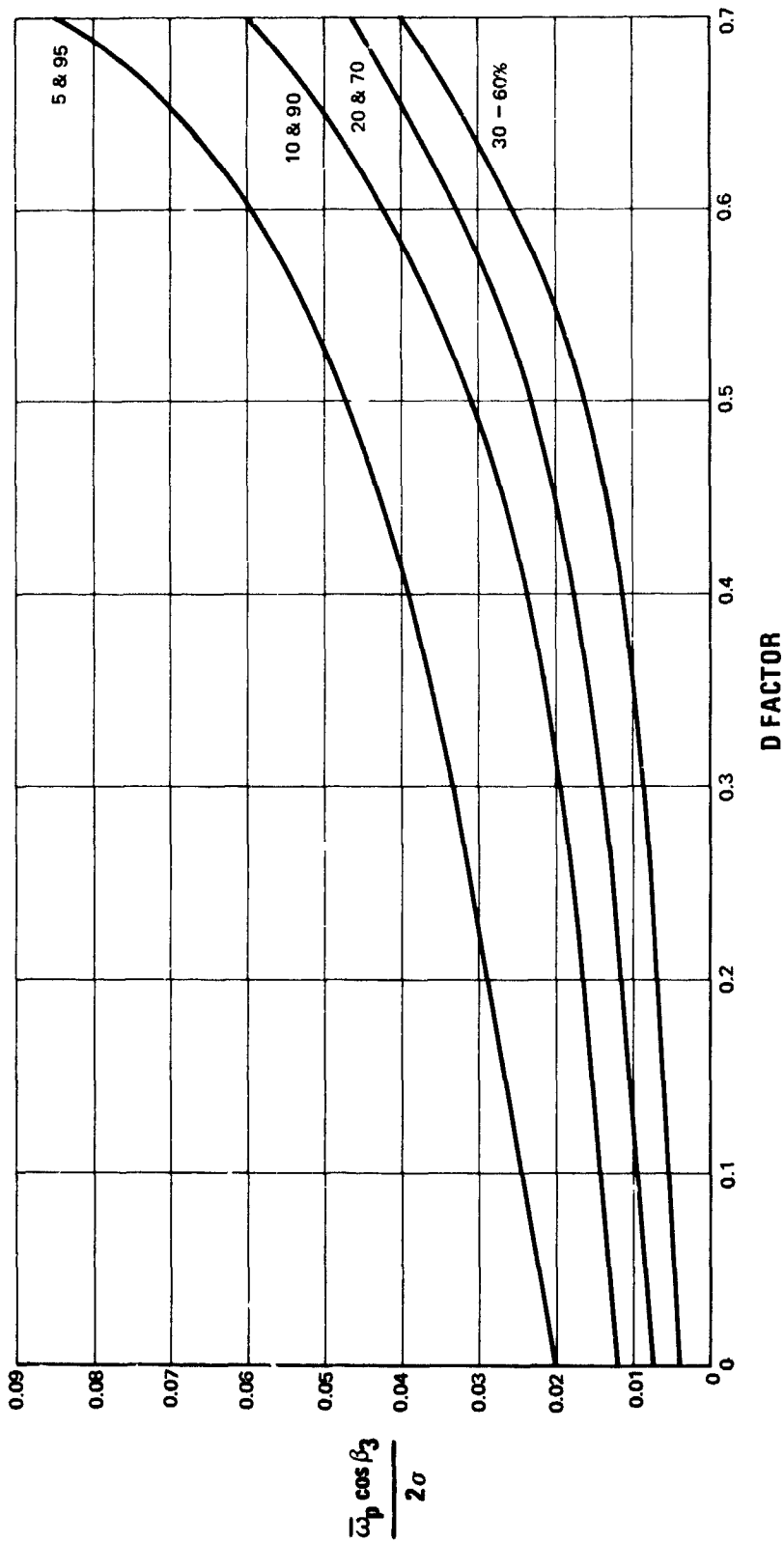


Figure 34 Stator Profile Loss Parameter vs D Factor

APPENDIX 3
Incidence Selection

APPENDIX 3

Incidence Selection

For blade elements with supersonic inlet relative Mach numbers, the absolute flow capacity is established by incidence and entrance-region curvature. The entrance region is defined as the portion of the blade suction surface forward of the first captured Mach wave, as shown on Figure 38. Consequently the selection of incidence is of major concern. However, this condition is relaxed for subsonic blade elements and additional latitude is available in selecting incidence.

Subsonic Flow

The philosophy used in this design was to set the subsonic incidence at approximately zero degrees with respect to the leading-edge suction surface, except near the blade ends.

For the rotor only the very root is subsonic. Data from Contract NAS3-7617 that was reviewed, indicated that a leading-edge suction-surface incidence of approximately -2.0 degrees gives minimum blade-element loss for the root. This incidence was faired into the incidence set for the supersonic portions discussed below.

The entire stator operates subsonically at design. This stator is very similar to those used in Reference 5. Figure 35 shows typical mid-span stator loss data indicating that an incidence of zero degrees to the suction surface is appropriate. Figures 36 and 37 show stator data for roots and tips respectively. This data indicates that both the root and tip suction-surface incidence for minimum loss should be positive. Figure 22 shows the selected spanwise variation of incidence for the stator.

Supersonic Flow

Efficient alignment of supersonic flow to the suction surface in the entrance region of rotor tip airfoils was a major design consideration. If the blade suction surface curvature upstream of the first captured Mach wave does not correspond exactly to free-stream flow, then alignment with the surface causes expansion or compression waves shown in Figure 38. When meridional flow is subsonic, the waves formed between the leading edge and the first captured Mach wave propagate forward, and adjust upstream flow conditions. Compression or expansion from this portion of the suction surface must be balanced by a corresponding expansion or compression of equal strength respectively, since each blade must have the same inlet flow conditions. Far upstream of the leading edge, compression and expansion waves cancel each other, and the flow is axisymmetric. Thus, a shock at the leading edge (Figure 38a) must be followed by an expansion to a neutral point B', where aligned flow angle equals the axisymmetric flow angle, followed by continued expansion to point B sufficient to cancel the entire leading-edge compression. Conversely an expansion about the leading-edge (Figure 38b) must be followed by a sys-

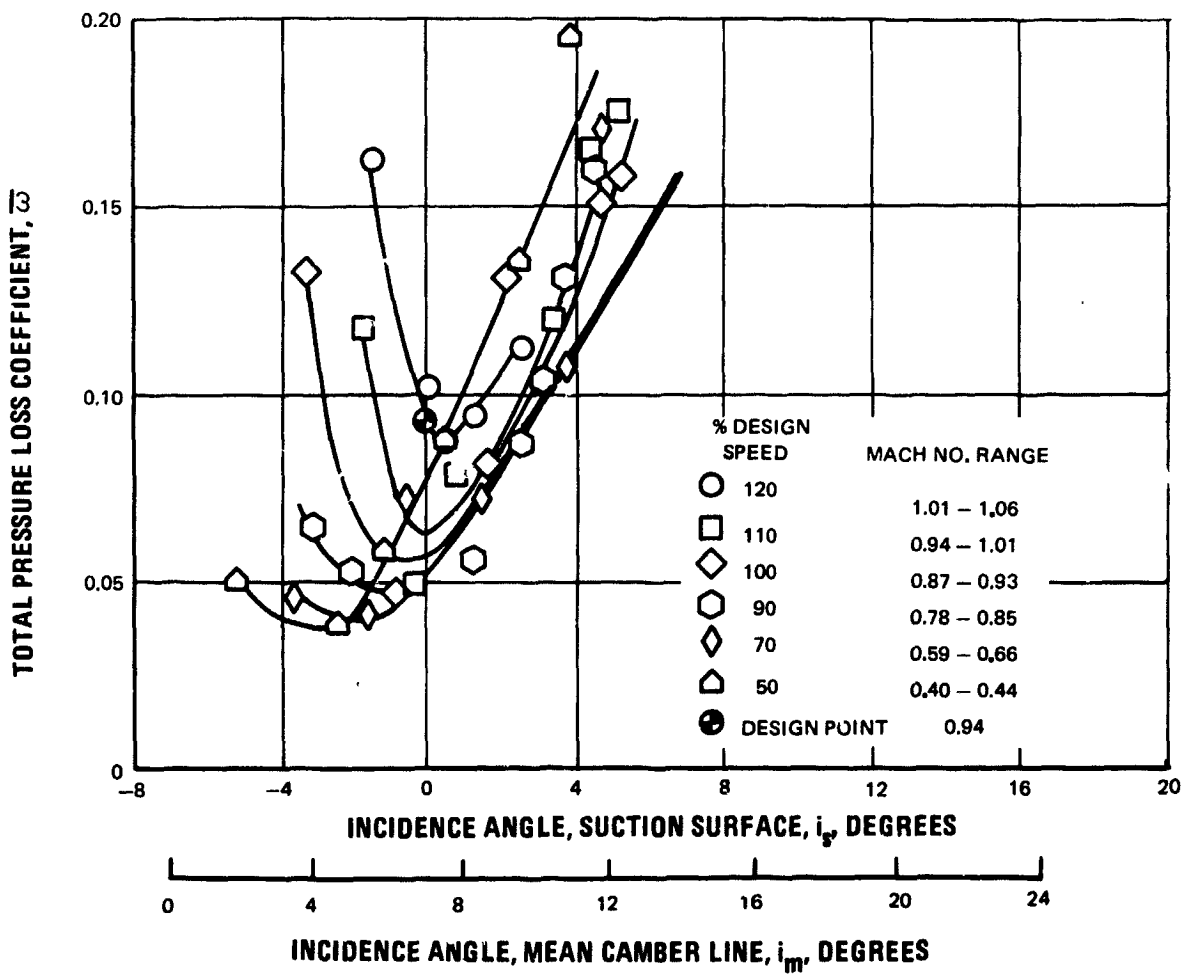


Figure 35 Multiple-Circular-Arc Stator B Loss Data for 50 Percent Span from Contract NAS3-7614

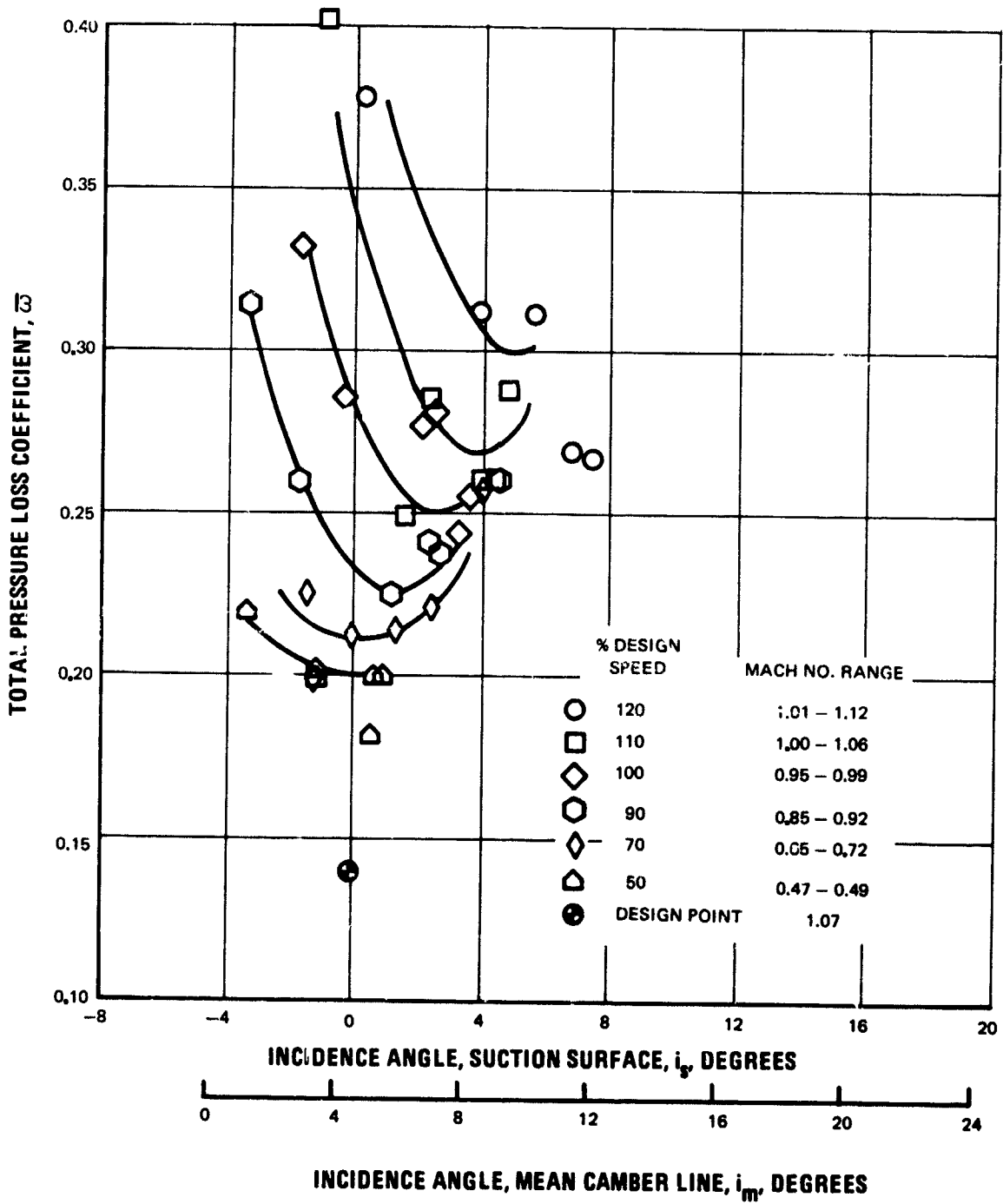


Figure 36 Multiple-Circular-Arc Stator B Loss Data for 5 Percent Span from Root, Contract NAS3-7614

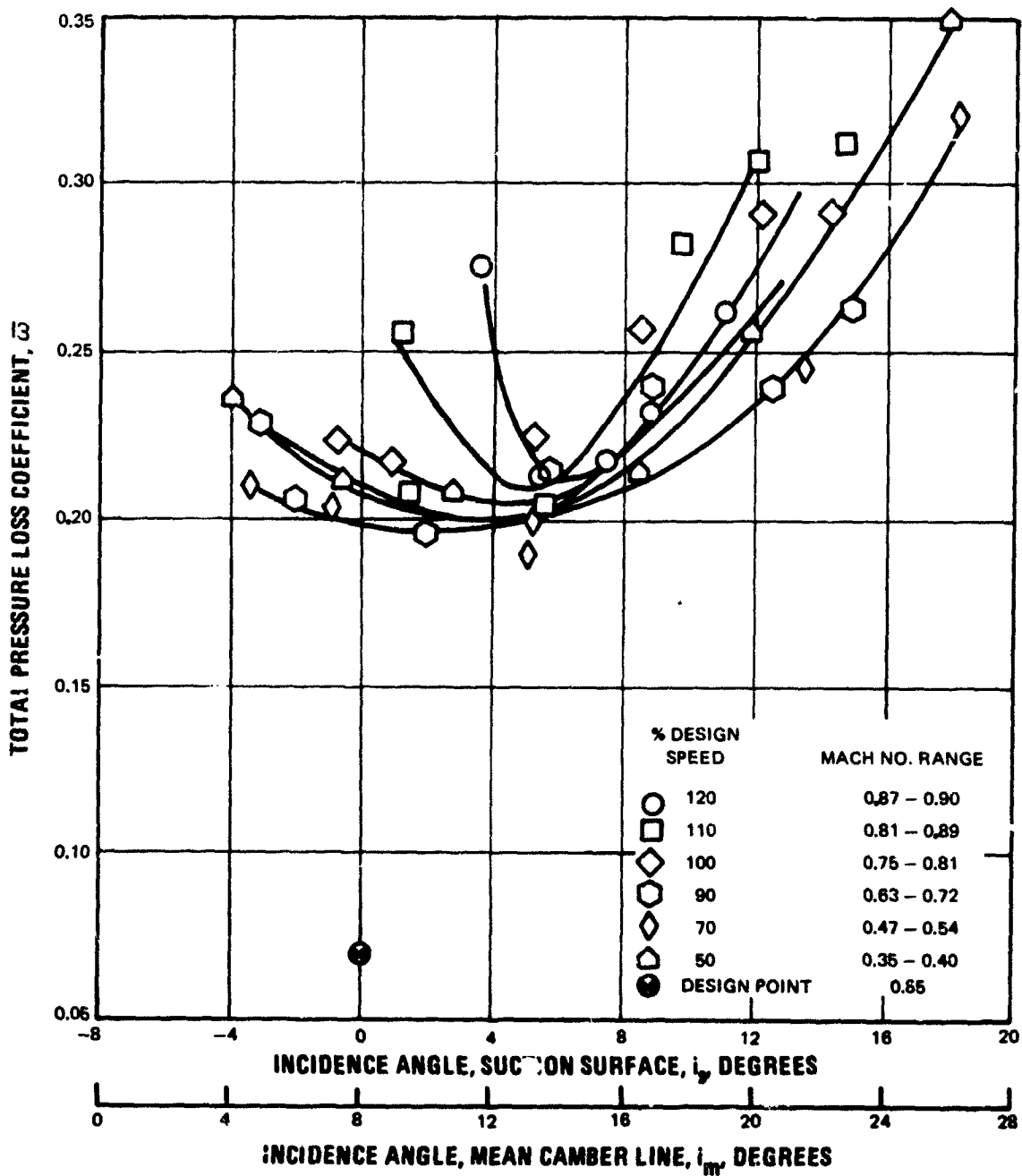


Figure 37 Multiple-Circular-Arc Stator B Loss Data for 95 Percent Span from Root, Contract NAS3-7614

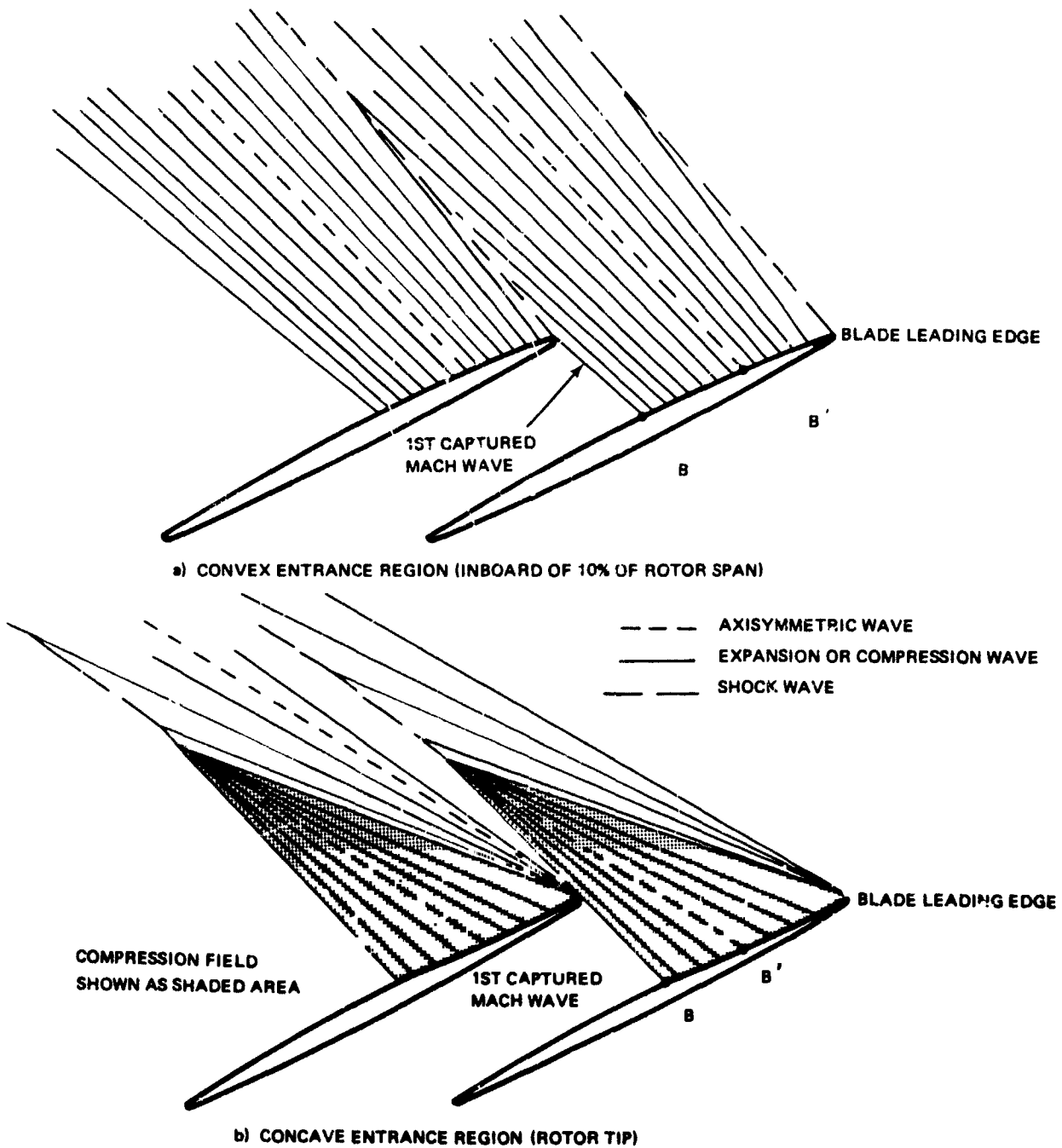


Figure 38 Wave Pattern for Super-Critical Operation of Curved-Blade Entrance Regions

tem of cancelling compression waves. Thus, a repeating pattern of waves with a period of one blade gap exists at any radial location, and only one Mach wave in the expansion or compression fields on the leading edge has the axisymmetric flow angle.

If entrance-region design of supersonic sections does not accommodate this adjustment, then it must take place through detached shocks or blade boundary-layer buildup, or combination of both. This sort of inefficient adjustment can be a source of significant loss in supersonic blade elements.

It was assumed that the neutral point on the blade-suction surface, where aligned flow angle equalled the axisymmetric flow angle, was halfway between the leading edge and the emanation point of the first captured Mach wave, as shown in Figure 38. A detailed construction of a typical flow pattern verified that this assumption is a good approximation.

Entrance-region relative flow angles for free-stream flow were calculated by the flow-field calculation procedure discussed in Appendix 1. These angles were decreased approximately 1.5 degrees to account for increased axial velocity due to blade leading-edge blockage, and for boundary-layer development on the suction surface. Then the blade-element suction surface was set tangent to this adjusted free-stream flow angle at point B' in Figure 38, which is midway between the leading edge and the emanation point of the first captured Mach wave, point B. Thus for supersonic flow, the airfoil suction surface was aligned with the axisymmetric flow angle at point B', with cancelling zones of expansion and compression on either side of this point. The resultant design incidence angles are shown on Figure 12.

APPENDIX 4

Stream-Tube Analysis in Channels Between Blades

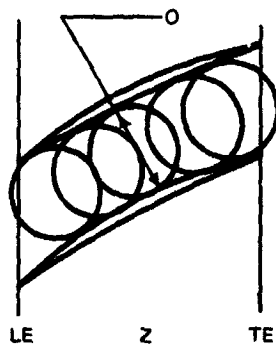
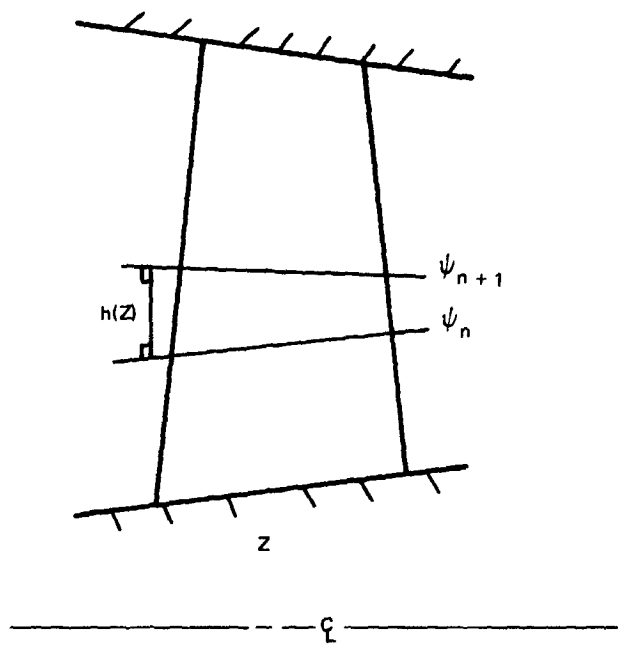
APPENDIX 4

Stream-Tube Analysis in Channels Between Blades

Supersonic blade element data in References 1 through 4, show minimum loss occurring when blade passage a/a^* was approximately 1.05. Subsonic stator blade-element data from References 5 and 4, and subsonic two-dimensional cascade data show minimum loss occurring when channel throat area was approximately $1.03 s \cos \beta$. Thus channel area was considered of equal importance to incidence angle in designing for operation at minimum loss.

A stream-tube analysis was performed to obtain the local value of a/a^* through the blade passage. The calculation used an average passage width obtained by averaging passage widths of blade channels for streamlines defining the stream-tube annulus, shown by Figure 39. The calculation accounts for convergence, total relative enthalpy change in rotors due to radius changes, and distribution of losses within the channel. The distribution of losses within the channel assumed no loss until the first covered section, see Figure 40. At this point the shock loss described in Appendix 2 was applied. The profile loss was linearly applied from the first covered section to the full value at the trailing edge. Thus, at the first covered section the full shock loss was used and at the trailing edge the sum of the shock and profile loss, as shown by Figure 40.

Values of minimum channel a/a^* were controlled by adjusting front camber. If a larger value of a/a^* was required the passage was opened by increasing the value of front camber while holding rotor incidence constant at the B' point, and stator incidence constant at the leading edge, as discussed in Appendix 3. Conversely, if the value of a/a^* was too large, front camber was reduced. In general, care was taken to design the blade so that minimum a/a^* occurs near the blade entrance region, to obtain gradual diffusion through the channel.



$$\text{STREAM TUBE AREA} = \frac{O(z)\psi_{n+1} + O(z)\psi_n}{2} \times h(z)$$

Figure 39 Channel Area

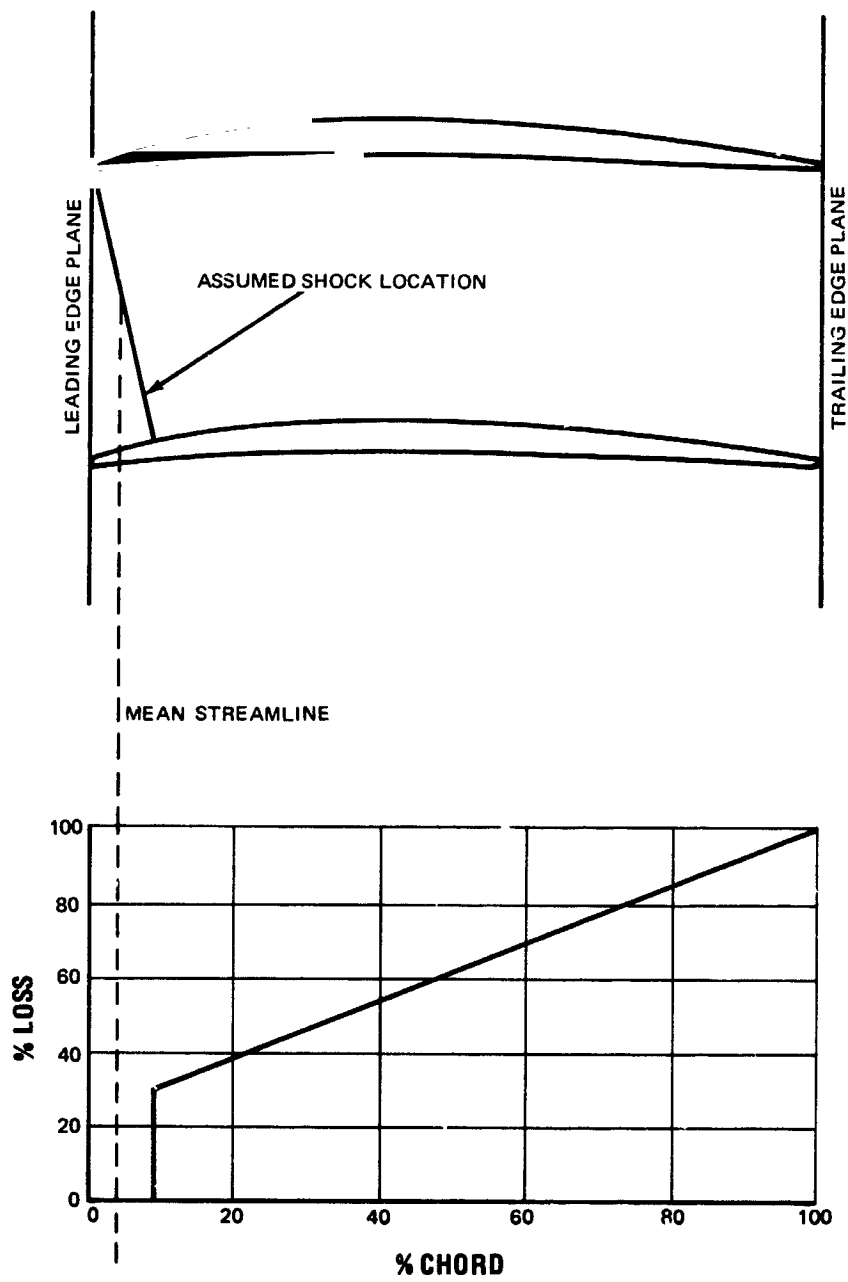


Figure 40 Loss Distribution through Channel

APPENDIX 5
Deviation System

APPENDIX 5

Deviation System

Carter's rule plus an experience factor was used to obtain deviation for both the rotor and stator. The form of Carter's rule that was used is given below:

$$\text{Carter's rule deviation} = \frac{(\Delta\beta - i)m_c \sqrt{\frac{1}{\sigma}}}{1 - m_c \sqrt{\frac{1}{\sigma}}}$$

$$m_c = 0.92 (a/c)^2 + 0.002 \beta'_2$$

$$\frac{a}{c} = \frac{\text{distance to maximum camber point from leading edge}}{\text{chord}}$$

For the rotor the modification to Carter's rule that was used is shown by Figure 41. Data from References 1, 2, 3, and 4 is shown in this figure.

For the stator the modification to Carter's rule that was used is shown by Figure 42. This curve is based on data from Reference 5 which evaluated three stators with Mach numbers and loadings slightly higher than those of the present design.

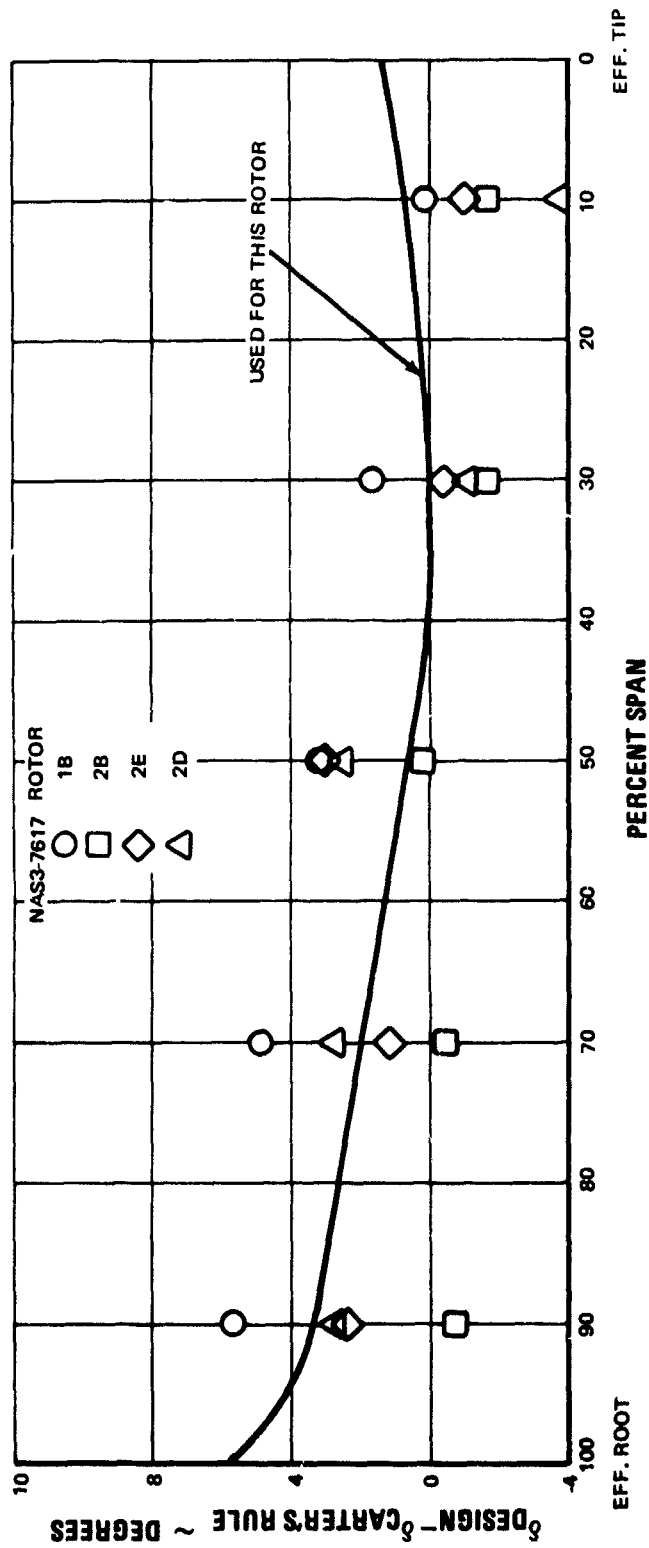


Figure 41 Modification to Carter's Rule for Rotor

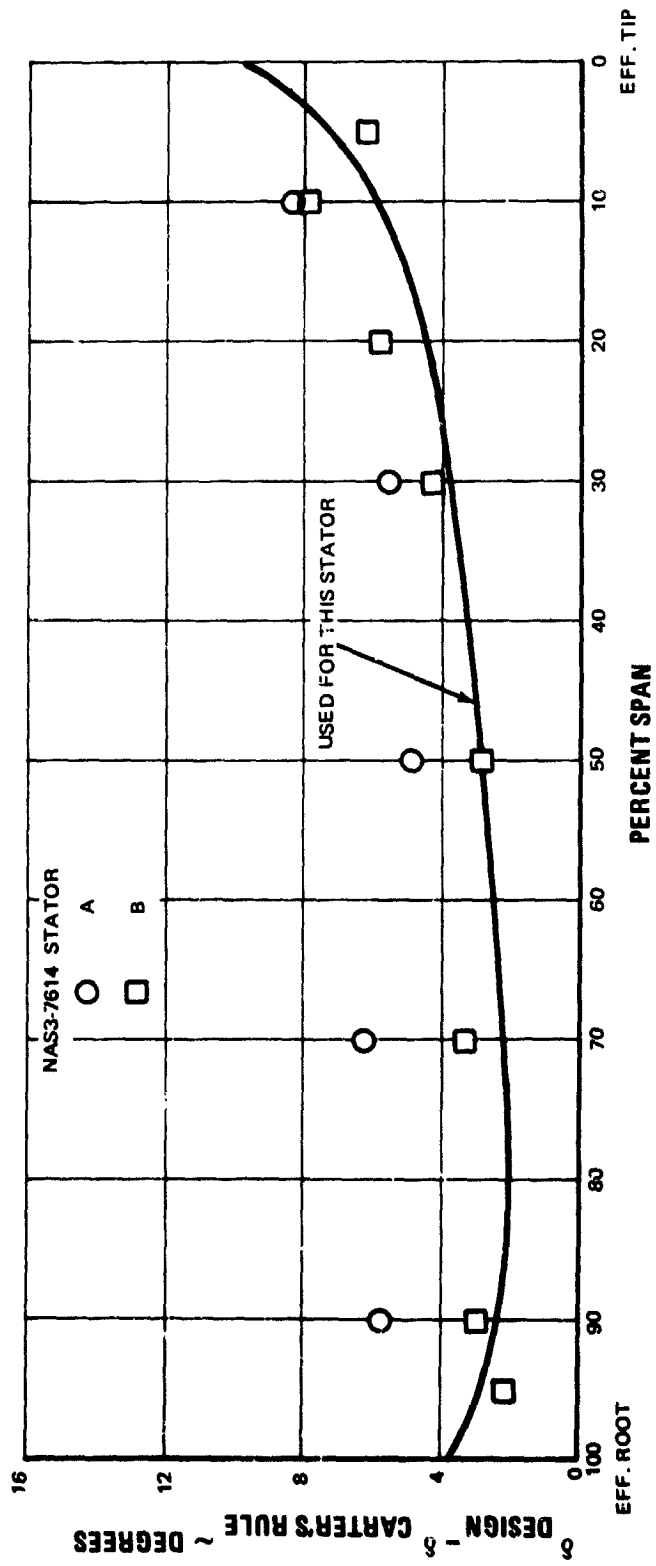


Figure 42 Modification to Carter's Rule for Stator

APPENDIX 6
Aerodynamic Summary

TABLE 6
Aerodynamic Summary - Rotor Inlet

		0	10	20	30	40	50	60	70	80	90	100
		effective I.D.									effective	O.D.
Diameter	inches	16.541	19.086	21.210	23.068	24.743	26.286	27.732	29.105	30.424	31.706	32.959
Diameter	meters	0.4201	0.4848	0.5387	0.5859	0.6285	0.6677	0.7044	0.7393	0.7728	0.8053	0.8316
Pressure Ratio	--	1.0	1.0	1.0	1.0	1.0	1.0	1.0	1.0	1.0	1.0	1.0
Temperature Ratio	--	1.0	1.0	1.0	1.0	1.0	1.0	1.0	1.0	1.0	1.0	1.0
M	--	0.560	0.585	0.609	0.629	0.644	0.653	0.656	0.654	0.646	0.632	0.621
M'	--	0.928	1.037	1.132	1.216	1.290	1.356	1.416	1.470	1.519	1.563	1.609
V	ft/sec	606.7	632.6	656.7	676.5	691.1	700.2	703.5	701.1	692.7	678.7	668.4
V	m/sec	184.9	192.8	200.2	206.2	210.6	213.4	214.4	213.7	211.1	206.9	203.7
V'	ft/sec	1005.5	1120.7	1219.9	1306.8	1384.2	1453.8	1517.2	1575.3	1629.3	1680.0	1731.8
V'	m/sec	306.5	341.6	371.8	398.3	421.9	443.1	462.4	480.2	496.6	512.1	527.8
V _z	ft/sec	575.6	617.1	651.5	675.1	691.1	698.9	698.7	680.7	675.0	652.3	638.6
V _z	m/sec	175.5	188.1	198.3	205.8	210.6	213.0	213.0	210.5	205.7	198.8	194.7
V _m	ft/sec	606.7	632.6	656.7	676.5	691.1	700.2	703.5	701.1	692.7	678.7	668.4
V _m	m/sec	184.9	192.8	200.2	206.2	210.6	213.4	214.4	213.7	211.1	206.9	203.7
V _θ	ft/sec	0	0	0	0	0	0	0	0	0	0	0
V _θ	m/sec	0	0	0	0	0	0	0	0	0	0	0
V' _θ	ft/sec	-801.8	-925.1	-1028.1	-1118.1	-1199.3	-1274.1	-1344.2	-1410.7	-1474.7	-1536.8	-1597.6
V' _θ	m/sec	-224.4	-282.0	-313.4	-340.8	-356.6	-388.4	-409.7	-429.9	-449.5	-468.4	-486.9
β _z	degrees	0	0	0	0	0	0	0	0	0	0	0
β _z	radians	0	0	0	0	0	0	0	0	0	0	0
β' _z	degrees	54.32	56.29	57.68	58.88	60.05	61.25	62.54	63.91	65.41	67.00	68.21
β' _z	radians	0.948	0.982	1.007	1.028	1.048	1.069	1.092	1.115	1.142	1.169	1.191
ε	degrees	18.42	12.70	7.83	3.65	-0.08	-3.51	-6.75	-9.88	-13.00	-16.05	-17.15
ε	radians	0.322	0.222	0.137	0.064	-0.001	-0.061	-0.118	-0.172	-0.227	-0.280	-0.299
U	ft/sec	801.8	925.1	1028.1	1118.1	1199.3	1274.1	1344.2	1410.7	1474.7	1536.8	1597.6
U	m/sec	244.4	282.0	313.4	340.8	365.6	388.4	409.7	430.0	449.5	468.4	486.9
M _m	--	0.560	0.586	0.610	0.629	0.644	0.653	0.657	0.654	0.646	0.632	0.621
M _m	--	0.531	0.571	0.604	0.628	0.644	0.652	0.652	0.644	0.629	0.607	0.594
β _m	degrees	0	0	0	0	0	0	0	0	0	0	0
β _m	radians	0	0	0	0	0	0	0	0	0	0	0
β' _m	degrees	52.88	55.64	57.43	58.83	60.05	61.21	62.37	63.57	64.84	66.17	67.30
β' _m	radians	0.923	0.971	1.002	1.027	1.048	1.068	1.089	1.110	1.132	1.155	1.175

Note: See Figure 1 for flowpath

TABLE 7
Aerodynamic Summary - Rotor Exit

		0	10	20	30	40	50	60	70	80	90	100
		effective I.D.										
		effective O.D.										
Diameter	inches	19.193	20.815	22.217	23.530	24.782	25.987	27.158	28.302	29.427	30.553	31.847
Diameter	meters	0.4875	0.5287	0.5643	0.5977	0.6295	0.6601	0.6898	0.7189	0.7474	0.7760	0.8089
Pressure Ratio	--	2.0	2.0	2.0	2.0	2.0	2.0	2.0	2.0	2.0	2.0	2.0
Temperature Ratio	--	1.250	1.230	1.229	1.232	1.235	1.239	1.244	1.251	1.259	1.277	1.350
M	--	0.854	0.801	0.764	0.735	0.712	0.694	0.680	0.670	0.662	0.657	0.651
M'	--	0.469	0.579	0.620	0.659	0.700	0.741	0.781	0.819	0.854	0.866	0.742
V	ft/sec	995.7	933.6	895.1	865.0	841.2	822.9	809.7	800.7	795.4	795.4	811.1
V	m/sec	303.5	284.6	272.8	263.7	256.4	250.8	246.8	244.0	242.4	242.4	247.2
V'	ft/sec	546.3	674.6	726.1	775.8	827.7	879.8	929.8	979.1	1025.4	1048.2	924.3
V'	m/sec	166.5	205.6	221.3	236.5	252.3	268.2	283.4	298.4	312.6	319.5	281.7
V _z	ft/sec	512.3	590.8	592.0	586.0	579.0	571.9	563.9	556.5	548.0	524.5	379.4
V _z	m/sec	156.1	180.1	180.4	178.6	176.5	174.3	171.9	169.6	167.0	159.9	115.6
V _m	ft/sec	538.4	605.2	598.4	588.0	579.2	572.2	566.1	562.0	558.4	540.9	395.4
V _m	m/sec	164.1	184.5	182.4	179.2	176.5	174.4	172.6	171.3	170.2	164.9	120.5
V _θ	ft/sec	837.6	710.9	665.6	634.4	610.0	591.5	578.9	570.2	566.4	583.1	708.2
V _θ	m/sec	255.3	216.7	202.9	193.4	185.9	180.3	176.5	173.8	172.6	177.7	215.9
V' _θ	ft/sec	-92.8	-298.1	-411.3	-506.1	-591.3	-688.2	-737.5	-801.7	-860.0	-897.9	-825.4
V' _θ	m/sec	-28.3	-90.9	-125.4	-154.3	-180.2	-203.7	-224.8	-244.4	-262.1	-273.7	-254.6
β _z	degrees	58.55	50.27	48.35	47.27	46.49	45.96	45.75	45.70	45.95	48.03	61.82
β _z	radians	1.022	0.877	0.844	0.825	0.811	0.802	0.799	0.798	0.802	0.838	1.079
β' _z	degrees	10.26	26.77	34.79	40.82	45.60	49.44	52.60	55.24	57.50	59.71	65.58
β' _z	radians	0.179	0.467	0.607	0.712	0.796	0.863	0.918	0.964	1.004	1.042	1.145
ε	degrees	17.93	12.55	8.38	4.69	1.28	-1.95	-5.04	-8.07	-11.71	-14.18	-16.35
ε	radians	0.313	0.219	0.146	0.082	0.022	-0.034	-0.088	-0.141	-0.194	-0.248	-0.285
U	ft/sec	930.3	1008.9	1076.9	1140.6	1201.3	1259.7	1316.4	1371.9	1426.4	1481.0	1543.7
U	m/sec	283.6	307.5	328.2	347.6	366.1	384.0	401.3	418.2	434.8	451.4	470.5
M _m	--	0.462	0.519	0.511	0.500	0.490	0.482	0.475	0.470	0.465	0.447	0.318
M _z	--	0.439	0.507	0.505	0.498	0.490	0.482	0.473	0.465	0.456	0.433	0.305
β _m	degrees	57.27	49.59	48.05	47.18	46.48	45.95	45.64	45.42	45.41	47.15	60.83
β _m	radians	0.999	0.866	0.839	0.823	0.811	0.802	0.797	0.793	0.793	0.823	1.062
β' _m	degrees	9.77	26.22	34.50	40.72	45.59	49.43	52.49	54.97	57.0	58.93	64.67
β' _m	radians	0.171	0.458	0.602	0.711	0.796	0.863	0.916	0.959	0.995	1.029	1.129

TABLE 8
Aerodynamic Summary - Stator Inlet

	0	10	20	30	40	50	60	70	80	90	100
	effective I.D.										
Diameter	19.934	21.376	22.637	23.808	24.911	25.960	26.965	27.934	28.870	29.787	30.766
Diameter	0.5063	0.5430	0.5750	0.6047	0.6327	0.6594	0.6849	0.7095	0.7333	0.7566	0.7815
Pressure Ratio	2.0	2.0	2.0	2.0	2.0	2.0	2.0	2.0	2.0	2.0	2.0
Temperature Ratio	1.250	1.230	1.230	1.232	1.235	1.239	1.244	1.251	1.259	1.276	1.350
M	0.888	0.850	0.823	0.804	0.789	0.778	0.771	0.768	0.767	0.769	0.769
M'	0.570	0.673	0.713	0.749	0.785	0.821	0.853	0.884	0.912	0.918	0.785
V	1030.3	983.3	956.5	937.1	922.9	913.3	907.9	906.3	908.6	917.2	943.7
V	314.1	299.7	291.5	285.6	281.3	278.4	276.7	276.2	276.9	279.6	287.7
V'	660.9	778.5	827.8	873.3	918.8	963.0	1004.2	1044.0	1080.7	1094.8	963.3
V'	201.4	237.3	252.3	266.2	280.1	293.5	306.1	318.2	329.4	333.7	293.6
V _z	616.3	684.6	691.4	693.0	694.1	695.2	696.0	697.7	700.1	692.6	588.7
V _z	187.9	208.7	210.7	211.2	211.6	211.9	212.1	212.7	213.4	211.1	179.4
V _m	641.3	698.4	698.7	696.4	695.3	695.4	696.0	698.2	701.6	695.3	594.3
V _m	195.5	212.9	213.0	212.3	211.9	212.0	212.1	212.8	213.8	211.9	181.1
V _θ	806.5	692.2	653.3	627.0	606.9	592.1	583.1	577.8	577.4	598.1	733.1
V _θ	245.8	211.0	199.1	191.1	185.0	180.5	177.7	176.1	176.0	182.3	223.5
V' _θ	-159.8	-344.0	-443.9	-526.9	-600.6	-666.2	-724.0	-776.2	-822.0	-845.7	-758.2
V' _θ	-48.7	-104.8	-135.3	-160.6	-183.1	-203.1	-220.7	-236.6	-250.6	-257.8	-231.1
β _z	52.61	45.32	43.38	42.14	41.16	40.42	39.96	39.63	39.51	40.82	51.24
β _z	0.918	0.791	0.757	0.736	0.718	0.706	0.697	0.692	0.690	0.712	0.894
β' _z	14.53	26.68	32.71	37.25	40.87	43.78	46.13	48.05	49.58	50.69	52.17
β' _z	0.254	0.466	0.571	0.650	0.713	0.764	0.805	0.839	0.865	0.885	0.911
ε	16.03	11.42	8.29	5.66	3.36	1.33	-0.49	-2.14	-3.63	-5.07	-7.90
ε	0.280	0.199	0.145	0.099	0.059	0.023	-0.009	-0.037	-0.063	-0.089	-0.138
U	966.3	1036.1	1097.2	1154.0	1207.5	1258.3	1307.0	1354.0	1399.4	1443.8	1491.3
U	294.5	315.8	334.4	351.7	368.1	383.5	398.4	412.7	426.5	440.1	454.6
M _m	0.553	0.604	0.601	0.597	0.594	0.593	0.591	0.591	0.591	0.583	0.485
M _z	0.531	0.592	0.595	0.594	0.593	0.593	0.591	0.591	0.591	0.581	0.480
β _m	51.51	44.74	43.08	42.00	41.11	40.41	39.96	39.61	39.45	40.70	50.97
β _m	0.899	0.781	0.752	0.733	0.718	0.705	0.697	0.691	0.689	0.710	0.890
β' _m	13.99	26.22	32.43	37.11	40.82	43.77	46.13	48.03	49.52	50.57	51.91
β' _m	0.244	0.458	0.566	0.648	0.712	0.764	0.805	0.838	0.864	0.883	0.906

TABLE 9
Aerodynamic Summary - Stator Exit

	0	10	20	30	40	50	60	70	80	90	100
	effective I.D.										
Diameter	21.072	22.267	23.323	24.322	25.285	26.217	27.126	28.013	28.885	29.747	30.628
Diameter	0.5352	0.5656	0.5924	0.6178	0.6422	0.6659	0.6890	0.7115	0.7337	0.7556	0.7780
Pressure Ratio	0.894	0.960	0.974	0.980	0.980	0.979	0.977	0.974	0.969	0.961	0.941
Temperature Ratio	1.0	1.0	1.0	1.0	1.0	1.0	1.0	1.0	1.0	1.0	1.0
M	0.504	0.583	0.588	0.587	0.581	0.576	0.571	0.566	0.559	0.548	0.520
M'	0.979	1.074	1.113	1.146	1.175	1.203	1.231	1.257	1.281	1.299	1.285
V	613.6	698.5	704.0	703.1	697.3	693.1	688.5	684.8	678.8	671.1	656.5
V	187.0	212.9	214.6	214.3	212.5	211.3	209.9	208.7	206.9	204.6	200.1
V'	1191.5	1285.6	1331.8	1372.7	1410.1	1447.5	1484.2	1520.7	1556.0	1590.4	1623.3
V'	186.3	212.2	214.1	214.0	212.3	211.1	209.8	208.7	206.9	204.6	200.1
V _z	611.1	696.3	702.5	702.1	696.7	692.7	688.3	684.6	678.7	671.0	656.4
V _z	186.3	212.2	214.1	214.0	212.3	211.1	209.8	208.7	206.9	204.5	200.1
V _m	613.6	698.5	704.0	703.1	697.3	693.1	688.5	684.8	678.8	671.1	656.5
V _m	187.0	212.9	214.6	214.3	212.5	211.3	209.9	208.7	206.9	204.6	200.1
V _θ	0	0	0	0	0	0	0	0	0	0	0
V _θ	0	0	0	0	0	0	0	0	0	0	0
V' _θ	-1021.4	-1079.3	-1130.5	-1178.9	-1225.6	-1270.8	-1314.8	-1357.8	-1400.1	-1441.9	-1484.6
V' _θ	-311.3	-329.0	-344.6	-359.3	-373.6	-387.3	-400.8	-413.9	-426.8	-439.5	-452.5
β _z	0	0	0	0	0	0	0	0	0	0	0
β _z	0	0	0	0	0	0	0	0	0	0	0
β' _z	59.12	57.17	58.14	59.22	60.38	61.40	62.37	63.24	64.14	65.04	66.15
β _z	1.032	0.998	1.015	1.034	1.054	1.072	1.089	1.104	1.119	1.135	1.155
ε	5.17	4.56	3.78	3.06	2.47	1.98	1.59	1.29	1.07	0.95	0.86
ε	0.090	0.080	0.066	0.053	0.043	0.035	0.028	0.023	0.019	0.017	0.015
U	1021.4	1079.3	1130.5	1178.9	1225.6	1270.8	1314.8	1357.8	1400.1	1441.9	1484.6
U	311.3	329.0	344.6	359.3	373.6	387.3	400.8	413.9	426.8	439.5	452.5
M _m	0.504	0.583	0.588	0.587	0.581	0.576	0.571	0.566	0.559	0.548	0.520
M _z	0.502	0.581	0.587	0.586	0.581	0.576	0.571	0.566	0.559	0.548	0.520
β _m	0	0	0	0	0	0	0	0	0	0	0
β _m	0	0	0	0	0	0	0	0	0	0	0
β' _m	59.00	57.09	58.08	59.18	60.36	61.39	62.36	63.24	64.13	65.04	66.15
β _m	1.030	0.996	1.014	1.033	1.054	1.071	1.088	1.104	1.119	1.135	1.155

APPENDIX 7

**Airfoil Sections on Conical Surfaces
(Multiple-Circular-Arc Definitions)**

TABLE 10
Airfoil Sections on Conical Surfaces - Rotor

Percent Flow ENGLISH UNITS	Inlet Root Diameter = 16.50 inches (0.4191 meter) Exit Root Diameter = 19.13 inches (0.4859 meter)		Inlet Tip Diameter = 33.04 inches (0.8382 meter) Exit Tip Diameter = 31.91 inches (0.8105 meter)		Multiple-Circular-Arc Airfoil, 30 Blades		Tangential Tilt = 0.034 inch (0.000864 meter)		Tip				
	Root	10.0	20.0	30.0	40.0	50.0	60.0	70.0		80.0	90.0		
	inches	16.541	19.08	21.22	23.081	24.757	26.299	27.742		29.112	30.43	31.71	
Diameter at leading edge	inches	4.4	4.4	4.4	4.4	4.4	4.4	4.4	4.4	4.4	4.4	4.4	4.4
c	inches	1.0	1.2	1.42	1.615	1.80	1.92	2.14	2.30	2.45	2.60	2.76	2.92
c/c		0.1	0.0892	0.08	0.072	0.0646	0.0576	0.0510	0.0443	0.0381	0.0318	0.0250	0.0182
% chord maximum thickness		53.0	54.0	55.0	57.0	58.0	60.0	62.0	64.0	65.0	67.0	70.0	70.0
s/c		0.5064	0.5066	0.5118	0.5180	0.5258	0.5307	0.5451	0.5728	0.6018	0.6307	0.6661	0.6961
RLE	inches	0.0200	0.0190	0.0180	0.0171	0.0161	0.0150	0.0140	0.0130	0.0120	0.0110	0.0100	0.0100
RTE	inches	0.0200	0.0179	0.0161	0.0145	0.0130	0.0115	0.0102	0.0089	0.0076	0.0064	0.0051	0.0051
β_1^*	degrees	54.84	56.45	57.50	58.35	59.08	59.88	60.69	61.57	62.60	63.72	64.49	64.49
β_1^*	degrees	48.41	50.02	53.01	54.57	55.93	57.46	58.49	59.79	61.16	62.60	63.72	63.72
ϕ	degrees	53.70	39.94	27.30	21.51	16.73	13.08	10.04	8.35	7.36	6.67	5.99	5.99
ϕ	degrees	9.53	8.57	7.57	6.50	5.39	4.37	3.46	2.30	1.29	0.41	-0.46	-0.46
ϵ	degrees	19.0	13.7	8.8	4.2	-0.2	-4.0	-7.0	-10.7	-14.2	-16.9	-17.0	-17.0
METRIC UNITS													
Diameter at leading edge	meter	0.42014	0.48489	0.53899	0.58626	0.62883	0.66800	0.70465	0.73944	0.77292	0.80543	0.83716	0.83716
c	meter	0.11176	0.11176	0.11176	0.11176	0.11176	0.11176	0.11176	0.11176	0.11176	0.11176	0.11176	0.11176
c/c	meter	0.02540	0.03048	0.03607	0.04102	0.04572	0.04877	0.05436	0.05842	0.06223	0.06604	0.07010	0.07010
% chord maximum thickness		53.0	54.0	55.0	57.0	58.0	60.0	62.0	64.0	65.0	67.0	70.0	70.0
s/c		0.5064	0.5066	0.5118	0.5180	0.5258	0.5307	0.5451	0.5728	0.6018	0.6307	0.6661	0.6961
RLE	meter	0.000508	0.000483	0.000457	0.000434	0.000409	0.000381	0.000356	0.000330	0.000305	0.000279	0.000254	0.000254
RTE	meter	0.000508	0.000455	0.000409	0.000368	0.000330	0.000292	0.000259	0.000226	0.000193	0.000163	0.000130	0.000130
β_1^*	radian	0.9570	0.9851	1.0034	1.0182	1.0309	1.0449	1.0590	1.0744	1.0924	1.1119	1.1254	1.1254
β_1^*	radian	0.8448	0.8728	0.9250	0.9522	0.9760	1.0024	1.0207	1.0433	1.0672	1.0924	1.1119	1.1119
ϕ	radian	0.9371	0.6970	0.4764	0.3753	0.2919	0.2282	0.1752	0.1457	0.1284	0.1164	0.1045	0.1045
ϕ	radian	0.1663	0.1370	0.1321	0.1134	0.0941	0.0763	0.0604	0.0401	0.0225	0.0072	-0.0080	-0.0080
ϵ	radian	0.3316	0.2391	0.1536	0.0733	-0.0035	-0.0698	-0.1222	-0.1867	-0.2478	-0.2949	-0.2967	-0.2967

Note: Tilt is the offset of the center of gravity at the tip from a radial line and varies linearly from the average actual root center of gravity

TABLE 11
Airfoil Sections on Conical Surfaces - Stator

Percent Flow	Inlet Root Diameter 19.88 inches (0.50495 meter)		20.0		30.0		40.0		50.0		60.0		70.0		80.0		90.0		Tip	
	Exit Root Diameter 21.00 inches (0.53340 meter)		22.640		23.810		24.910		25.960		26.970		27.940		28.870		29.790		30.770	
ENGLISH UNITS	Multiple-Circular-Arc Airfoil, 44 Vanes																			
Diameter at leading edge	inches	inches	inches	inches	inches	inches	inches	inches	inches	inches	inches	inches	inches	inches	inches	inches	inches	inches	inches	inches
c	19.830	21.380	21.380	21.380	21.380	21.380	21.380	21.380	21.380	21.380	21.380	21.380	21.380	21.380	21.380	21.380	21.380	21.380	21.380	21.380
c ₁	0.875	0.918	0.918	0.918	0.918	0.918	0.918	0.918	0.918	0.918	0.918	0.918	0.918	0.918	0.918	0.918	0.918	0.918	0.918	0.918
% chord maximum thickness	0.05	0.0525	0.0525	0.0525	0.0525	0.0525	0.0525	0.0525	0.0525	0.0525	0.0525	0.0525	0.0525	0.0525	0.0525	0.0525	0.0525	0.0525	0.0525	0.0525
a/c	54.25	54.70	54.70	54.70	54.70	54.70	54.70	54.70	54.70	54.70	54.70	54.70	54.70	54.70	54.70	54.70	54.70	54.70	54.70	54.70
RLE	0.0069	0.0073	0.0073	0.0073	0.0073	0.0073	0.0073	0.0073	0.0073	0.0073	0.0073	0.0073	0.0073	0.0073	0.0073	0.0073	0.0073	0.0073	0.0073	0.0073
RTE	0.0069	0.0073	0.0073	0.0073	0.0073	0.0073	0.0073	0.0073	0.0073	0.0073	0.0073	0.0073	0.0073	0.0073	0.0073	0.0073	0.0073	0.0073	0.0073	0.0073
β ₂ °	47.31	44.73	44.73	44.73	44.73	44.73	44.73	44.73	44.73	44.73	44.73	44.73	44.73	44.73	44.73	44.73	44.73	44.73	44.73	44.73
φ ₂ °	44.40	41.79	41.79	41.79	41.79	41.79	41.79	41.79	41.79	41.79	41.79	41.79	41.79	41.79	41.79	41.79	41.79	41.79	41.79	41.79
φ	57.70	52.68	52.68	52.68	52.68	52.68	52.68	52.68	52.68	52.68	52.68	52.68	52.68	52.68	52.68	52.68	52.68	52.68	52.68	52.68
φ ₁	7.54	9.86	9.86	9.86	9.86	9.86	9.86	9.86	9.86	9.86	9.86	9.86	9.86	9.86	9.86	9.86	9.86	9.86	9.86	9.86
ε	11.20	9.00	9.00	9.00	9.00	9.00	9.00	9.00	9.00	9.00	9.00	9.00	9.00	9.00	9.00	9.00	9.00	9.00	9.00	9.00

Percent Flow	Inlet Tip Diameter 30.82 inches (0.78283 meter)		30.0		40.0		50.0		60.0		70.0		80.0		90.0		Tip	
	Exit Tip Diameter 30.70 inches (0.77978 meter)		30.0		30.0		30.0		30.0		30.0		30.0		30.0		30.0	
METRIC UNITS	Multiple-Circular-Arc Airfoil, 44 Vanes																	
Diameter at leading edge	meter	meter	meter	meter	meter	meter	meter	meter	meter	meter	meter	meter	meter	meter	meter	meter	meter	meter
c	0.50622	0.54305	0.54305	0.54305	0.54305	0.54305	0.54305	0.54305	0.54305	0.54305	0.54305	0.54305	0.54305	0.54305	0.54305	0.54305	0.54305	0.54305
c ₁	0.07620	0.07620	0.07620	0.07620	0.07620	0.07620	0.07620	0.07620	0.07620	0.07620	0.07620	0.07620	0.07620	0.07620	0.07620	0.07620	0.07620	0.07620
% chord maximum thickness	0.05	0.0525	0.0525	0.0525	0.0525	0.0525	0.0525	0.0525	0.0525	0.0525	0.0525	0.0525	0.0525	0.0525	0.0525	0.0525	0.0525	0.0525
a/c	54.25	54.70	54.70	54.70	54.70	54.70	54.70	54.70	54.70	54.70	54.70	54.70	54.70	54.70	54.70	54.70	54.70	54.70
RLE	0.00175	0.00185	0.00185	0.00185	0.00185	0.00185	0.00185	0.00185	0.00185	0.00185	0.00185	0.00185	0.00185	0.00185	0.00185	0.00185	0.00185	0.00185
RTE	0.00175	0.00185	0.00185	0.00185	0.00185	0.00185	0.00185	0.00185	0.00185	0.00185	0.00185	0.00185	0.00185	0.00185	0.00185	0.00185	0.00185	0.00185
β ₂ °	0.82556	0.78054	0.78054	0.78054	0.78054	0.78054	0.78054	0.78054	0.78054	0.78054	0.78054	0.78054	0.78054	0.78054	0.78054	0.78054	0.78054	0.78054
φ ₂ °	0.77478	0.72924	0.72924	0.72924	0.72924	0.72924	0.72924	0.72924	0.72924	0.72924	0.72924	0.72924	0.72924	0.72924	0.72924	0.72924	0.72924	0.72924
φ	1.00687	0.91927	0.91927	0.91927	0.91927	0.91927	0.91927	0.91927	0.91927	0.91927	0.91927	0.91927	0.91927	0.91927	0.91927	0.91927	0.91927	0.91927
φ ₁	0.13157	0.17206	0.17206	0.17206	0.17206	0.17206	0.17206	0.17206	0.17206	0.17206	0.17206	0.17206	0.17206	0.17206	0.17206	0.17206	0.17206	0.17206
ε	0.1954	0.1571	0.1571	0.1571	0.1571	0.1571	0.1571	0.1571	0.1571	0.1571	0.1571	0.1571	0.1571	0.1571	0.1571	0.1571	0.1571	0.1571

APPENDIX 8
Rotor Slot Design

APPENDIX 8

Rotor Slot Design

A. Aerodynamic Design

A slot was designed for the multiple-circular-arc rotor with the objective of reducing shock losses and improving efficiency. Slot exit flow was used to deflect supersonic flow on the suction surface of the blade, causing an oblique shock upstream of the assumed normal shock position of the channel entrance, as shown in Figure 13. This oblique shock has low loss, and reducing the downstream Mach number gives lower normal shock losses. Recovery of the oblique and normal shock system is higher than the recovery of a single normal shock.

Investigations of slot chordwise position showed that placing the intersection of the rear slot wall and the suction surface at the assumed normal shock impingement point gave optimum results. When the slot was moved forward, the recovery was almost exactly the same for the oblique and normal shock combination, but flow behind the slot expanded to conform to the blade surface with nearly the original high Mach number. This resulted in an area of reduced loss in mid-channel but the original losses on the suction surface remained. Moving the slot aft reduced the channel area affected by the oblique shock.

Aerodynamic limits and practical limits of fabrication were determined. Parametric studies of overall shock recovery were made for slot designs falling within these boundaries. Results are shown in Figure 43 for the three radial positions defining the slot ends shown in Figure 44.

Rotor Slot Design Limits

1) Wedge Angle Limit

The relative Mach number on the suction surface of a blade determines the maximum wedge angle formed by the slot discharge air for which an attached oblique shock can exist.

2) Compression Limit

At a given radial location, total pressure at the slot exit was assumed to be equal to the total pressure at the leading edge, multiplied by the recovery of a normal shock at the blade inlet relative Mach number. In order to obtain flow rate control, slots were designed for choked exit flow which then specified the maximum static pressure at the slot exit for the corresponding total pressure. As the slot angle is increased, the oblique shock angle is increased with a corresponding rise in the static pressure downstream of

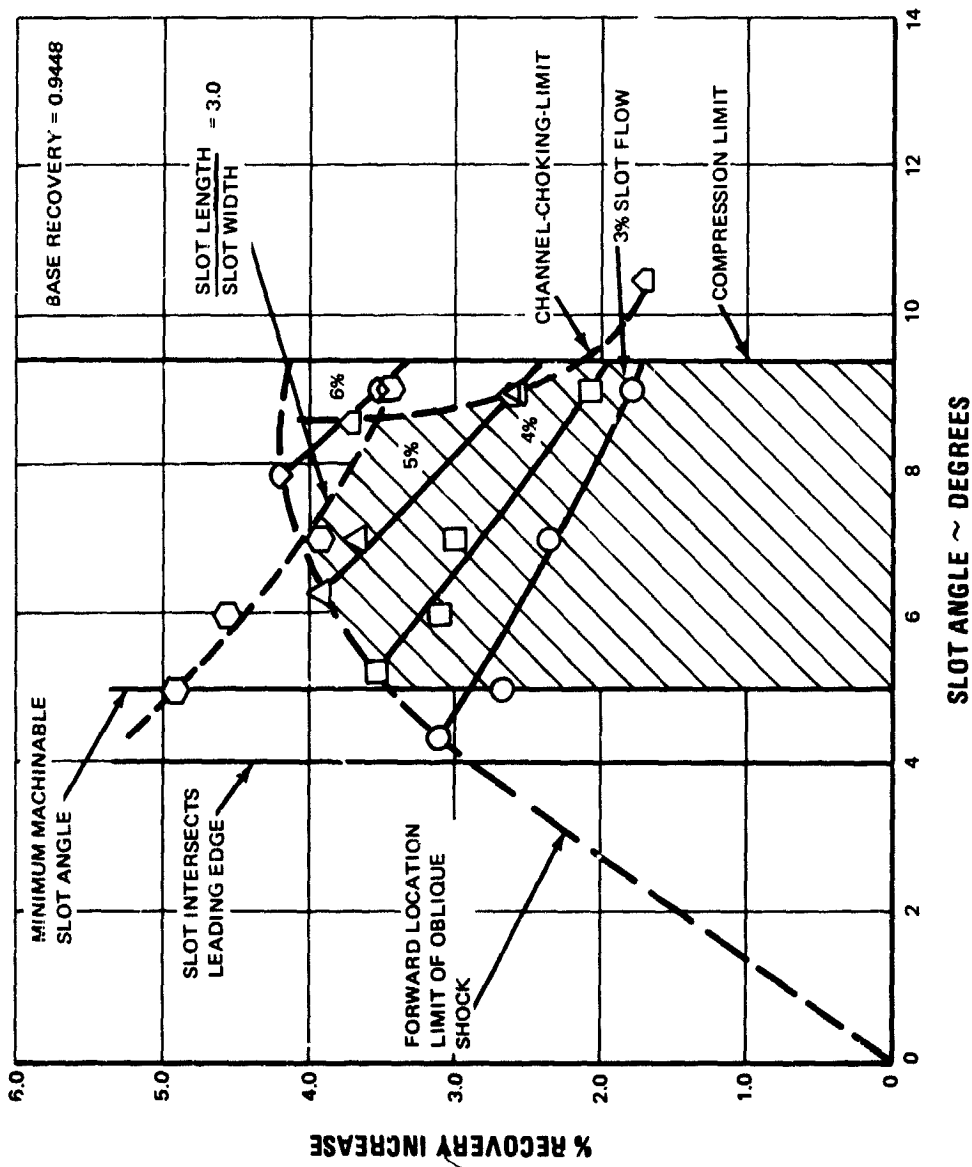


Figure 43 Recovery Increase vs Slot Angle
 a) Radius 14.0 Inches - 69.7% Span

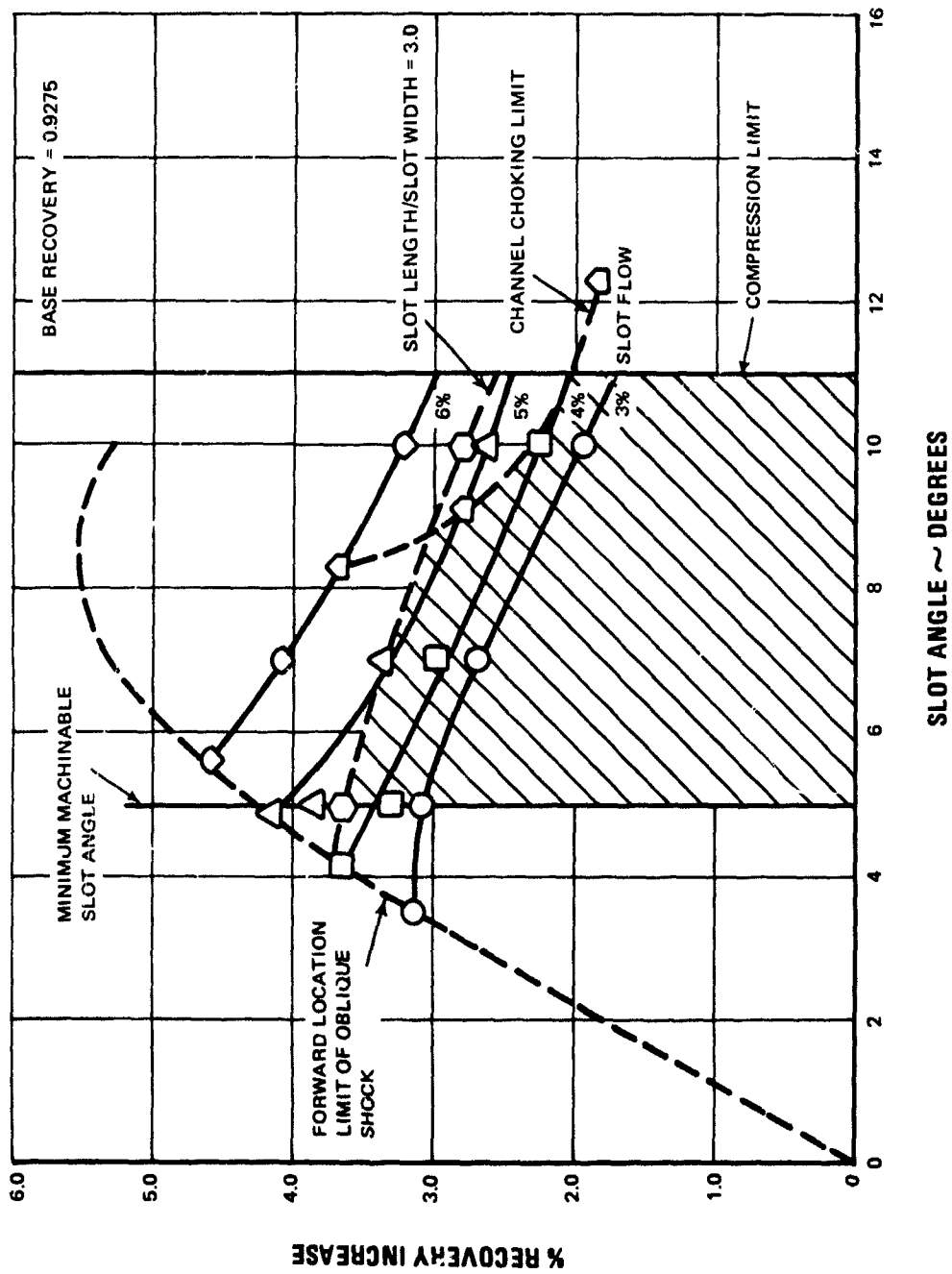
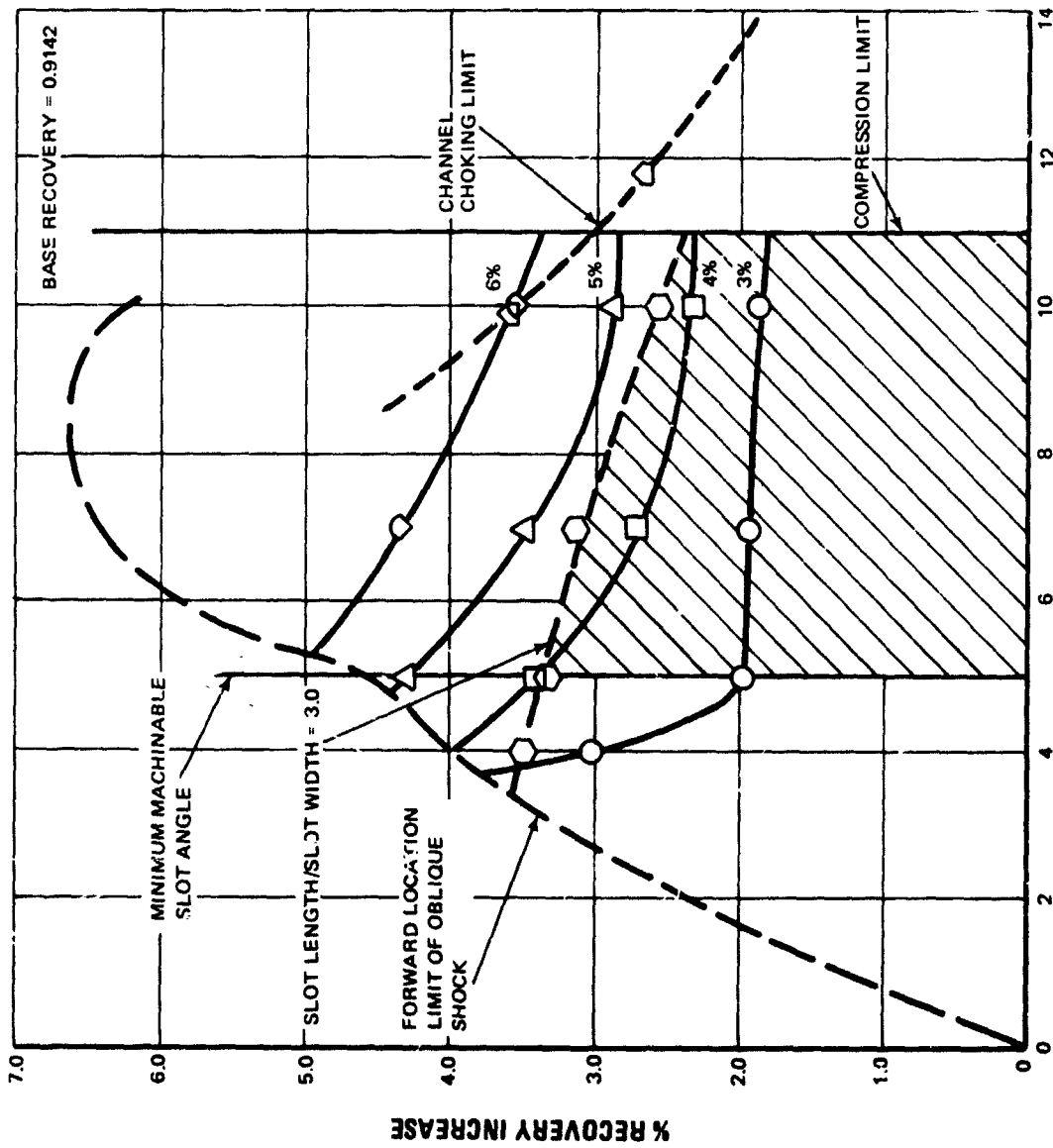


Figure 43 Recovery Increase vs Slot Angle
 b) Radius 15.0 Inches - 81.8% Span



SLOT ANGLE ~ DEGREES

Figure 43 Recovery Increase vs Slot Angle
c) Radius 15.75 Inches - 90.0% Span

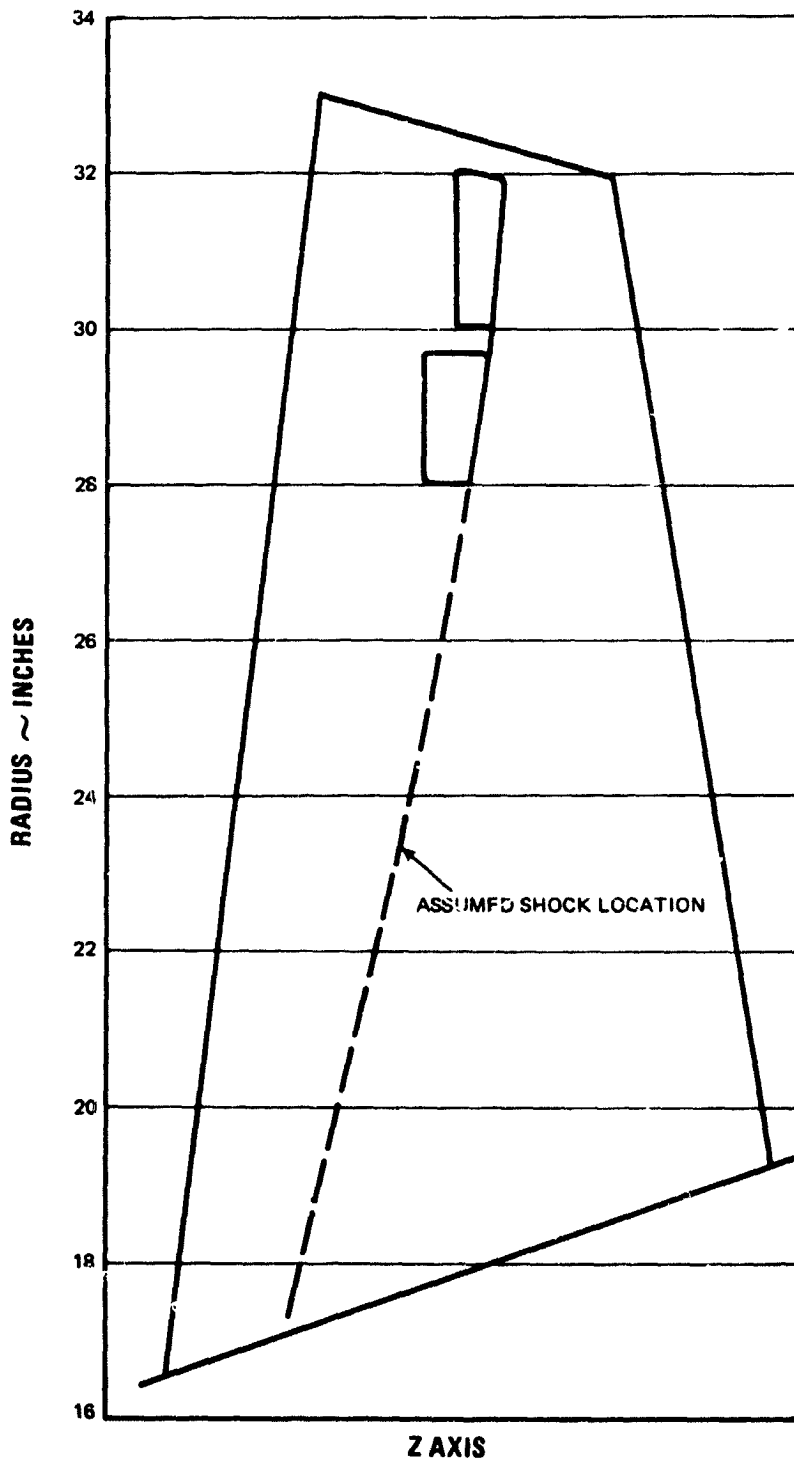


Figure 44 Axial Projection of Slotted Rotor

the oblique shock. The limiting slot angle occurs when the static pressure in the channel downstream of the oblique shock becomes greater than the static pressure in the slot. The assumption of a choked slot is valid only when it discharges into a region of lower static pressure. An oblique shock compression which would unchoke the slot would make calculations of slot flow, and of the oblique shock system, very complex. This slot angle limit was found to be less than the wedge-angle limit described in 1) and thus replaces it as an upper limit. It can be found on Figure 4.

3) Forward Location Limit of Oblique Shock

With a slot exit at the assumed normal shock location and a given slot angle, increasing slot width moves the starting point of the oblique shock towards the leading edge, so that it covers more of the channel. Finally, the oblique shock just reaches the leading edge of the adjacent rotor blade so that the entire channel is affected by the oblique shock. Any further increase in slot width will cause the oblique shock to extend in front of the leading edge of the adjacent blade and change the entire inlet-flow pattern. This limit is shown in Figure 43.

4) Slot Length-to-Width Ratio Limit

For a given radial station and slot angle, increasing slot width decreases the ratio of slot length to width. For flow guidance capabilities it was decided that the ratio of slot length to width should be greater than three. Any value less than this results in a poorly-defined throat where flow control is doubtful. The slot length was measured directly from drawings, taking into account the rounding off of sharp edges. These limits are shown in Figure 43.

5) Channel Choking Limit

For a given radial station the channel between two rotor blades has a given average Mach number and thus an a/a^* associated with it. But when slot flow is added to the channel flow, the reference a^* will increase and a/a^* will decrease towards one where choking may occur. This is partially offset by the increased recovery due to the oblique shock system. It is desired to keep a/a^* from decreasing more than two percent from the value of 1.03 originally in the channel. Thus:

$$\frac{a/a^*_{\text{original}}}{a/a^*_{\text{slot} + \text{original}}} = 1.02$$

This ratio is calculated using the relationship:

$$\frac{W_{\text{slot} + \text{original}}}{W_{\text{original}}} \times \frac{\text{recovery}_{\text{original}}}{\text{recovery}_{\text{original} + \text{slot}}} = \frac{a/a^*_{\text{original}}}{a/a^*_{\text{slot} + \text{original}}}$$

Thus percent flow rates of the slot are limited by channel choke considerations. Limits are shown in Figure 43.

6) Geometric Limits

(a) Slot Intersecting Rotor Blade Leading Edge

For highly cambered blades and for slots near the leading edge, the slot entrance can cut off the leading edge of the blade. These limits are shown in Figure 43.

(b) Machinable Slot Angle

Slot angles less than 5 degrees with the tangent to the section surface would compromise the dimensional accuracy of the slot because of machining tolerances. Fabrication limits are shown in Figure 43.

The shaded area in Figure 43 represents the feasible slot configurations at a particular radius.

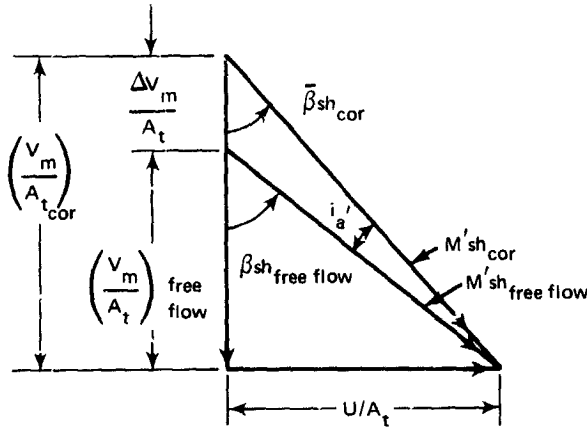
Calculation of Relative Mach Number at Shock Impingement Point

Calculations made in the parametric study of overall shock recovery depended on the channel Mach number distribution between the shock impingement point and the leading edge of the adjacent blade. The procedure used in determining this distribution was as follows.

Radial distributions of relative Mach number at the rotor leading edge and at the loci of shock impingement points on the blade suction surface were calculated using a stream-line analysis computer program. The calculation was made for free flow, with no blade effects. Resulting free-stream Mach numbers at the shock impingement points were corrected for blade blockage and boundary layer effects which increase the axial velocity and decrease the relative air angle. The calculation method is shown below.

$$\beta_{sh\ cor} = \beta_{sh, free\ flow} - i_a'$$

where i_a' , the blockage correction angle, is discussed in Appendix 3.



$A_t = \sqrt{\gamma RT_t}$ speed of sound at absolute stagnation temperature

Ratios of absolute velocity to the speed of sound at absolute stagnation temperature were used to determine corrected relative Mach numbers corresponding to adjusted axial velocities, as follows:

$$M_{sh \text{ free flow}} = M'_{sh \text{ free flow}} \cos \beta_{sh \text{ free flow}}$$

$$\left(\frac{V_m}{A_t}\right)_{\text{free flow}} = M_{sh \text{ free flow}} \sqrt{\frac{T}{T_t}} \quad \text{from tables}$$

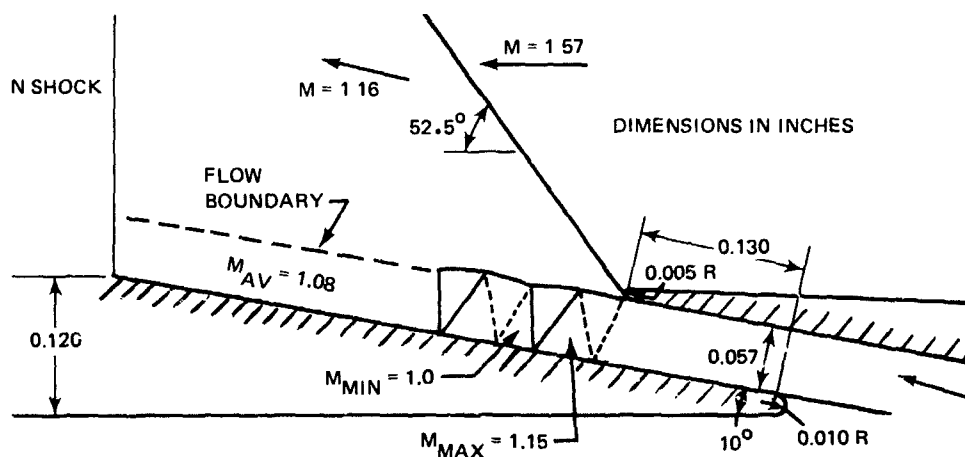
$$\left(\frac{V_m}{A_t}\right)_{\text{cor}} = \left(\frac{V_m}{A_t}\right)_{\text{free flow}} \left(\frac{\tan \bar{\beta}_{sh \text{ free flow}}}{\tan \bar{\beta}_{sh \text{ cor}}}\right)$$

$$M_{sh \text{ cor}} \text{ found from tables corresponding to } \left(\frac{V_m}{A_t}\right)_{\text{cor}}$$

$$M'_{sh \text{ cor}} = \frac{M_{sh \text{ cor}}}{\cos \beta_{sh \text{ cor}}}$$

This procedure uses the constant A_t based on absolute stagnation temperature as a reference for all geometrical corrections. The resulting relative Mach number $M'_{sh \text{ cor}}$ is the value at the shock impingement point corrected for blockage and boundary-layer effects. This corrected free streamline is not parallel to the suction surface, so the actual blade-surface relative Mach number was found as follows:

of the normal shock satisfy the usual boundary conditions. Sonic flow emerging from the slot expands to the static pressure determined by the oblique it causes. A method of characteristics solution of this flow showed that the outer boundary of the flow is only slightly irregular, and can be considered to be parallel to the rear slot wall, as shown in the sketch. As a result, the slot angle was used as the wedge angle for oblique



shock calculations. The procedure is as follows:

- 1) A slot or wedge angle Ω is chosen. Using M_{x_2} and this wedge angle, the shock angle ν is determined from Keenan and Kaye tables.
- 2) The Mach number normal to the oblique shock is determined from $(M_{x_2})_n = M_{x_2} \sin \nu$. This determines P_y/P_x from normal shock tables.
- 3) Downstream of the oblique shock, M_y is found from Keenan and Kaye tables, using Ω and ν from 1).
- 4) M_{y_n} , the normal component of M_y to the normal shock, is found from $M_{y_n} = M_y \sin (90 - \Omega)$. This determines P_5/P_y from normal shock tables.
- 5) Total recovery across the oblique and normal shock is found from $P_5/P_x = (P_5/P_y)(P_y/P_x)$
- 6) Mach number is found in the slot in the same manner as for wedge angle determination:
 - a) p_y/P_y found from isentropic tables for M_y
 - b) P_y/P_x found in Step 2
 - c) P_6/P_x found from normal shock tables for M_{x_2}
 - d) $P_{s1}/P_{s1} = P_y/P_6 = (p_y/P_y)(P_y/P_x)(P_x/P_6)$

- 7) M_{s1} is found from isentropic tables for this pressure ratio. P_4/P_{s1} is found from normal shock tables for $M_{s1n} \sin(90 - \Omega)$
- 8) Total recovery from Region X to Region 4 across the slot region is

$$P_1/P_X = (P_1/P_{s1})(P_6/P_X)$$
- 9) The recovery across the normal shock with no oblique shock present, corresponds to $M_{x_{av}}$. This is the base recovery from which all increases are measured.
- 10) The area weight factors for Regions 4, 5, and 6 are found by measuring the widths of the regions intersected by the shock pattern, and dividing them by the channel width. Thus the total recovery in the channel with the oblique is found by adding the products of the recoveries and their respective area weight factors.
- 11) Recovery increase is found by subtracting the P_6/P_X recovery corresponding to no oblique shock present, from the new recovery calculated in Step 10.

Efficiency Calculations

Adiabatic efficiency is given by

$$\eta = \frac{[T_2/T_1][\bar{R}_{total}]^{\frac{k-1}{k}} - 1}{T_2/T_1 - 1}$$

$$(1 - \bar{R}_{profile}) + (1 - \bar{R}_{shock}) = 1 - \bar{R}_{total}$$

$\bar{R}_{profile}$ is constant but the slot improves \bar{R}_{shock}

Efficiency was calculated for slotted and unslotted blade sections, using the corresponding \bar{R}_{total} values. Figure 45 is a plot of estimated rotor efficiency with and without slots, versus span.

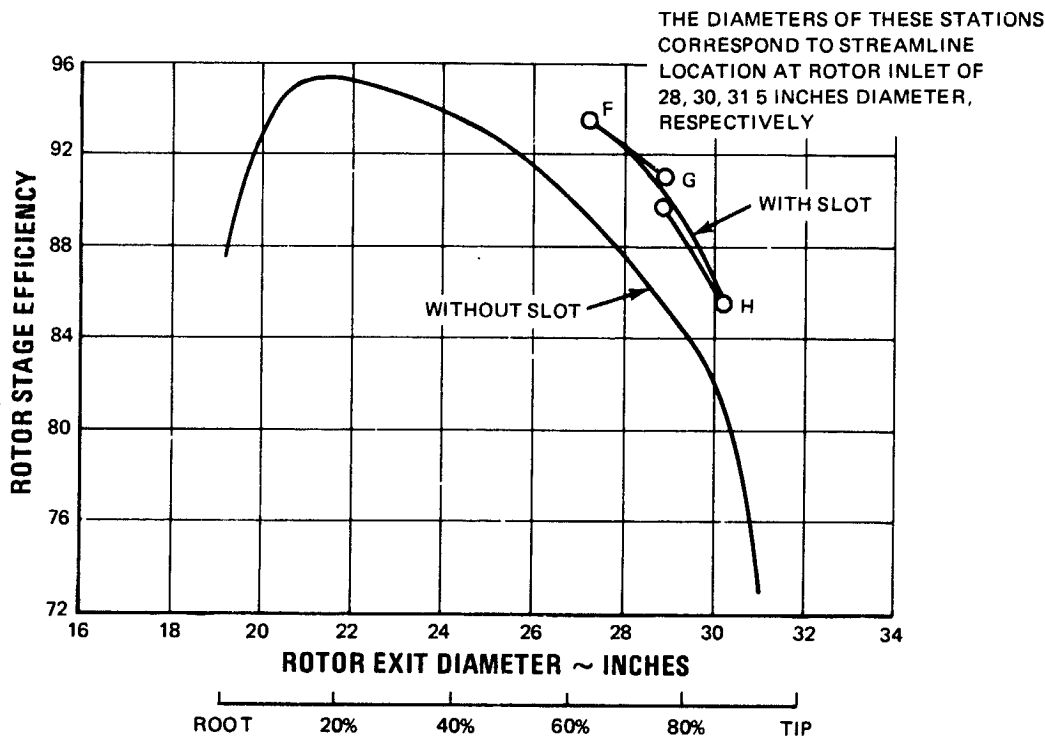


Figure 45 Rotor Efficiency vs Rotor Exit Diameter

B. Mechanical Design

Vibration Frequency

The coordinates of the slotted blade sections were used in calculating the blade first-mode vibration frequency of 500 cps at 110 percent of design speed. This is shown in Figure 46 to give adequate margin above the first-mode resonance caused by two excitations per revolution. Second-mode resonance frequency is 1030 cps.

A bending frequency of 842 cps was calculated for the rear outboard blade cantilevered at a radius of 14 inches where the slot begins, assuming no intermediate or tip bridges exist. A bending frequency of 1085 cps was calculated for the front outboard blade cantilevered at a radius of 14 inches. Neither frequency will resonate with 2E or 3E excitations per revolution.

Blade Steady-State Stress

At 110 percent of design speed maximum blade stress due to centrifugal and untwist effects occurs at the root leading edge of the blade and is 85,264 psi, which is below the maximum allowable of 116,000 psi for titanium (AMS 4929). This stress is lower than the MCA unslotted blade maximum steady-state stress of 89,400 psi at 110 percent of design speed. The results are summarized below.

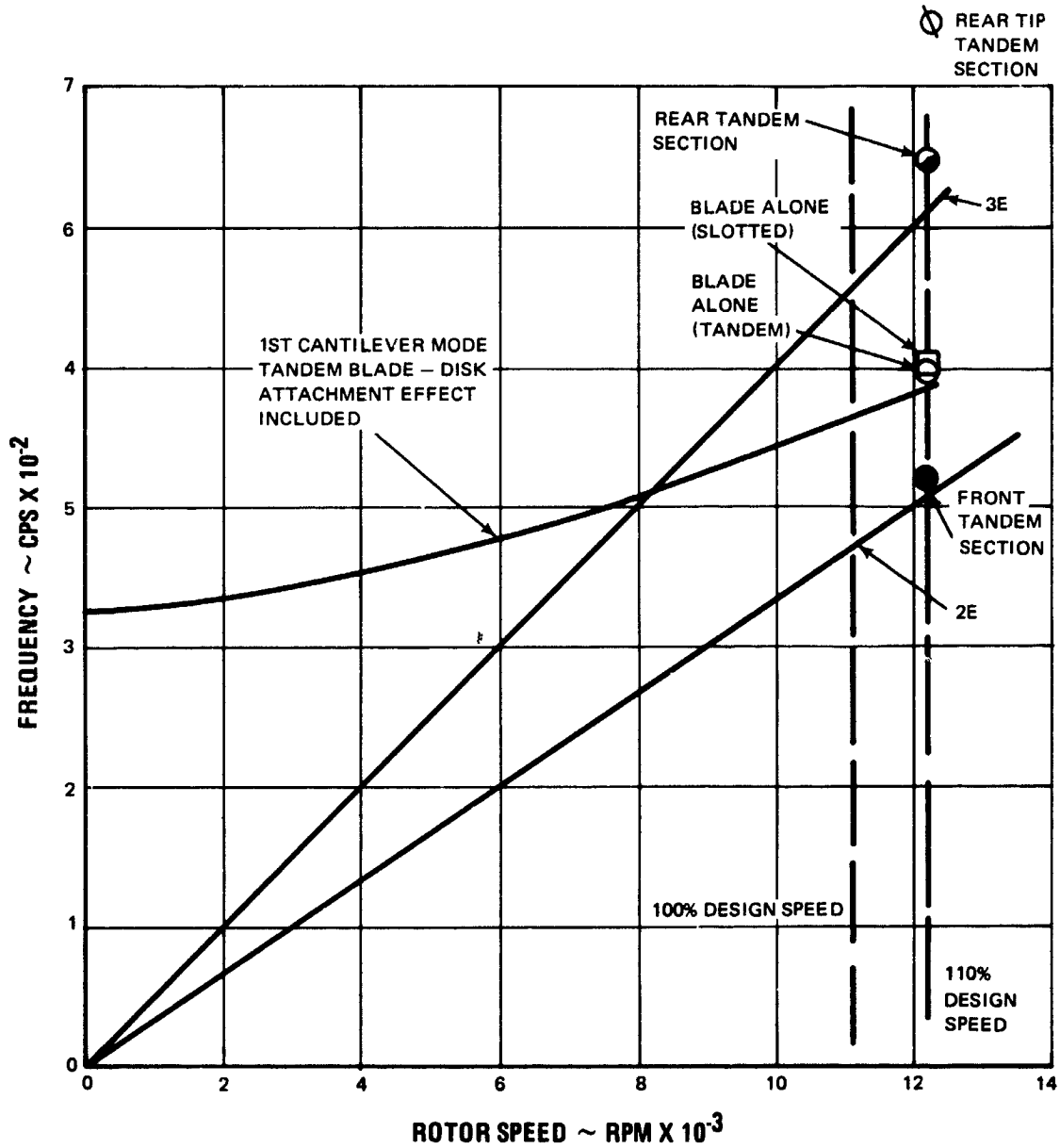


Figure 46 Rotor Blade Resonance Diagram

<u>Location</u>	<u>Calculated Stress, psi</u>	<u>Allowable Stress at 100°F, psi</u>
blade root P/A	34,843	69,000
blade root L/E, P/A untwist, tensile	85,457	116,000 (0.2% yield)
blade 10% from root, concave surface, max. thickness, P/A and untwist, tensile	76,604	116,000 (0.2% yield)

APPENDIX 9
Tandem Rotor Design

APPENDIX 9

Tandem Rotor Design

A. Aerodynamic Design

A tandem rotor was designed with the objectives of 1) minimizing shock losses by contouring the supersonic section of the suction surface to minimize supersonic acceleration, and 2) minimizing the effects of shock boundary-layer interactions, by initiating the diffusion process on a subsonic portion of the blade, where the boundary layer is no longer affected by the passage shock shown in Figure 14. Tandem blade sections were designed by shifting the portion of the multiple-circular-arc blade downstream of the normal shock impingement point, tangentially in the direction of rotation. In this way blade leading and trailing edge planes were kept the same as for the MCA blade and surface contours were kept the same except in the immediate region of the normal shock. Other criteria used in the tandem design are as follows:

- 1) The tandem shape was required only from a radius of 10.4 inches to the tip, since at that radius the local Mach number was less than 1.35, below which value boundary-layer separation was unlikely (Reference 9).
- 2) Near the hub the trailing-edge location of the forward section was placed downstream of the shock impingement to provide for possible boundary-layer reattachment. At the tip where the shock is very strong and there is little chance of reattachment, the front-section trailing edge was located immediately behind the shock-impingement point. Trailing edges of intermediate front sections follow a straight line on a projected view of the blade (Figure 47).
- 3) The slot width between the two tandem blade sections was made approximately 10 times the predicted total boundary-layer momentum thickness buildup on the pressure and suction surfaces at the assumed normal shock location. The slot length-to-width ratio was made equal to or greater than three whenever possible for directional guidance and flow-rate control.
- 4) Rear-section leading edge and front-section trailing edge radii were determined from results of a vibration stress test on various tandem-shaped test specimens.
- 5) Bridge width and blend radii were determined as a result of a stress study done on the proposed tandem design.
- 6) The stacking line was determined as a result of tilt stress considerations on the blade.
- 7) Smooth surface contours were maintained on front and rear sections.

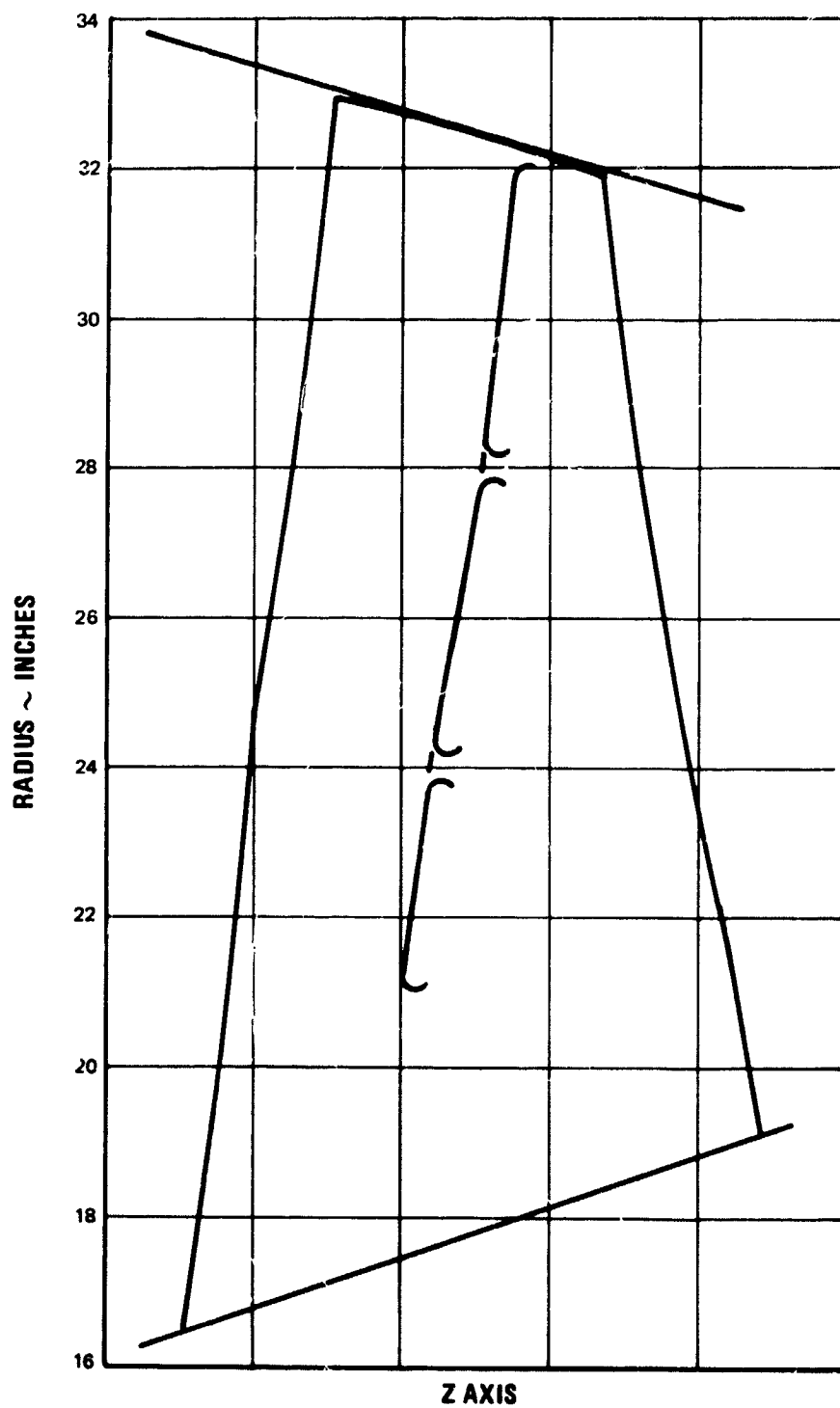
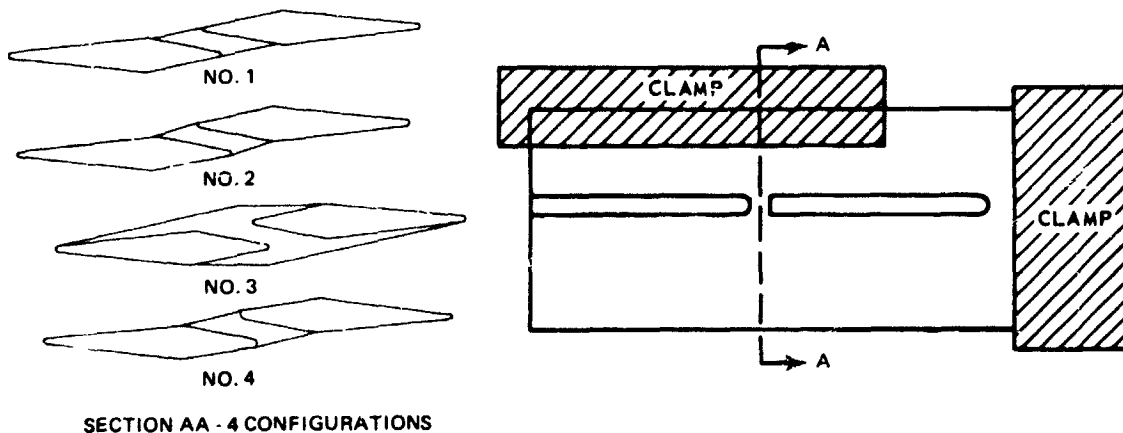


Figure 47 Axial Projection of Tandem Rotor

B. Mechanical Design

Bridge Fatigue Specimen Tests

Fatigue tests were run on sample tandem blades having bridges at mid-span between front and rear blades. Relative fatigue strengths of four bridge configurations were determined. A schematic drawing of a test specimen clamped to a shaker is shown in the sketch, together with sections of four bridge configurations. Specimen No. 1 was the basic configuration, No. 2 had increased overlap between front and rear tandem blades, No. 3 had the bridge extended outside the channel, and No. 4 had increased radii on blade edges intersecting the bridge. Relative strengths were judged



SECTION AA - 4 CONFIGURATIONS

on the basis of the vibratory stress measured by strain gages at maximum thickness at the radial height of the bridge. Stresses were not measured at failure points because slight variations in gage position in areas of high stress concentration produced scattered results.

All failures occurred at the airfoil bridge junction. Relative stresses for fatigue failures at approximately 10^7 cycles are tabulated below:

<u>Configuration</u>	<u>Stress or Reference Gage for Failure at 10^7 Cycles, psi</u>
1	3,500
2	10,000
3	7,500
4	15,000

From these tests it was determined that large blade-edge radii as in Configuration No. 4, and long blade overlap as in Configuration No. 2, were effective methods of obtaining fatigue strength. Both of these features were incorporated in the tandem blade design.

Vibration Frequency

Tandem blade section coordinates were used to determine airfoil section properties. These properties were then used to calculate first-mode vibration frequency of the blade. This frequency was adjusted to include the effect of disc attachment flexibility. At 110 percent of design speed the blade-alone frequency was 490.0 cps which is shown in Figure 46 to give adequate margin above the first-mode response caused by two excitations per revolution.

A bending frequency of 745 cps was calculated for the rearward outboard section cantilevered from a radius of 14 inches where a bridge is located (Figure 47). This frequency is lower than that of the front section cantilevered at the same radius. The front section cantilevered at a radius of 10.4 inches where the tandem sections start has a bending frequency of 418 cps, close to the 2E value of 408 cps at 110 percent of design speed. The rear section cantilevered at a radius of 10.4 inches has a bending frequency of 645 cps, which is well above the 3E value of 608 cps at 110 percent of design speed. These values are shown in Figure 46. The assumption of cantilevered blades gives very conservative results, since the blades are actually fixed at more than one position, which will tend to increase the natural bending frequency. It was concluded that the isolated tandem-section frequencies are less critical than the full-blade system.

Blade Steady-State Stress

Combined centrifugal pull and untwisting stresses were calculated at 110 percent of design speed. A comparison was made to allowable stresses based on the use of AMS 4928 titanium alloy at 150°F (338°K).

The maximum local stress occurs at the root leading edge of the blade, which from past experience is not a problem. The combined stress at 10 percent span at the maximum thickness point was calculated to be 76,604 psi compared to 74,000 psi for the MCA blade at 110 percent of design speed, well below the 0.2 percent yield strength of 116,000 psi for titanium. The results are summarized below.

<u>At 110 Percent of Design Speed</u>		
<u>Location</u>	<u>Calculated Stress, psi</u>	<u>Allowable Stress at 100°F, psi</u>
blade root P/A, tensile	41,517	69,000
blade root L/E, P/A untwist, tensile	85,457	113,000 (0.2% yield)
blade 10% out from root, concave surface, max. thickness, P/A + untwist, tensile	76,604	116,000 (0.2% yield)

Bridge Steady-State Stress

Centrifugal loads, untwist torques, and bending moments due to gas loads and nonradial stacking were used to calculate shear and bending stresses on the three bridge sections. Three types of stress calculations were made.

The first type of calculation was based on the assumption that the bridges equalize the radial elongations of the front and rear spanwise lengths between bridges by absorbing the difference between centrifugal loads that would occur if front and rear were unrestrained and the loads that will occur when the bridges restrain them. The untwist program for the tandem-blade system gave the qualitative result that centrifugal loads constituted the major stress for all tandem sections, and was constant for a cross-section at a given radius. Since elongation is directly proportional to stress, equal elongation of front and rear tandem sections was assumed in calculating loads on a spanwise length between bridges in the restrained condition. Centrifugal loads were determined for the individual front and rear tandem sections, and the difference between the restrained and unrestrained centrifugal loads was used to calculate a shear and bending stress in the bridge.

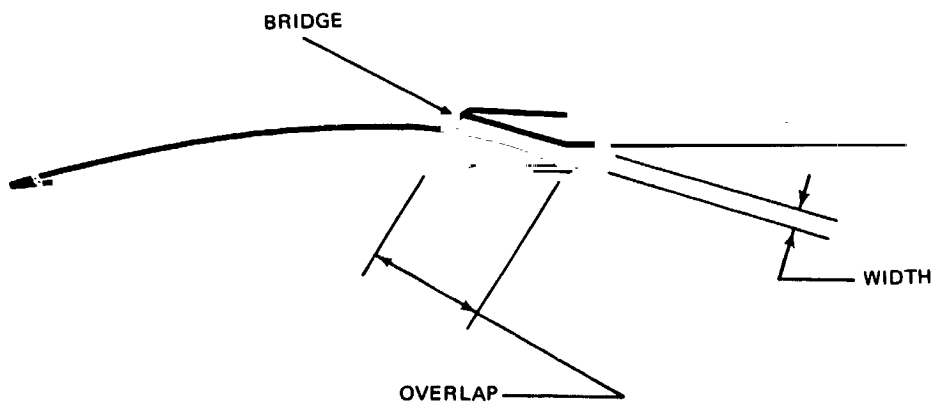
The second type of calculation treated the bridge as a beam with fixed ends and with a center couple. A bridge bending stress was calculated based on the conservative assumption that the entire untwist torque due to the tandem blade system outboard of the bridge acts on the bridge as a center couple.

The third type of calculation involved stresses due to gas bending and center-of-gravity offset from a radial stacking line. It was not possible to stack the tandem blade so that centers of gravity of the combined front and rear sections lay on one straight line. This resulted in blade bending stresses due to centrifugal loads. A program which calculates fiber stresses due to center-of-gravity offset and gas-bending loads was used to determine the radial distribution of blade section stresses for a tangential tilt of 0.030 inch, the value which gives minimum root bending stresses. The individual front and rear blades were divided into free-body diagrams by horizontal planes passing through the blades approximately midway between bridges. The bending moments and moments of inertia for the airfoil sections at the radial positions of the free-body ends were used to calculate the bending stress at the centers of gravity of front and rear sections. Radial loads were calculated on free-body ends by assuming that the average stress on a blade section was equal to the stress at its center of gravity.

It was observed that the front section was in compression and the rear section in tension. The difference in radial loads on the front-section free body and the difference in loads on the rear-section free body were found to be of comparable magnitude and in the opposite direction. These loads were used to calculate a shear and bending stress similar to those due to centrifugal loads.

The results of the three calculations are summarized below for the two inner bridges of 0.15 inch radial height, 1.0 inch overlap, and 0.15 inch width.

<u>Radial Location</u>	<u>12.0 inches</u>	<u>14.0 inches</u>
1) equal elongation stress	shear = 11,200 psi bending = 33,500 psi	shear = 9,700 psi bending = 28,900 psi
2) untwist-moment stress	bending = 15,000 psi	bending = 6,200 psi
3) tilt stress	shear = 1,960 psi bending = 5,880 psi	shear = lower bending = lower
<u>Resultant Stress</u>	shear = 13,160 psi bending = 54,380 psi	<u>Allowable</u> 66,000 psi 116,000 psi



APPENDIX 10

Airfoil Coordinates for Manufacturing Sections

TABLE 12

Rotor Coordinates - Sections A, B, C and D

ENGLISH UNITS		A-A	B-B	C-C	D-D
Sect					
Radius inches		9.90	10.40	11.00	12.00
c inches		4.2480	4.3415	4.3900	4.4190
γ degrees		32.97	37.84	41.99	47.98
ȳ inches		0.3980	0.2956	0.2294	0.1445
X̄ inches		2.2978	2.3237	2.3413	2.3601

STA	X	Y	X	Y	X	Y	X	Y
1	0.0000	0.0000	0.0000	0.0000	0.0000	0.0000	0.0000	0.0000
2	0.0000	-0.0170	0.0000	-0.0175	0.0000	-0.0170	0.0000	-0.0158
3	0.4248	0.0990	0.4342	0.0720	0.4390	0.0515	0.4419	0.0255
4	0.8496	0.1865	0.8683	0.1355	0.8780	0.0992	0.8838	0.0520
5	1.2744	0.2440	1.3024	0.1735	1.3170	0.1250	1.3257	0.0635
6	1.6992	0.2820	1.7366	0.1920	1.7560	0.1320	1.7676	0.0610
7	2.1240	0.3020	2.1708	0.1970	2.1950	0.1305	2.2095	0.0515
8	2.5488	0.3060	2.6049	0.1890	2.6340	0.1200	2.6514	0.0395
9	2.9736	0.2856	3.0390	0.1670	3.0730	0.1010	3.0933	0.0262
10	3.3984	0.2335	3.4732	0.1275	3.5120	0.0738	3.5352	0.0125
11	3.8232	0.1415	3.9074	0.0680	3.9510	0.0350	3.9771	-0.0019
12	4.2480	-0.0200	4.3415	-0.0160	4.3900	-0.0140	4.4190	-0.0120
13	4.2480	0.0250	4.3415	0.0190	4.3900	0.0160	4.4190	0.0132
14	3.8232	0.3625	3.9074	0.2550	3.9510	0.2015	3.9771	0.1420
15	3.3984	0.5505	3.4732	0.4130	3.5120	0.3340	3.5352	0.2390
16	2.9736	0.6532	3.0390	0.5110	3.0730	0.4192	3.0933	0.3055
17	2.5488	0.6942	2.6049	0.5575	2.6340	0.4625	2.6514	0.3400
18	2.1240	0.6850	2.1708	0.5605	2.1950	0.4680	2.2095	0.3435
19	1.6992	0.6300	1.7366	0.5190	1.7560	0.4335	1.7676	0.3140
20	1.2744	0.5255	1.3024	0.4350	1.3170	0.3615	1.3257	0.2600
21	0.8496	0.3835	0.8683	0.3170	0.8780	0.2645	0.8838	0.1920
22	0.4248	0.2130	0.4342	0.1785	0.4390	0.1500	0.4419	0.1102
23	0.0000	0.0185	0.0000	0.0180	0.0000	0.0170	0.0000	0.0165

METRIC UNITS		A-A	B-B	C-C	D-D
LER	0.0182	0.0179	0.0175	0.0165	
TER	0.0207	0.0188	0.0169	0.0142	

Sect.	A-A	B-B	C-C	D-D
Radius meters	0.25150	0.26420	0.27940	0.30480
c meters	0.107899	0.110274	0.111506	0.112242
γ radians	0.57533	0.66031	0.73273	0.83725
ȳ meters	0.010108	0.007508	0.005826	0.003670
X̄ meters	0.058364	0.059021	0.059469	0.059946

STA	X	Y	X	Y	X	Y	X	Y
1	0.00000	0.000000	0.000000	0.000000	0.000000	0.000000	0.000000	0.000000
2	0.000000	-0.000431	0.000000	-0.000444	0.000000	-0.000431	0.000000	-0.000401
3	0.010789	0.002514	0.010982	0.001828	0.011150	0.001308	0.011224	0.000647
4	0.021579	0.004737	0.022054	0.003441	0.022301	0.002519	0.022448	0.001320
5	0.032369	0.006197	0.033080	0.004406	0.033451	0.003175	0.033672	0.001612
6	0.043159	0.007162	0.044109	0.004876	0.044602	0.003352	0.044897	0.001549
7	0.053949	0.007670	0.055138	0.005003	0.055753	0.003314	0.056121	0.001308
8	0.064739	0.007772	0.066164	0.004800	0.066903	0.003048	0.067345	0.001003
9	0.075529	0.007254	0.077190	0.004241	0.078054	0.002577	0.078569	0.000665
10	0.086319	0.005930	0.088219	0.003238	0.089204	0.001874	0.089794	0.000317
11	0.097109	0.003594	0.099247	0.001727	0.100355	0.000889	0.101018	-0.000025
12	0.107899	-0.000508	0.110274	-0.000406	0.111506	-0.000355	0.112242	-0.000304
13	0.107890	0.000635	0.110274	0.000482	0.111506	0.000406	0.112242	0.000335
14	0.097109	0.009207	0.099247	0.006477	0.100355	0.0051181	0.101018	0.003606
15	0.086319	0.013982	0.088219	0.010490	0.089204	0.008483	0.089794	0.006070
16	0.075529	0.016591	0.077190	0.012979	0.078054	0.010647	0.078569	0.007759
17	0.064739	0.017632	0.066164	0.014160	0.066903	0.011747	0.067345	0.008636
18	0.053949	0.017399	0.055138	0.014236	0.055753	0.011887	0.056121	0.008724
19	0.043159	0.016002	0.044109	0.013182	0.044602	0.011010	0.044897	0.007975
20	0.032369	0.013347	0.033080	0.011049	0.033451	0.009182	0.033672	0.006604
21	0.021579	0.009740	0.022054	0.008051	0.022301	0.006718	0.022448	0.004876
22	0.010789	0.005410	0.010982	0.004533	0.011150	0.003810	0.011224	0.0027990
23	0.000000	0.000469	0.000000	0.000457	0.000000	0.000431	0.000000	0.000419

LER	0.000462	0.000454	0.000444	0.000419
TER	0.000525	0.000477	0.000429	0.000360

TABLE 13

Rotor Coordinates - Sections E, F, G and H

ENGLISH UNITS		Sect.	E-E	F-F	G-G	H-H
	radius	inches	13.0	14.0	15.0	15.75
	c	inches	4.4215	4.3977	4.3705	4.3565
	γ	degrees	53.54	58.03	62.44	65.04
	ȳ	inches	0.0813	0.0365	0.0109	0.0128
	X̄	inches	2.3705	2.3697	2.3598	2.3608

STA	X	Y	X	Y	X	Y	X	Y
1	0.0000	0.0000	0.0000	0.0000	0.0000	0.0000	0.0000	0.0000
2	0.0000	-0.0150	0.0000	-0.0135	0.0000	-0.0115	0.0000	-0.0110
3	0.4422	0.0062	0.4398	-0.0058	0.4370	-0.0135	0.4356	-0.0142
4	0.8843	0.0172	0.8795	-0.0040	0.8741	-0.0188	0.8713	-0.0172
5	1.3264	0.0195	1.3193	-0.0090	1.3112	-0.0258	1.3070	-0.0205
6	1.7686	0.0120	1.7591	-0.0180	1.7482	-0.0332	1.7426	-0.0236
7	2.2108	-0.0020	2.1988	0.0302	2.1852	-0.0405	2.1782	-0.0240
8	2.6529	-0.0130	2.6386	-0.0407	2.6223	-0.0450	2.6139	-0.0245
9	3.0950	-0.0210	3.0784	-0.0455	3.0594	-0.0450	3.0496	-0.0220
10	3.5372	-0.0240	3.5182	-0.0410	3.4964	-0.0372	3.4852	-0.0165
11	3.9794	-0.0218	3.9579	-0.0290	3.9334	-0.0240	3.9208	-0.0105
12	4.4215	-0.0110	4.3977	-0.0073	4.3705	-0.0055	4.3565	-0.0065
13	4.4215	0.0105	4.3977	0.0088	4.3705	0.0062	4.3565	0.0050
14	3.9794	0.1015	3.9579	0.0730	3.9334	0.0575	3.9208	0.0565
15	3.5372	0.1715	3.5182	0.1210	3.4964	0.0902	3.4852	0.0882
16	3.0950	0.2185	3.0784	0.1520	3.0594	0.1080	3.0496	0.0990
17	2.6529	0.2425	2.6386	0.1642	2.6223	0.1095	2.6139	0.0925
18	2.2108	0.2408	2.1988	0.1575	2.1852	0.0960	2.1782	0.0782
19	1.7686	0.2155	1.7591	0.1380	1.7482	0.0830	1.7426	0.0630
20	1.3264	0.1790	1.3193	0.1150	1.3112	0.0675	1.3070	0.0505
21	0.8843	0.1320	0.8795	0.0870	0.8741	0.0520	0.8713	0.0378
22	0.4422	0.0784	0.4398	0.0535	0.4370	0.0335	0.4356	0.0240
23	0.0000	0.0140	0.0000	0.0135	0.0000	0.0125	0.0000	0.0110
LER	0.0152		0.0137		0.0121		0.0108	
TER	0.0113		0.0088		0.0063		0.0053	

METRIC UNITS		Sect.	E-E	F-F	G-G	H-H
	radius	meters	0.33020	0.35560	0.38100	0.40005
	c	meters	0.112306	0.111701	0.111010	0.110655
	γ	radians	0.93427	1.01262	1.08958	1.13495
	ȳ	meters	0.002065	0.000927	0.000276	0.000325
	X̄	meters	0.060210	0.060190	0.059938	0.059964

STA	X	Y	X	Y	X	Y	X	Y
1	0.000000	0.000000	0.000000	0.000000	0.000000	0.000000	0.000000	0.000000
2	0.000000	-0.000381	0.000000	-0.000342	0.000000	-0.000292	0.000000	-0.000279
3	0.011231	0.000157	0.011170	-0.000147	0.011099	-0.000342	0.011064	-0.000360
4	0.022461	0.000436	0.022339	-0.000101	0.022202	-0.000477	0.022131	-0.000436
5	0.033690	0.000495	0.033510	-0.000228	0.033304	-0.000655	0.033197	-0.000520
6	0.044922	0.000304	0.044681	-0.000457	0.044404	-0.000843	0.044262	-0.000599
7	0.056154	-0.000050	0.055849	0.000767	0.055504	-0.001028	0.055326	-0.000609
8	0.067383	-0.000330	0.067020	-0.001033	0.066606	-0.001143	0.066393	-0.000622
9	0.078613	-0.000533	0.078191	-0.001155	0.077708	-0.001143	0.077459	-0.000558
10	0.089844	-0.000509	0.089362	-0.001041	0.088808	-0.000944	0.088524	-0.000419
11	0.101076	-0.000553	0.100536	-0.000736	0.099908	-0.000609	0.099588	-0.000266
12	0.112306	-0.000279	0.111701	-0.000198	0.111010	-0.000139	0.110655	-0.000165
13	0.112306	0.000266	0.111701	0.000223	0.111010	0.000157	0.110655	0.000127
14	0.101076	0.002578	0.100530	0.001854	0.099908	0.001460	0.099588	0.001435
15	0.089844	0.004356	0.089362	0.003073	0.088808	0.002291	0.088524	0.002240
16	0.078613	0.005549	0.078191	0.003860	0.077708	0.002743	0.077459	0.002514
17	0.067383	0.006159	0.067020	0.004170	0.066606	0.002781	0.066393	0.002349
18	0.056154	0.006116	0.055849	0.004000	0.055504	0.002-38	0.055326	0.001986
19	0.044922	0.005473	0.044681	0.003505	0.044404	0.002108	0.044262	0.001600
20	0.033690	0.004546	0.033510	0.002921	0.033304	0.001714	0.033197	0.001282
21	0.022461	0.003378	0.022339	0.002209	0.022202	0.001320	0.022131	0.000960
22	0.011231	0.001991	0.011170	0.001358	0.011099	0.000850	0.011064	0.000609
23	0.000000	0.000355	0.000000	0.000342	0.000000	0.000317	0.000000	0.000279
LER	0.000386		0.000347		0.000307		0.000274	
TER	0.000287		0.000223		0.000160		0.000134	

TABLE 14

Rotor Coordinates - Sections J, K, L and M

ENGLISH UNITS		Sect.	J-J	K-K	L-L	M-M		
radius	inches		8.35	8.85	9.35	16.5		
c	inches		4.0615	4.0630	4.1238	4.3346		
γ	degrees		10.39	18.53	26.92	66.88		
\bar{Y}	inches		0.9024	0.7270	0.5657	0.0048		
\bar{X}	inches		2.1237	2.1957	2.2503	2.3615		
STA	X	Y	X	Y	X	Y	X	Y
1	0.0000	0.0000	0.0000	0.0000	0.0000	0.0000	0.0000	0.0000
2	0.0000	0.0222	0.0000	-0.0190	0.0000	-0.0190	0.0000	-0.0094
3	0.4062	0.2762	0.4063	0.2020	0.4124	0.1460	0.4335	-0.0122
4	0.8123	0.5040	0.8126	0.3765	0.8248	0.2750	0.8469	-0.0166
5	1.2184	0.6780	1.2189	0.5106	1.2371	0.3690	1.3004	-0.0194
6	1.6246	0.8080	1.6252	0.6135	1.6495	0.4395	1.7338	-0.0210
7	2.0308	0.8908	2.0315	0.6800	2.0619	0.4860	2.1673	-0.0208
8	2.4369	0.9140	2.4378	0.7005	2.4743	0.5037	2.6008	-0.0178
9	2.8430	0.8665	2.8441	0.6685	2.8867	0.4615	3.0342	-0.0132
10	3.2492	0.7250	3.2504	0.5650	3.2990	0.4050	3.4677	-0.0082
11	3.6554	0.4578	3.6567	0.3575	3.7114	0.2535	3.9011	-0.0060
12	4.0615	-0.0270	4.0630	-0.0250	4.1238	-0.0215	4.3346	-0.0036
13	4.0615	0.3750	4.0630	0.0370	4.1238	0.0322	4.3346	0.0020
14	3.6554	0.7132	3.6567	0.6330	3.7114	0.5140	3.9011	0.0470
15	3.2492	1.0848	3.2504	0.9330	3.2990	0.7610	3.4677	0.0724
16	2.8430	1.2835	2.8441	1.0840	2.8867	0.8800	3.0342	0.0790
17	2.4369	1.3620	2.4378	1.1355	2.4743	0.9175	2.6008	0.0670
18	2.0308	1.3452	2.0315	1.1100	2.0619	0.8918	2.1673	0.0526
19	1.6246	1.2465	1.6252	1.0140	1.6495	0.8115	1.7338	0.0414
20	1.2184	1.0688	1.2189	0.8510	1.2371	0.6768	1.3004	0.0320
21	0.8123	0.8005	0.8126	0.6222	0.8248	0.4915	0.8669	0.0234
22	0.4062	0.4440	0.4063	0.3410	0.4124	0.2702	0.4335	0.0164
23	0.0000	0.0260	0.0000	0.0225	0.0000	0.1950	0.0000	0.0094
LER	0.0185		0.0182		0.0185		0.0094	
TER	0.0166		0.0181		0.0199		0.0032	
METRIC UNITS		Sect.	J-J	K-K	L-L	M-M		
radius	meters		0.21209	0.22479	0.23749	0.41910		
c	meters		0.103162	0.103200	0.104744	0.110098		
γ	radians		0.18131	0.32335	0.46975	1.16706		
\bar{Y}	meters		0.022920	0.018465	0.014368	0.000121		
\bar{X}	meters		0.053941	0.055770	0.057157	0.059982		
STA	X	Y	X	Y	X	Y	X	Y
1	0.000000	0.000000	0.000000	0.000000	0.000000	0.000000	0.000000	0.000000
2	0.000000	-0.000563	0.000000	-0.000482	0.000000	-0.000482	0.000000	-0.000238
3	0.010317	0.007015	0.010320	0.005130	0.010474	0.003708	0.011010	-0.000309
4	0.020632	0.012801	0.020640	0.009563	0.020949	0.006985	0.022019	-0.000421
5	0.030947	0.017221	0.030960	0.012969	0.031422	0.009372	0.033030	-0.000492
6	0.041264	0.020523	0.041280	0.015582	0.041897	0.011163	0.044038	-0.000533
7	0.051582	0.022809	0.051600	0.017272	0.052372	0.012344	0.055049	-0.000528
8	0.061897	0.023215	0.061920	0.017792	0.062847	0.012781	0.066060	-0.000452
9	0.072212	0.022009	0.072240	0.016979	0.073322	0.012230	0.077068	-0.000335
10	0.082529	0.018415	0.082560	0.014351	0.083794	0.010307	0.088079	-0.000208
11	0.092847	0.011628	0.092880	0.009080	0.094269	0.006438	0.099087	-0.000152
12	0.103162	-0.000685	0.103200	-0.000635	0.104744	-0.000546	0.110098	-0.000091
13	0.103162	0.009525	0.103200	0.009939	0.104744	0.008817	0.110098	0.000071
14	0.092847	0.018115	0.092880	0.016078	0.094269	0.013055	0.099087	0.001193
15	0.082529	0.027553	0.082560	0.023698	0.083794	0.019329	0.088079	0.001838
16	0.072212	0.032600	0.072240	0.027533	0.073322	0.022352	0.077068	0.002006
17	0.061897	0.034594	0.061920	0.028841	0.062847	0.023304	0.066060	0.001701
18	0.051582	0.034168	0.051600	0.028194	0.052372	0.022651	0.055049	0.001336
19	0.041264	0.031661	0.041280	0.025755	0.041897	0.020612	0.044038	0.001051
20	0.030947	0.027147	0.030960	0.021615	0.031422	0.017190	0.033030	0.000812
21	0.020632	0.020332	0.020640	0.015803	0.020949	0.012484	0.022019	0.000594
22	0.010317	0.011277	0.010320	0.008661	0.010474	0.006863	0.011010	0.000416
23	0.000000	0.000660	0.000000	0.000571	0.000000	0.004953	0.000000	0.000238
LER	0.000469		0.000462		0.000469		0.000238	
TER	0.000421		0.000459		0.000505		0.000081	

TABLE 15

Stator Coordinates - Sections A, B, C and D

ENGLISH UNITS		Sect	A-A	B-B	C-C	D-D
	Radius inches		10.6	11.0	11.75	12.5
c	inches		2.9635	2.9760	2.9850	2.9940
γ	degrees		18.68	17.91	16.37	15.18
Ȳ	inches		0.2931	0.2755	0.2693	0.2665
Ȳ	inches		1.5618	1.5717	1.5813	1.5913

STA	X	Y	X	Y	X	Y	X	Y
1	0.0000	0.0000	0.0000	0.0000	0.0000	0.0000	0.0000	0.0000
2	0.0000	0.0080	0.0000	0.0070	0.0000	0.0095	0.0000	0.0100
3	0.2964	0.1365	0.2976	0.1315	0.2985	0.1330	0.2994	0.1345
4	0.5927	0.2500	0.5952	0.2430	0.5970	0.2430	0.5988	0.2440
5	0.8890	0.3480	0.8928	0.3370	0.8955	0.3338	0.8982	0.3330
6	1.1854	0.4165	1.1904	0.4000	1.1940	0.3970	1.1976	0.3960
7	1.4818	0.4480	1.4880	0.4290	1.4925	0.4245	1.4970	0.4240
8	1.7781	0.4440	1.7856	0.4230	1.7910	0.4190	1.7964	0.4180
9	2.0744	0.4025	2.0832	0.3820	2.0895	0.3770	2.0958	0.3760
10	2.3708	0.3220	2.3808	0.3030	2.3880	0.2980	2.3952	0.2980
11	2.6672	0.1950	2.6784	0.1825	2.6865	0.1764	2.6946	0.1765
12	2.9635	0.0075	2.9760	0.0080	2.9850	0.0080	2.9940	0.0075
13	2.9635	-0.0070	2.9760	-0.0070	2.9850	-0.0076	2.9940	-0.0080
14	2.6672	0.1175	2.6784	0.1040	2.6865	0.0932	2.6946	0.0890
15	2.3708	0.2055	2.3808	0.1835	2.3880	0.1710	2.3952	0.1625
16	2.0744	0.2625	2.0832	0.2380	2.0895	0.2230	2.0958	0.2135
17	1.7781	0.2925	1.7856	0.2675	1.7910	0.2528	1.7964	0.2430
18	1.4818	0.2955	1.4880	0.2725	1.4925	0.2605	1.4970	0.2520
19	1.1854	0.2755	1.1904	0.2570	1.1940	0.2464	1.1976	0.2400
20	0.8890	0.2310	0.8928	0.2180	0.8955	0.2110	0.8982	0.2065
21	0.5927	0.1670	0.5952	0.1590	0.5970	0.1556	0.5988	0.1550
22	0.2964	0.0875	0.2976	0.0825	0.2985	0.0810	0.2994	0.0815
23	0.0000	-0.0090	0.0000	-0.0090	0.0000	-0.0090	0.0000	-0.0090
LER	0.0076		0.0079		0.0085		0.0090	
TER	0.0069		0.0072		0.0076		0.0081	

METRIC UNITS		Sect.	A-A	B-B	C-C	D-D
	Radius meters		0.21624	0.22440	0.23970	0.25500
c	meters		0.075272	0.075590	0.075819	0.076047
γ	radians		0.32597	0.31253	0.28566	0.26489
Ȳ	meters		0.007444	0.006997	0.006840	0.006769
Ȳ	meters		0.039669	0.039921	0.040165	0.040419

STA	X	Y	X	Y	X	Y	X	Y
1	0.000000	0.000000	0.000000	0.000000	0.000000	0.000000	0.000000	0.000000
2	0.000000	0.000203	0.000000	0.000177	0.000000	0.000241	0.000000	0.000254
3	0.007528	0.003467	0.007559	0.003340	0.007581	0.003378	0.007604	0.003416
4	0.015054	0.006350	0.015118	0.006172	0.015163	0.006172	0.015209	0.006197
5	0.022580	0.008839	0.022677	0.008559	0.022745	0.008478	0.022814	0.008458
6	0.030109	0.010579	0.030236	0.010160	0.030327	0.010083	0.030419	0.010058
7	0.037637	0.011379	0.037795	0.010896	0.037909	0.010782	0.038023	0.010769
8	0.045163	0.011277	0.045354	0.010744	0.045491	0.010642	0.045628	0.010617
9	0.052688	0.010223	0.052913	0.009702	0.053073	0.009575	0.053233	0.009550
10	0.060218	0.008178	0.060472	0.007696	0.060655	0.007569	0.060838	0.007569
11	0.067746	0.004953	0.068031	0.004635	0.068237	0.004480	0.068442	0.004483
12	0.075272	0.000190	0.075590	0.000203	0.075819	0.000203	0.076047	0.000190
13	0.075272	-0.000177	0.075590	-0.000177	0.075819	-0.000193	0.076047	-0.000203
14	0.067746	0.002984	0.068031	0.002641	0.068237	0.002367	0.068442	0.002260
15	0.060218	0.005219	0.060472	0.004660	0.060655	0.004343	0.060838	0.004127
16	0.052688	0.006667	0.052913	0.006045	0.053073	0.005664	0.053233	0.005422
17	0.045163	0.007429	0.045354	0.006794	0.045491	0.006421	0.045628	0.006172
18	0.037637	0.007505	0.037795	0.006921	0.037909	0.006616	0.038023	0.006400
19	0.030109	0.006997	0.030236	0.006527	0.030327	0.006258	0.030419	0.006096
20	0.022580	0.005867	0.022677	0.005537	0.022745	0.005359	0.022814	0.005245
21	0.015054	0.004241	0.015118	0.004038	0.015163	0.003952	0.015209	0.003937
22	0.007528	0.002222	0.007559	0.002095	0.007581	0.002057	0.007604	0.002070
23	0.000000	-0.000228	0.000000	-0.000228	0.000000	-0.000228	0.000000	-0.000228
LER	0.000193		0.000200		0.000215		0.000228	
TER	0.000175		0.000182		0.000193		0.000205	

TABLE 16

Stator Coordinates - Sections E, F, G and H

ENGLISH UNITS		Sect.	E-E	F-F	G-G	H-H
Radius	inches		13.25	14.0	14.75	15.1
c	inches		2.9970	2.9995	2.9980	2.9960
γ	degrees		14.27	13.83	13.76	13.67
\bar{Y}	inches		0.2635	0.2694	0.2855	0.3065
\bar{X}	inches		1.5985	1.6083	1.6180	1.6234

STA	X	Y	X	Y	X	Y	X	Y
1	0.0000	0.0000	0.0000	0.0000	0.0000	0.0000	0.0000	0.0000
2	0.0000	0.0095	0.0000	0.0100	0.0000	0.0110	0.0000	0.0107
3	0.2997	0.1130	0.3000	0.1338	0.2998	0.1360	0.2996	0.1390
4	0.5994	0.2420	0.5999	0.2460	0.5996	0.2490	0.5992	0.2585
5	0.8991	0.3310	0.8998	0.3355	0.8994	0.3456	0.8988	0.3600
6	1.1988	0.3965	1.1998	0.4036	1.1992	0.4200	1.1984	0.4415
7	1.4985	0.4270	1.4998	0.4380	1.4990	0.4620	1.4980	0.4902
8	1.7982	0.4210	1.7997	0.4340	1.7988	0.4620	1.7976	0.4945
9	2.0979	0.3795	2.0996	0.3925	2.0986	0.4208	2.0972	0.4525
10	2.3976	0.2995	2.3996	0.3122	2.3984	0.3372	2.3968	0.3650
11	2.6973	0.1790	2.6996	0.1870	2.6982	0.2028	2.6964	0.2215
12	2.9970	0.0080	2.9995	0.0089	2.9980	0.0090	2.9960	0.0115
13	2.9970	-0.0080	2.9995	-0.0090	2.9980	-0.0090	2.9960	-0.0090
14	2.6973	0.0875	2.6996	0.0885	2.6982	0.0970	2.6964	0.1095
15	2.3976	0.1590	2.3996	0.1605	2.3984	0.1768	2.3968	0.1990
16	2.0979	0.2075	2.0996	0.2120	2.0986	0.2300	2.0972	0.2560
17	1.7982	0.2370	1.7997	0.2415	1.7988	0.2600	1.7976	0.2865
18	1.4985	0.2455	1.4998	0.2495	1.4990	0.2665	1.4980	0.2905
19	1.1988	0.2330	1.1998	0.2352	1.1992	0.2478	1.1984	0.2685
20	0.8991	0.2015	0.8998	0.2030	0.8994	0.2090	0.8988	0.2210
21	0.5994	0.1500	0.5999	0.1508	0.5996	0.1510	0.5992	0.1580
22	0.2997	0.0765	0.3000	0.0761	0.2998	0.0765	0.2996	0.0792
23	0.0000	-0.0095	0.0000	-0.0100	0.0000	-0.0105	0.0000	-0.0100
LER	0.0095		0.0100		0.0104		0.0105	
TER	0.0084		0.0089		0.0092		0.0094	

METRIC UNITS		Sect.	E-E	F-F	G-G	H-H
Radius	meters		0.27030	0.28560	0.30090	0.30804
c	meters		0.076123	0.076187	0.076149	0.076098
γ	radius		0.24901	0.24133	0.24011	0.23854
\bar{Y}	meters		0.006692	0.006842	0.007251	0.007785
\bar{X}	meters		0.040601	0.040850	0.041097	0.041234

STA	X	Y	X	Y	X	Y	X	Y
1	0.000000	0.000000	0.000000	0.000000	0.000000	0.000000	0.000000	0.000000
2	0.000000	0.000241	0.000000	0.000254	0.000000	0.000279	0.000000	0.000271
3	0.007612	0.003378	0.007620	0.003398	0.007614	0.003454	0.007609	0.003530
4	0.015224	0.006146	0.015237	0.006248	0.015229	0.006324	0.015219	0.006555
5	0.022837	0.008407	0.022854	0.008521	0.022844	0.008763	0.022829	0.009144
6	0.030449	0.010071	0.030474	0.010251	0.030459	0.010668	0.030439	0.011214
7	0.038061	0.010845	0.038094	0.011125	0.038074	0.011734	0.038049	0.012451
8	0.045674	0.010693	0.045712	0.011023	0.045689	0.011734	0.045659	0.012560
9	0.053288	0.009639	0.053329	0.009969	0.053304	0.010688	0.053268	0.011493
10	0.060899	0.007607	0.060949	0.007929	0.060919	0.008564	0.060878	0.009271
11	0.068511	0.004546	0.068569	0.004749	0.068534	0.005151	0.068488	0.005626
12	0.076123	0.000203	0.076187	0.000226	0.076149	0.000228	0.076098	0.000292
13	0.076123	-0.000203	0.076187	-0.000228	0.076149	-0.000228	0.076098	-0.000228
14	0.068511	0.002222	0.068569	0.002247	0.068534	0.002463	0.068488	0.002781
15	0.060899	0.004038	0.060949	0.004076	0.060919	0.004490	0.060878	0.005054
16	0.053286	0.005270	0.053329	0.005384	0.053304	0.005842	0.053268	0.006502
17	0.045674	0.006019	0.045712	0.006134	0.045689	0.006604	0.045659	0.007277
18	0.038061	0.005235	0.038094	0.005337	0.038074	0.006769	0.038049	0.007378
19	0.030449	0.005918	0.030474	0.005974	0.030459	0.006294	0.030439	0.006819
20	0.022837	0.005118	0.022854	0.005156	0.022844	0.005308	0.022829	0.005613
21	0.015224	0.003810	0.015237	0.003830	0.015229	0.003835	0.015219	0.004013
22	0.07612	0.001943	0.07620	0.001932	0.07614	0.001943	0.07609	0.002011
23	0.000000	-0.000241	0.000000	-0.000254	0.000000	-0.000266	0.000000	-0.000254
LER	0.000241		0.000256		0.000264		0.000266	
TER	0.000213		0.000226		0.000233		0.000238	

TABLE 17

Stator Coordinates - Sections J, K and L

ENGLISH UNITS	Sect	J-J	K-K	L-L
Radius inches		9.9	10.3	15.5
c inches		2.9470	2.9545	2.9960
γ degrees		20.3	19.32	13.55
ȳ inches		0.3295	0.3070	0.3400
ȳ inches		1.5523	1.5578	1.6286

STA	X	Y	X	Y	X	Y
1	0.0000	0.0000	0.0000	0.0000	0.0000	0.0000
2	0.0000	0.0068	0.0000	0.0080	0.0000	0.0102
3	0.2947	0.1415	0.2954	0.1370	0.2996	0.1470
4	0.5894	0.2670	0.5909	0.2565	0.5992	0.2725
5	0.8841	0.3775	0.8864	0.3598	0.8988	0.3838
6	1.1788	0.4540	1.1818	0.4315	1.1984	0.4778
7	1.4735	0.4910	1.4772	0.4650	1.4980	0.5350
8	1.7682	0.4882	1.7727	0.4635	1.7976	0.5422
9	2.0629	0.4460	2.0682	0.4212	2.0972	0.5005
10	2.3576	0.3585	2.3636	0.3370	2.3968	0.4070
11	2.6523	0.2180	2.6590	0.2047	2.6964	0.2500
12	2.9470	0.0082	2.9545	0.0080	2.9960	0.0090
13	2.9470	-0.0078	2.9545	-0.0080	2.9960	-0.0100
14	2.6523	0.1430	2.6590	0.1285	2.6964	0.1332
15	2.3576	0.2460	2.3636	0.2230	2.3968	0.2340
16	2.0629	0.3110	2.0682	0.2842	2.0972	0.2985
17	1.7682	0.3440	1.7727	0.3140	1.7976	0.3290
18	1.4735	0.3460	1.4772	0.3165	1.4980	0.3290
19	1.1788	0.3190	1.1818	0.2925	1.1984	0.2972
20	0.8841	0.2635	0.8864	0.2425	0.8988	0.2400
21	0.5894	0.1550	0.5909	0.1735	0.5992	0.1700
22	0.2947	0.0935	0.2954	0.0890	0.2996	0.0840
23	0.0000	-0.0090	0.0000	-0.0080	0.0000	-0.0095
LER	0.0070		0.0073		0.0107	
TER	0.0065		0.0067		0.0096	

METRIC UNITS	Sect.	J-J	K-K	L-L
Radius meters		0.20196	0.21012	0.31620
c meters		0.074853	0.075044	0.076098
γ radius		0.35424	0.33713	0.23645
ȳ meters		0.008369	0.007797	0.008636
ȳ meters		0.039428	0.039568	0.041366

STA	X	Y	X	Y	X	Y
1	0.000000	0.000000	0.000000	0.000000	0.000000	0.000000
2	0.000000	0.000172	0.000000	0.000203	0.000000	0.000259
3	0.007485	0.003594	0.007503	0.003479	0.007609	0.003733
4	0.014970	0.006781	0.015008	0.006515	0.015219	0.006921
5	0.022456	0.009588	0.022514	0.009138	0.022829	0.009748
6	0.029941	0.011531	0.030017	0.010960	0.030439	0.012136
7	0.037426	0.012471	0.037520	0.011811	0.038049	0.013589
8	0.044912	0.012400	0.045026	0.011772	0.045659	0.013771
9	0.052397	0.011328	0.052532	0.010698	0.053268	0.012712
10	0.059883	0.009105	0.060035	0.008559	0.060878	0.010337
11	0.067368	0.005537	0.067538	0.005199	0.068488	0.006350
12	0.074853	0.000208	0.075044	0.000203	0.076098	0.000225
13	0.074853	-0.000198	0.075044	-0.000203	0.076098	-0.000254
14	0.067368	0.003632	0.067538	0.003263	0.068488	0.003383
15	0.059883	0.006248	0.060035	0.005664	0.060878	0.005943
16	0.052397	0.007899	0.052532	0.007218	0.053268	0.007581
17	0.044912	0.008737	0.045026	0.007975	0.045659	0.008356
18	0.037426	0.008798	0.037520	0.008039	0.038049	0.038356
19	0.029941	0.008102	0.030017	0.007429	0.030439	0.007548
20	0.022456	0.006692	0.022514	0.006159	0.022829	0.006096
21	0.014970	0.004699	0.015008	0.004406	0.015219	0.004318
22	0.007485	0.002374	0.007503	0.002260	0.007609	0.002133
23	0.000000	-0.000228	0.000000	-0.000203	0.000000	-0.000241
LER	0.000177		0.000185		0.000271	
TER	0.000165		0.000170		0.000243	

APPENDIX 11

Nomenclature

APPENDIX 11

Nomenclature

- A = speed of sound
- a = distance to maximum camber point from leading edge
- a/a* = critical area ratio
- b = rotor semi-chord at 75 percent of span from root, inches or meters
- B = location of first captured Mach wave on suction surface
- B' = point midway between leading edge and first captured Mach wave emanation point on suction surface
- c = chord, inches or meters
- D = diffusion factor = $1 - \frac{V_{i+1}}{V_i} + \frac{r_{i+1} (V_{\theta_{i+1}}) - r_i (V_{\theta_i})}{(r + r_{i+1}) V_i \sigma}$
- i = 1 for rotors and 2 for stators; V_i and V_{i+1} become V'_i and V'_{i+1} respectively for rotors
- E = excitation per rotor revolution
- h = streamtube height
- H = total or stagnation entropy, Btu/lb mass (cal/kg)
- i = incidence = angle between inlet air direction and tangent to blade mean camber line at leading edge, degrees or radians
- k = ratio of specific heats
- K = blockage factor
- M = Mach number
- m_c = correlation factor in Carter's rule = $0.92(a/c)^2 + 0.002\beta_2$
- m = distance along a meridional streamline (in Z - R plane)

- P = total or stagnation pressure, lb/ft^2 or kg/m^2
 p = static or stream pressure, lb/ft^2 or kg/m^2
 r = radius
 R, θ, Z = cylindrical coordinate system located with Z axis as rig centerline and with unit vectors \bar{i}, \bar{j} , and \bar{k} respectively
 R_c = streamline radius of curvature
 \bar{R} = total recovery across rotor after profile and shock losses
 s = blade spacing, inches or meters
 T = temperature, $^{\circ}\text{R}$ or $^{\circ}\text{K}$
 t = blade maximum thickness, inches or meters
 U = rotor speed, ft/sec or meter/sec
 V = air velocity, ft/sec or meter/sec
 \bar{V} = absolute air velocity vector =
 $V_R \bar{i} + V_{\theta} \bar{j} + V_Z \bar{k}$, ft/sec or meter/sec
 \bar{V}' = relative air velocity vector =
 $V_R \bar{i} + V_{\theta} \bar{j} + V_Z \bar{k}$, ft/sec or meter/sec
 V_m = meridional air velocity =
 $(V_R^2 + V_Z^2)^{1/2}$, ft/sec or meter/sec
 X = airfoil coordinate parallel to chord
 \bar{X} = horizontal distance to airfoil center of gravity from leading edge along chord, inches or meters
 Y = airfoil coordinate normal to chord
 \bar{Y} = vertical distance to airfoil center of gravity from chord, inches or meters
 y = length along calculation station from centerline to point of interest

- W = weight flow
- α = critical surface angle approximating a streamline of revolution as measured from the axial direction, degrees or radians
- β_z = absolute air angle = $\cot^{-1} (V_z/V_\theta)$, degrees or radians (plane parallel to z axis)
- β_m = absolute air angle = $\cot^{-1} (V_m/V_\theta)$, degrees or radians (meridional plane)
- β'_z = relative air angle = $\cot^{-1} (V_z/V'_\theta)$, degrees or radians (plane parallel to z axis)
- β'_m = relative air angle = $\cot^{-1} (V_m/V'_\theta)$, degrees or radians (meridional plane)
- β^* = stator metal angle on conical surface, angle between tangent to mean camber line and meridional directional at leading and trailing edge, degrees or radians
- β'^* = rotor metal angle on conical surface, angle between tangent to mean camber line and axial direction at leading or trailing edge, degrees or radians
- $\Delta\beta$ = air-turning angle, difference between inlet and exit flow angles across a blade row, degrees
- γ = blade chord angle, angle between chord and axial direction on cylindrical surface degrees or radians
- ϵ = angle between tangent to streamline projected on meridional plane and axial direction, degrees or radians
- λ = angle of calculation station measured from axial direction
- μ = Prandtl-Meyer function
- ν = oblique shock angle
- ρ = density, lb mass/ft³ or kg/m³
- σ = solidity, ratio of chord to spacing
- ϕ = blade camber angle, difference between blade angles at leading and trailing edges on conical surface, $\beta'_1 - \beta'_2$ for rotors and $\beta_2 - \beta_3$ for stators, degrees or radians

- ψ = denotes a streamline
 ω = angular velocity of rotor, radians/sec
 ω_t = torsional frequency, radians/sec
 $\bar{\omega}$ = total pressure loss coefficient, mass average defect in relative total pressure divided by difference between inlet stagnation and static pressure
 Ω = rotor slot angle with suction surface
 L.E.R. = leading edge radius, inches or meters
 T.E.R. = trailing edge radius, inches or meters

Subscripts

- av = average
 f = front
 m = meridional
 n = normal component
 p = profile
 r = coordinate normal to axis with unit vector \bar{i}
 s = shock
 sl = slot region
 ss = suction surface
 ss_{ss} = suction surface supersonic
 t^{ss} = total
 x = upstream of normal-oblique shock combination
 x_a = upstream oblique shock
 x_b = upstream normal shock with oblique shock present
 y = downstream oblique shock
 z = coordinate along axis with unit vector \bar{k}
 θ = coordinate in tangential direction with unit vector \bar{j}
 1 = station into rotor
 2 = station out of rotor or into stator
 3 = station out of stator
 4 = downstream normal shock in slot region
 5 = downstream normal shock in oblique shock region
 6 = downstream normal shock in clean upstream region

Superscript

- ' = relative to rotor

REFERENCES

1. Seyler, D. R. and J. P. Gostelow, Single-Stage Experimental Evaluation of High-Mach-Number Compressor-Rotor Blading, Part 2 - Performance of Rotor 1B, NASA CR-54582, GER67FPD236, 1967
2. Gostelow, J. P. and K. W. Krabacher, Single-Stage Experimental Evaluation of High-Mach-Number Compressor-Rotor Blading, Part 3 - Performance of Rotor 2E, NASA CR-54583, GER67FPD248, 1967
3. Gostelow, J. P. and K. W. Krabacher, Single-Stage Experimental Evaluation of High-Mach-Number Compressor-Rotor Blading, Part 5 - Performance of Rotor 2B, NASA CR-54585, GER67FPD278, 1967
4. Gostelow, J. P. and K. W. Krabacher, Single-Stage Experimental Evaluation of High-Mach-Number Compressor-Rotor Blading, Part 4 - Performance of Rotor 2D, NASA CR-54584, GER67FPD276, 1967
5. Keenan, M. J., K. G. Harley and G. A. Bogardus, Experimental Evaluation of Transonic Stators, Data and Performance Report, Multiple-Circular-Arc Stator A, NASA CR-54621, PWA-3260, 1968
6. Peacock, R. E., Flow Control in the Corners of Cascades, A. R. C. 27 291, October 1965
7. Ferri, Kuchemann and Sterne, Progress in Aeronautical Sciences, Vol. II, pp 43-47 and 114-119, Pergamon Press, 1962
8. Miller, G. R., G. W. Lewis Jr. and M. J. Hartmann, Shock Losses in Transonic Compressor Blade Rows, ASME Paper 60-WA-77
9. Bogdonoff, S. M. and C. E. Kepler, Separation of a Supersonic Turbulent Boundary Layer, Jour. Aero. Sci., pp 414-424, 1955